University of Alberta

Planar Imaging Quantification: A New Method using 3D Attenuation Correction Data and Monte Carlo Simulated Buildup Factors

by

COLLIE ROY E. MILLER ©

A thesis submitted to the Faculty of Graduate Studies and Research in partial
fulfilment of the requirements for the degree of Doctor of Philosophy

in

RADIOLOGY AND DIAGNOSTIC IMAGING - MEDICAL SCIENCES

EDMONTON, ALBERTA

FALL 1996

National Library
of Canada

Acquisitions and
Bibliographic Services Branch

395 Wellington Street
Ottawa, Ontario
K1A 0N4

Bibliothèque nationale
du Canada

Direction des acquisitions et
des services bibliographiques

395, rue Wellington
Ottawa (Ontario)
K1A 0N4

Your file Votre référence

Our file Notre référence

The author has granted an irrevocable non-exclusive licence allowing the National Library of Canada to reproduce, loan, distribute or sell copies of his/her thesis by any means and in any form or format, making this thesis available to interested persons.

L'auteur a accordé une licence irrévocable et non exclusive permettant à la Bibliothèque nationale du Canada de reproduire, prêter, distribuer ou vendre des copies de sa thèse de quelque manière et sous quelque forme que ce soit pour mettre des exemplaires de cette thèse à la disposition des personnes intéressées.

The author retains ownership of the copyright in his/her thesis. Neither the thesis nor substantial extracts from it may be printed or otherwise reproduced without his/her permission.

L'auteur conserve la propriété du droit d'auteur qui protège sa thèse. Ni la thèse ni des extraits substantiels de celle-ci ne doivent être imprimés ou autrement reproduits sans son autorisation.

ISBN 0-612-18082-4

Canada

University of Alberta

Library Release Form

NAME OF AUTHOR: Collie Roy E. Miller

TITLE OF THESIS: Planar Imaging Quantification: A New Method using 3D Attenuation Correction Data and Monte Carlo Simulated Buildup Factors.

DEGREE: Doctor of Philosophy

YEAR THIS DEGREE GRANTED: 1996

Permission is hereby granted to the University of Alberta Library to reproduce single copies of this thesis and to lend or sell such copies for private, scholarly or scientific research purposes only.

The author reserves all other publication and other rights in association with the copyright in the thesis, and except as hereinbefore provided neither the thesis or any substantial portion thereof may be printed or otherwise reproduced in any material form whatever without the author's prior written permission.

Collie R.E. Miller
Suite 604, Newton Place
8515 - 112 Street
Edmonton, Alberta
T6G 1K7
Canada

Dated: October 4, , 1996

University of Alberta
Faculty of Graduate Studies and Research

The undersigned certify that they have read, and recommended to the Faculty of Graduate Studies and Research for acceptance, a thesis entitled **Planar Imaging Quantification: A New Method using 3D Attenuation Correction Data and Monte Carlo Simulated Buildup Factors** submitted by Collie Roy E. Miller in partial fulfillment of the requirements for the degree of Doctor of Philosophy in Radiology and Diagnostic Imaging.

Dr. L.J. Filipow (Supervisor)

Dr. S.A. Jackson (Co-supervisor)

Dr. A.J.B. McEwan

Dr. M.E. Hoskinson

Z J Koles

Dr. Z.J. Koles

Dr. D.P. Hube

Dr. L.J. Hahn (External Examiner)

Dated: October 4, 1996

Abstract

A new method to correct for attenuation and the buildup of scatter in planar imaging quantification is presented. The method is based on the combined use of 3D density information provided by computed tomography to correct for attenuation and the application of Monte Carlo simulated buildup factors to correct for buildup in the projection pixels. CT and nuclear medicine images were obtained for a purpose built nonhomogeneous phantom that models the human anatomy in the thoracic and abdominal regions. The CT transverse slices of the phantom were converted to a set of consecutive density maps. An algorithm was developed that projects the 3D information contained in the set of density maps to create opposing pairs of accurate 2D correction maps that were subsequently applied to planar images acquired from a dual head gamma camera. A comparison of results obtained by the new method and the geometric mean approach based on published techniques is presented for some of the source arrangements used. Excellent results were obtained for various source-phantom configurations used to evaluate the method. Activity quantification of a line source at most locations in the nonhomogeneous phantom produced errors of less than 2%. Additionally, knowledge of the actual source depth is not required for accurate activity quantification. Quantification of volume sources placed in foam, perspex and aluminum produced errors of less than 7% for the abdominal and thoracic configurations of the phantom. A clinical evaluation of the method was also performed. CT slices of a standard man provided the required data for attenuation correction in nuclear medicine patients. Quantification of ^{99m}Tc lung activity for 6 patients using the new method produced errors of less than 5%.

Acknowledgments

I would like to thank my supervisor, Dr. Larry Filipow for his support and guidance during the course of this research. I thank him for the unlimited time , interest and effort that he has contributed to my academic program and general progress. It has been most enjoyable doing research with him. I would like to thank Dr. Stuart Jackson for his help and contribution to this research. I appreciate his interest and support. I am grateful to both Drs. Filipow and Jackson for their friendship, kind thoughts and the many enjoyable discussions that we had. My sincere thanks to Dr. Michael Hoskinson for his assistance in organizing the clinical studies in nuclear medicine. I would like to thank Dr. Terence Riauka for his help and friendship. I would also like to thank the following people who contributed in various ways to my research: Drs. Sandy McEwan, Connor Maguire, Z.J. Koles, Lawrence Le, J. Kivilu, Mrs. Loralee Robertson, Mr. R. Hughes, Mr. E. Mah, Mrs J. Dawson and Mrs. H. Skolarchuk. I would like to thank members of staff in nuclear medicine, CT and x-ray.

Finally, I would like to express my sincere thanks and appreciation to my family and the Gordon family for their love and support and to thank Dr. W.F.B. Clarke for his friendship, encouragement and invaluable support during the years of my studies.

Table of Contents

1.0 Introduction 1

1.1 Overview of Nuclear Medicine Imaging 1

1.2 Overview of Activity Quantification in Nuclear Medicine 4

1.3 Outline of Thesis 7

2.0 Background Physics to Nuclear Medicine Imaging 11

2.1 Photon Propagation Through Matter 11

Compton Scattering 12
Photoelectric Absorption 13
Rayleigh Scattering 15
Attenuation under of Narrow and Broad Beam Conditions 16
Effects of the Interaction Processes 17

2.2 Activity, Calibration and Radionuclides 22

Activity and Calibration 22
Radionuclides 23

2.3 Gamma Camera Imaging 25

Basic Principles of Operation 26
Collimators 28
Detector Crystal 33
Photomultiplier Tube Array and Computing Circuits 34
Intrinsic Efficiency, Energy and Resolution 36
Effect of Count Rate on Detector Performance 37
Random Errors in Image Counts 38

3.0 Correction Methods for Accurate Activity Quantification 39

3.1 Window Methods 39

- Dual Energy Window 39
- Dual Photopeak Window 41
- Asymmetric Window 44

3.2 Attenuation Coefficients and Correction Maps 46

- Geometric Mean Method 47
- Transmission-Emission Method 49
- Chang Algorithm 52

3.3 Buildup factors 53

4.0 Theoretical Considerations of New Method and General Concepts of Monte Carlo Simulations 55

4.1 Theory 55

4.2 Monte Carlo Technique 61

- Brief Description of the Monte Carlo Code 62
- Theoretical Models 65

5.0 Experimental Validation using Physical Phantoms 66

5.1 Materials and Methods 66

- Design and Construction of the Phantom 66
- Thoracic and Abdominal Phantom Configurations 66
- Computed Tomography 68
- Nuclear Medicine Imaging 69
- Determination of 2D Correction Maps 76
- Summary of Correction Algorithm 78
- Simulation of Buildup Functions 78
- Summary of Procedures for New Method 79

5.2 Results and Discussion 81

- Sensitivity 81
- Buildup Function Simulations 82
- Comparison of Methods 84
- Evaluation of Methods using Projection Profiles 85
- Effects of Incorrect Source Depth Estimation 88
- Spectral Analysis 89
- Quantification of Volume Sources 90
- Error Analysis 91

6.0 Clinical Applications 120

6.1 Materials and Methods 120

- Anatomical Data 120
- Development of the Computerized Human Model 121
- Patient Studies 122
- Implementation of the Model 128
- Alignment and Combination of Images 130
- Monte Carlo Simulation of Clinically Realistic Buildup 135

6.2 Results and Discussion 136

7.0 Conclusions and Future Work 148

7.1 Conclusions 148

7.2 Future Work 151

List of Figures

Figure 1: Example of dual head gamma camera used to acquire nuclear medicine images. 10

Figure 2: (a) Illustration of Compton scattering and (b) differential Klein-Nishina solid angle for scattering. 14

Figure 3: Narrow beam (a) and broad beam (b) geometries. 19

Figure 4: (a) Cross section of phantom with sources 1 and 2. Only one source present at any given time. 1 = 16 cm depth and 2 = 4 cm depth. (b) Images 1 and 2 correspond to source locations 1 and 2 respectively. 20

Figure 5: Basic components of the gamma camera. 27

Figure 6: Illustration of collimator geometry and acceptance angle. 30

Figure 7: Illustration of changes in collimator resolution with source to collimator distance. 31

Figure 8: Dual energy windows with lower energy scatter window,C,and photopeak window, P. 42

Figure 9: Dual photopeak windows with lower half, L, and upper half, U. 42

Figure 10: Asymmetric energy windows with lower photopeak window, L, shifted towards the upper photopeak window, U. 45

Figure 11: Asymmetric energy windows with upper photopeak window, U, extended to the lower photopeak window, L. 45

Figure 12: Geometry of nonhomogeneous phantom and gamma camera. 50

Figure 13: Geometry of setup for transmission measurement using a flood source. 50

Figure 14: Transverse section of body containing a point source. $M_a(i, j)$ and $M_p(i, j)$ are the anterior and posterior uncorrected images respectively and r is an index for a ray at projection angle, θ. 57

Figure 15: Volume of height, t, and coronal plane, CP, at depth, d. ACM and PCM are the anterior and posterior 2D correction maps respectively. 58

Figure 16: Design of phantom shown in (a). The arrows point to one of the small rectangular perspex blocks (b) of which the phantom iscomprised. (c) is the cross section of the thoracic configuration consisting of 4 cm x 4 cm aluminium (spine) and two 14 cm x 7 cm foam inserts (lungs). (d) is the cross section of the abdominal configuration consisting of a 4 cm x 4 cm aluminium insert. 67

Figure 17: (a) Transverse section of homogeneous perspex phantom with line source configuration (A). (b) Transverse section of nonhomogeneous phantom, which consists of perspex and a 4 cm x 4 cm aluminium block, with line source configurations (B) and (C). Each configuration was used under two conditions: (i) Only a single source present at any given time and (ii) Two sources present at any given time and were vertically separated. The gamma camera positions are shown above and below the phantom. 72

Figure 18: Transverse section of nonhomogeneous phantom with line source configuration (1 -16). The phantom consists of perspex, 4 cm x 4 cm aluminium, 3 cm x 3 cm water and 3 cm x 3 cm foam. Only one source was present at any given time. The gamma camera positions are shown at the top of each phantom arrangement. 73

Figure 19: Transverse section of nonhomogeneous phantom horizontally separated sources. Two sources were present at any given time. Source 1 was kept in position while the second source moves to positions 2, 3, 4 and 5, each 2 cm apart. 74

Figure 20: Transverse section of nonhomogeneous phantom with source positions (9 - 12). This configuration shows the actual depth of the source (solid line) and assumed depths (dashed line). Assumed depths varied by 1 cm step from 2 cm to 18 cm and only one source present at any given time. The gamma camera positions are shown above and below the phantom. 74

Figure 21: Illustration of the new method. NM = nuclear medicine, CT = computed tomography, Ant I = anterior nuclear medicine image, Post I = posterior nuclear medicine image, Cor Ant I = corrected anterior nuclear medicine image, Cor Post I = corrected posterior nuclear medicine image, Ant Cor Map = anterior correction map, Post Cor Map = posterior correction map. 80

Figure 22: Results of sensitivity experiments 83

Figure 23: Monte Carlo simulated buildup function for ^{99m}Tc line source in persperx phantom using a 20% energy window. 83

Figure 24: Results for the source configuration used in Figure 17 when only one source was present in the homogeneous phantom (A) and nonhomogeneous phantom for overlap region (B) and nonoverlap region (C). (a) Results obtained by the new method. 95

Figure 25: Results for the source configuration used in Figure 17 when two sources were present in the homogeneous phantom (A) and nonhomogeneous phantom for overlap region (B) and nonoverlap region (C). (a) Results obtained by the new method. 96

Figure 26(a): Projection profile for source-detector configuration of Figure 18(a) with source at position 1 (shown in lower left of graph). 97

Figure 26(b): Projection profile for source-detector configuration of Figure 18(a) with source at position 2 (shown in lower left of graph). 97

Figure 26(c): Projection profile for source-detector configuration of Figure 18(a) with source at position 3 (shown in lower left of graph). 98

Figure 26(d): Projection profile for source-detector configuration of Figure 18(a) with source at position 4 (shown in lower left of graph). 98

Figure 26(e): Projection profile for source-detector configuration of Figure 18(a) with source at position 5 (shown in lower left of graph). 99

Figure 26(f): Projection profile for source-detector configuration of Figure 18(a) with source at position 6 (shown in lower left of graph). 99

Figure 26(g): Projection profile for source-detector configuration of Figure 18(a) with source at position 7 (shown in lower left of graph). 100

Figure 26(h): Projection profile for source-detector configuration of Figure 18(a) with source at position 8 (shown in lower left of graph). 100

Figure 27(a) Projection profile for source-detector configuration of Figure 18(b) with source at position 9 (shown in lower left of graph). 101

Figure 27(b): Projection profile for source-detector configuration of Figure 18(b) with source at position 10 (shown in lower left of graph). 101

Figure 27(c): Projection profile for source-detector configuration of Figure 18(b) with source at position 11 (shown in lower left of graph). 102

Figure 27(d): Projection profile for source-detector configuration of Figure 18(b) with source at position 12 (shown in lower left of graph). 102

Figure 27(e): Projection profile for source-detector configuration of Figure 18(b) with source at position 13 (shown in lower left of graph). 103

Figure 27(f): Projection profile for source-detector configuration of Figure 18(b) with source at position 14 (shown in lower left of graph). 103

Figure 27(g): Projection profile for source-detector configuration of Figure 18(b) with source at position 15 (shown in lower left of graph). 104

Figure 27(h): Projection profile for source-detector configuration of Figure 18(b) with source at position 16 (shown in lower left of graph). 104

Figure 28(a): Projection profile for source-detector configuration of Figure 18(a) with volume source at position 1 (shown in lower left of graph). 105

Figure 28(b): Projection profile for source-detector configuration of Figure 18(a) with volume source at position 2 (shown in lower left of graph). 105

Figure 28(c): Projection profile for source-detector configuration of Figure 18(a) with volume source at position 3 (shown in lower left of graph). 106

Figure 28(d): Projection profile for source-detector configuration of Figure 18(a) with volume source at position 4 (shown in lower left of graph). 106

Figure 28(e): Projection profile for source-detector configuration of Figure 18(a) with volume source at position 5 (shown in lower left of graph). 107

Figure 28(f): Projection profile for source-detector configuration of Figure 18(a) with volume source at position 6 (shown in lower left of graph). 107

Figure 28(g): Projection profile for source-detector configuration of Figure 18(a) with volume source at position 7 (shown in lower left of graph). 108

Figure 28(h): Projection profile for source-detector configuration of Figure 18(a) with volume source at position 8 (shown in lower left of graph). 108

Figure 29(a): Projection profile for source-detector configuration of Figure 18(b) with volume source at position 9 (shown in lower left of graph). 109

Figure 29(b): Projection profile for source-detector configuration of Figure 18(b) with volume source at position 10 (shown in lower left of graph). 109

Figure 29(c): Projection profile for source-detector configuration of Figure 18(b) with volume source at position 11 (shown in lower left of graph). 110

Figure 29(d): Projection profile for source-detector configuration of Figure 18(b) with volume source at position 12 (shown in lower left of graph). 110

Figure 29(e): Projection profile for source-detector configuration of Figure 18(b) with volume source at position 13 (shown in lower left of graph). 111

Figure 29(f): Projection profile for source-detector configuration of Figure 18(b) with volume source at position 14 (shown in lower left of graph). 111

Figure 29(g): Projection profile for source-detector configuration of Figure 18(b) with volume source at position 15 (shown in lower left of graph). 112

Figure 29(h): Projection profile for source-detector configuration of Figure 18(b) with volume source at position 16 (shown in lower left of graph). 112

Figure 30(a): Projection profile for source-detector configuration of Figure 19(a) with two line sources horizontally separated by 2 cm (shown in lower left of graph). 113

Figure 30(b): Projection profile for source-detector configuration of Figure 19(a) with two line sources horizontally separated by 4 cm (shown in lower left of graph). 113

Figure 30(c): Projection profile for source-detector configuration of Figure 19(a) with two line sources horizontally separated by 6 cm (shown in lower left of graph). 114

Figure 30(d): Projection profile for source-detector configuration of Figure 19(a) with two line sources horizontally separated by 8 cm (shown in lower left of graph). 114

Figure 31(a): Projection profile for source-detector configuration of Figure 19(b) with two line sources horizontally separated by 2 cm (shown in lower left of graph). 115

Figure 31(b): Projection profile for source-detector configuration of Figure 19(b) with two line sources horizontally separated by 4 cm (shown in lower left of graph). 115

Figure 31(c): Projection profile for source-detector configuration of Figure 19(b) with two line sources horizontally separated by 6 cm (shown in lower left of graph). 116

Figure 31(d): Projection profile for source-detector configuration of Figure 19(b) with two line sources horizontally separated by 8 cm (shown in lower left of graph). 116

Figure 32: Variation in estimated activity with assumed source depth using the configuration shown in Figure 20. 117

Figure 33: The geometric mean of counts for four different energy regions of the spectrum from a ^{99m}Tc line source at various depths in a perspex phantom. 117

Figure 34: Variation in the proportion of counts with source depth for various energy regions of the spectra from a point source. 118

Figure 35: Variation in the proportion of counts with source depth for various energy regions of the spectra from two point sources separated horizontally by 2 cm. 118

Figure 36: Variation in the proportion of counts with source depth for various energy regions of the spectra from two point sources separated horizontally by 6 cm. 119

Figure 37: Variation in the proportion of counts with source depth for various energy regions of the spectra from two point sources separated horizontally by 10 cm. 119

Figure 38: CT transverse slices of the standard man from neck to midthigh. 123

Figure 39: Density maps of the standard man from neck to midthigh. 124

Figure 40: (a) CT slices of a section of the thorax and (b) the corresponding density maps. 125

Figure 41: (a) CT slices of a section of the abdomen and (b) the corresponding density maps. 126

Figure 42: (a) Posterior (1) and anterior (2) correction maps of the collapsed thorax. 132

Figure 43: (a) Non-aligned ventilation and perfusion images. (b) The horizontally aligned images. 133

Figure 44: Examples of 2D correction maps (posterior) with different lung sizes. Images (a) to (d) were generated from collapsed CT slices of the same human being. 134

Figure 45: Patient #1: 1) ventilation, 2) perfusion, 3) "pure" perfusion, 4) 2D correction map and 5) the corrected image. All are posterior views. 142

Figure 46: Patient #2: 1) ventilation, 2) perfusion, 3) "pure" perfusion, 4) 2D correction map and 5) the corrected image. All are posterior views. 143

Figure 47: Patient #3: 1) ventilation, 2) perfusion, 3) "pure" perfusion, 4) 2D correction map and 5) the corrected image. All are posterior views. 144

Figure 48: Patient #4: 1) ventilation, 2) perfusion, 3) "pure" perfusion, 4) 2D correction map and 5) the corrected image. All are posterior views. 145

Figure 49: Patient #5: 1) ventilation, 2) perfusion, 3) "pure" perfusion, 4) 2D correction map and 5) the corrected image. All are posterior views. 146

Figure 50: Patient #6: 1) ventilation, 2) perfusion, 3) "pure" perfusion, 4) 2D correction map and 5) the corrected image. All are posterior views. 147

List of Tables

Table 1: Density and linear attenuation coefficient values for phantom inserts. 93

Table 2: Results of sensitivity experiments. 93

Table 3: Monte Carlo simulated buildup factors at various depths and energy window settings. 93

Table 4: Percentage of actual activity estimated in various source-phantom configurations. The values in the table represent the averages for the three situations indicated. 94

Table 5: Percentage actual counts obtained from conjugate projections. The values in the table represent the averages for the three categories indicated. 94

Table 6: Results of volume sources in abdominal and thoracic phantom. 94

Table 7: Tissue types used in model and the assigned densities. 140

Table 8: Patient information including weight and chest thickness. 140

Table 9: ROI counts for the ventilation (Vent), Perfusion (Perf) and "Pure" Perfusion (P. Perf) images. 141

Table 10: Injected and calculated activities using both methods and the errors associated with them. 141

Chapter 1

Introduction

1.1 Overview of Nuclear Medicine Imaging

The use of ionizing radiation for medical purposes is the result of a plethora of scientific discoveries and technological developments during the past century. This began with the discovery of x-rays by Wilhelm Roentgen in 1895 (1), of radioactivity by Henri Bequerel in 1896 (2) and of radium by Pierre and Marie Curie in 1898 (3). Detailed accounts of the interesting discoveries and developments that took place between then and now are well documented in a number of publications (4, 5, 6), and will not be presented here. However, it is important to note that the aforementioned discoveries of the late 1890s, herald the beginning of a new era in science that evolved into the study of nuclear physics and the "birth" of nuclear medicine, radiotherapy and diagnostic radiology.

Perhaps the simplest definition of nuclear medicine is that it is a specialized field of medicine that involves the administration of a radioactive substance known as a radiopharmaceutical to a patient for diagnostic or therapeutic purposes. The radiopharmaceutical is a complex chemical substance that is labeled or tagged with a radioactive element (radionuclide) and has specific physical, chemical and biological properties that enable selective organ or tissue localization in the body.

The primary objective of nuclear medicine imaging is to obtain information about organ function in a patient. This is the major distinction between this imaging modality and the other familiar imaging modalities such as conventional x-ray, computed tomography (CT) and magnetic resonance imaging (MRI), where the primary objective is to provide structural (anatomical) information. Nuclear medicine imaging procedures generally begin with the patient being given an intravenous injection of an appropriate radiopharmaceutical for the organ of interest (called the target organ). It is desirable from both an imaging and radiation safety point of view that maximum accumulation (uptake) of the radiopharmaceutical takes place in the target organ and there should be only an insignificant accumulation in any other organ or tissue. The uptake rate, distribution and clearance rate of the radiopharmaceutical in the target organ is related to the functional state of the organ and is used to indicate the presence of a disease or disorder. The radiopharmaceutical distribution in the body is detected externally using a special radiation detector called an Anger or scintillation camera which produces a 2D image of the distribution. This is possible due to the emission of gamma photons of suitable energy from the radioactive element used to label the pharmaceutical.

Current technology has the camera or cameras mounted on a rotating gantry that allows for 360° rotation about the patient. Images can then be acquired by either static planar 2D imaging or rotating, single photon emission computed tomography (SPECT) methods. Figure 1 shows a dual head SPECT camera that can be used for either acquisition. In planar imaging, projection images are acquired at a fixed angle with respect to the patient to produce a 2D representation of the activity distribution. In SPECT imaging, projection images are acquired at many evenly spaced angles around the patient and then digitally reconstructed to produce a 3D representation of the radiopharmaceutical distribution. The pattern of the radiopharmaceutical distribution varies with different studies. In some studies the normal organ accumulates the radiopharmaceutical and the lesion or diseased area does not ("cold" area). Examples of this are liver scans with technetium-99m (^{99m}Tc) sulfur colloids and lung scans with ^{99m}Tc macroaggregated particles (^{99m}Tc MAA). In other studies the diseased or affected area will selectively concentrate the radiopharmaceutical relative to its surroundings ("hot" area). Examples of this are the presence of lesions in bone scans with ^{99m}Tc pyrophosphate and tumour sites in gallium-67 (^{67}Ga) citrate scans.

The mechanism of radiopharmaceutical localization in the body varies for each organ study. Some common examples include: 1) **localization by capillary blockade** of the radiopharmaceutical, ^{99m}Tc MAA (particle size 10 - 90 µm) in lungs. Almost immediately after injection it becomes trapped in the pulmonary capillary bed. Imaging its distribution provides a representative assessment of lung perfusion, 2) **localization**

by phagocytosis of ^{99m}Tc sulfur colloid particles (100 nm) by cells of the reticuloendothelial system in the liver and spleen. These cells recognize the small foreign substances in the blood and remove them by phagocytosis. This allows for imaging of the liver and spleen, 3) **compartmental localization** whereby the radiopharmaceutical is introduced directly into a well defined anatomical compartment. One example is the inhalation of Xenon-133 (^{133}Xe) gas into the lungs for a ventilation scan to visualize the tracheo-bronchial airways and 4) **active transport** whereby the radiopharmaceutical is concentrated in tissue against a concentration gradient above plasma levels. A classic example is the trapping and organification of radioactive iodide by the thyroid gland. Further discussions on these and other mechanisms of radiopharmaceutical localization in the body can be found elsewhere (7, 8).

1.2 Overview of Activity Quantification in Nuclear Medicine

The increasing use of sophisticated gamma camera systems and a number of new radiopharmaceuticals in nuclear medicine has generated much interest in activity quantification. Absolute quantification of the *in vivo* distribution of radioactivity is important in clinical research and for understanding many physiological processes. It provides significant diagnostic and therapeutic information on patient dosimetry and has potential applications that may influence patient management. For example, quantification may be used to assess blood flow to tumours or to investigate the extent of certain diseases by calculating the uptake of radiopharmaceuticals which concentrate at sites of inflammation. Other examples include the accurate calculation of dose to organs at risk from quantification data and evaluation of the fate of sequestered radiolabeled platelets.

Despite recent advances, absolute quantification of the 3D distribution of a radionuclide within a patient remains one of the greatest challenges of nuclear medicine. This is due to the fact that nuclear medicine images are degraded by several factors which limit the quantitative ability of this modality. The two most influential factors on the accuracy of activity quantification are Compton scatter and photoelectric absorption. These two processes are due to the interaction of emitted photons with tissue and occur in the patient before the photons are detected externally.

Several methods have been proposed to improve the accuracy of activity quantification in planar and SPECT imaging. In principle, correction methods used in planar imaging can be applied to SPECT imaging. The methods used by most investigators can be placed into three broad categories. The first involves the use of energy window techniques for planar (9-14) and SPECT (15-19) imaging. The second utilizes a broad beam effective linear attenuation coefficient for correction in planar imaging (20-22) and may include a term to correct for source thickness (23). For this category, SPECT imaging has also utilized a single empirically derived, effective attenuation coefficient (24-26) and recently, the use of attenuation correction maps with varied linear attenuation coefficients for nonhomogeneous structures (27-29). Meikle *et al* (30) have demonstrated improved accuracy in SPECT imaging quantification for nonhomogeneous structures using a transmission-dependent scatter correction technique.

The third method uses a buildup function for scatter correction in planar (31-33) and SPECT (34) acquisitions. The accuracy of any of the methods depends on its ability to correct for scatter. At present, none of the scatter correction methods has been adopted as the standard method for clinical use. The principles involved and the limitations of these methods are discussed in several publications such as (35, 36). It is important to note that any method that is proposed for clinical use to improve the accuracy of activity quantification should take into account the density variation in a nonhomogeneous medium (such as the human body) and the buildup of scattered photons in each projection during the acquisition process.

The approaches using attenuation correction maps have the potential to improve the accuracy of activity quantification over those that use a single effective attenuation coefficient, measured for a broad beam geometry, to describe attenuation in a nonhomogeneous medium. Essentially, the latter uses an attenuation coefficient which is smaller than the narrow beam value, thereby undercorrecting for absorption of primary photons in order to compensate for the contribution of scattered photons in the projection. This is done under the assumption that a fixed proportion of the absorbed primary photons can be replaced by scattered photons detected in the projection. However, this assumption can lead to significant errors (15). Certainly, it is incorrect to apply a single attenuation coefficient value to a nonhomogeneous medium, especially where there is significant variation in density such as the thorax and pelvis. Accurate correction maps can be derived from transmission-emission studies (27, 29) and computed tomography (28, 37, 38). Investigations where transmission and emission scans are obtained simultaneously, such as Tan *et al* (39), would provide ideal information for accurate quantification, however, would require hardware changes to most gamma camera systems.

1.3 Outline of Thesis

The primary objective of this research is to develop a practical, clinical method for accurate organ and whole body activity quantification using conjugate pairs of planar images and density maps obtained from computed tomography. Most of the investigations in activity quantification are currently performed using SPECT imaging. SPECT has the potential to provide accurate quantification, and in particular, it can be used to estimate the uptake in small localized regions. Unfortunately, in some procedures such as the intravenous administration of radiolabelled antibodies and ^{67}Ga citrate studies, the magnitude of uptake is too small for satisfactory quantification by SPECT imaging. In addition, whole body activity quantification (where the counts rates are low) by SPECT requires unacceptable acquisition times. For these procedures, planar imaging methods may be potentially more useful as they require shorter acquisition and processing times, are easier to implement and produce images of lower statistical uncertainty.

It is important to note that planar imaging has its limitation in that it suffers from an inability to take into consideration the 3-D nature of activity distribution and the attenuation process. However, the availability of whole body CT anthropomorphic data, has made it possible to develop a method in nuclear medicine that utilizes this 3-D information to solve this problem (40).

This thesis presents the theory and concepts of the proposed method, the relevant details involved in its development, an evaluation of the method using physical phantoms that simulate abdominal and thoracic regions of the human body and clinical applications using randomly selected patients. The thesis demonstrates the application of 3D information provided by CT for attenuation correction of planar images in nuclear medicine and the use of Monte Carlo simulated buildup factors to correct for the buildup of scatter in the two projections required by this method.

Following the introduction to nuclear medicine presented in this chapter, Chapter 2 presents the necessary background physics for understanding the fundamental concepts and principles of nuclear medicine imaging. A discussion is presented on photon propagation through matter, radioactivity and the Anger camera principles and limitations. In Chapter 3, approaches to attenuation and scatter correction are discussed with a view of providing an understanding of the problems and limitations that must be overcome in order to achieve accurate activity quantification. Chapter 4 presents the theory and concepts of a new method, developed by this research, for accurate activity quantification. In Chapter 5, experimental validation of the theory using physical phantoms is discussed. A description of the correction algorithm is also presented. In Chapter 6, clinical applications of the method are outlined and the combination of the patient nuclear medicine image and the computerized human model is described. The conclusions of the project are presented in Chapter 7 with a summary of the investigations of Chapters 5 and 6. In addition, a discussion of future work in regards to this project is presented in that chapter.

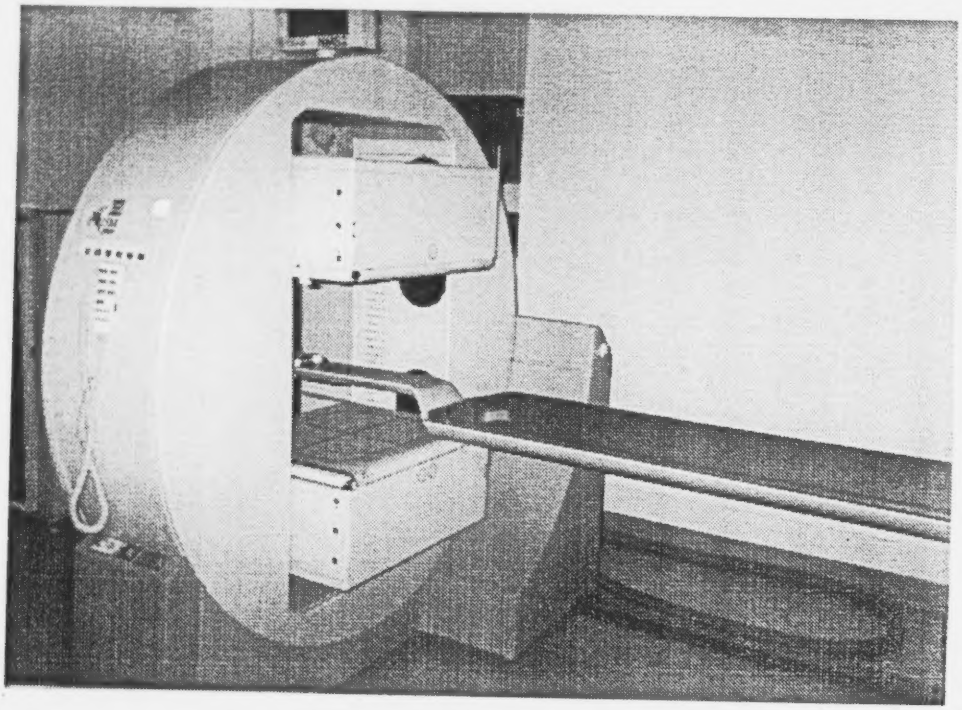

Figure 1. Example of dual head gamma camera used to acquire nuclear medicine images.

Chapter 2

Background Physics to Nuclear Medicine Imaging

2.1 Photon Propagation Through Matter

Fundamental to an understanding of the imaging process in nuclear medicine, are the mechanisms of the propagation of electromagnetic radiation in the form of gamma photons through matter and detection of the emitted radiation. When traversing matter, photons will either penetrate without interaction or interact and be scattered or absorbed. The combined effect of absorption and scatter is referred to as attenuation. There are four major types of photon interactions with matter: 1) Rayleigh scattering, 2) Compton scattering, 3) photoelectric absorption and 4) pair production. The first section of this chapter focusses on the first three because they occur in nuclear medicine and significantly affect the quantitative ability of this imaging modality. The fourth process, pair production, plays no role in nuclear medicine because it occurs at photon energies greater than 1.02 MeV, which is above the diagnostic energy range (70 - 360 keV), and is only mentioned here for the purpose of completion. In the second section of this chapter, the concepts of activity and activity calibration are presented. This is important because accurate determination of the activity of a radiopharmaceutical prior to its administration to a patient is an absolute requirement in nuclear medicine. In the third, the principles, performance and limitations of the instrument that is central to nuclear medicine imaging, the gamma camera, are discussed.

Compton Scattering

In Compton scattering a photon interacts with a loosely bound (free) orbital electron of an atom (41). In this process the photon loses a small amount of energy to the electron and is deflected through a scattering angle θ with respect to its original direction of travel. The electron departs at angle ϕ with momentum p and kinetic energy T, acquired from the interaction. This is illustrated in Figure 2(a). The energy of the scattered photon depends on the geometry of interaction and is given by the following relationship:

$$E'(E,\theta) = \frac{E}{1+\frac{E}{0.511}(1-\cos\theta)} \qquad (1)$$

where E and E' are the incident and scattered photon energies respectively, θ is the angle of the scattered photon with respect to the direction of the incident photon. The kinetic energy T transferred to the electron in Compton scattering is given by:

$$T = E - E' \qquad (2)$$

and ranges from nearly zero ("grazing" collisions) up to a maximum value that occurs for backscattering events where $\theta = 180^0$. The scattering angle of the electron can be obtained from the relationship:

$$\cot\phi = \left(1 + \frac{E}{0.511}\right)\tan\frac{\theta}{2} \qquad (3)$$

where ϕ is the electron scattering angle and has value $0 < \phi < 90^0$.

Compton scattering is the most common interaction process with soft tissue in the diagnostic energy range (8). The probability of a photon interacting in a Compton collision with a free electron and be scattered into a small solid angle, $d\Omega$, at angle, θ, with respect to the direction of the incident photon (Figure 2(b)), is given by the differential Klein-Nishina scattering cross section (42-44):

$$\frac{d_e\sigma(E,\theta)}{d\Omega} = \frac{r_0^2}{2}\left(\frac{E'}{E}\right)^2\left(\frac{E}{E'} + \frac{E'}{E} - \sin^2\theta\right) \qquad (4)$$

where E′ is defined in Equation 1 and $r_0 = e^2/m_0c^2 = 2.818\text{x}10^{-13}$ cm, is the classical electron radius.

Photoelectric Absorption

Photoelectric absorption is an interaction process in which a photon interacts with a tightly bound (inner shell) electron and is completely absorbed. The energy absorbed is used to overcome the binding energy, (BE), of the electron and to provide kinetic energy, T_e for ejecting the electron. The kinetic energy given to the ejected

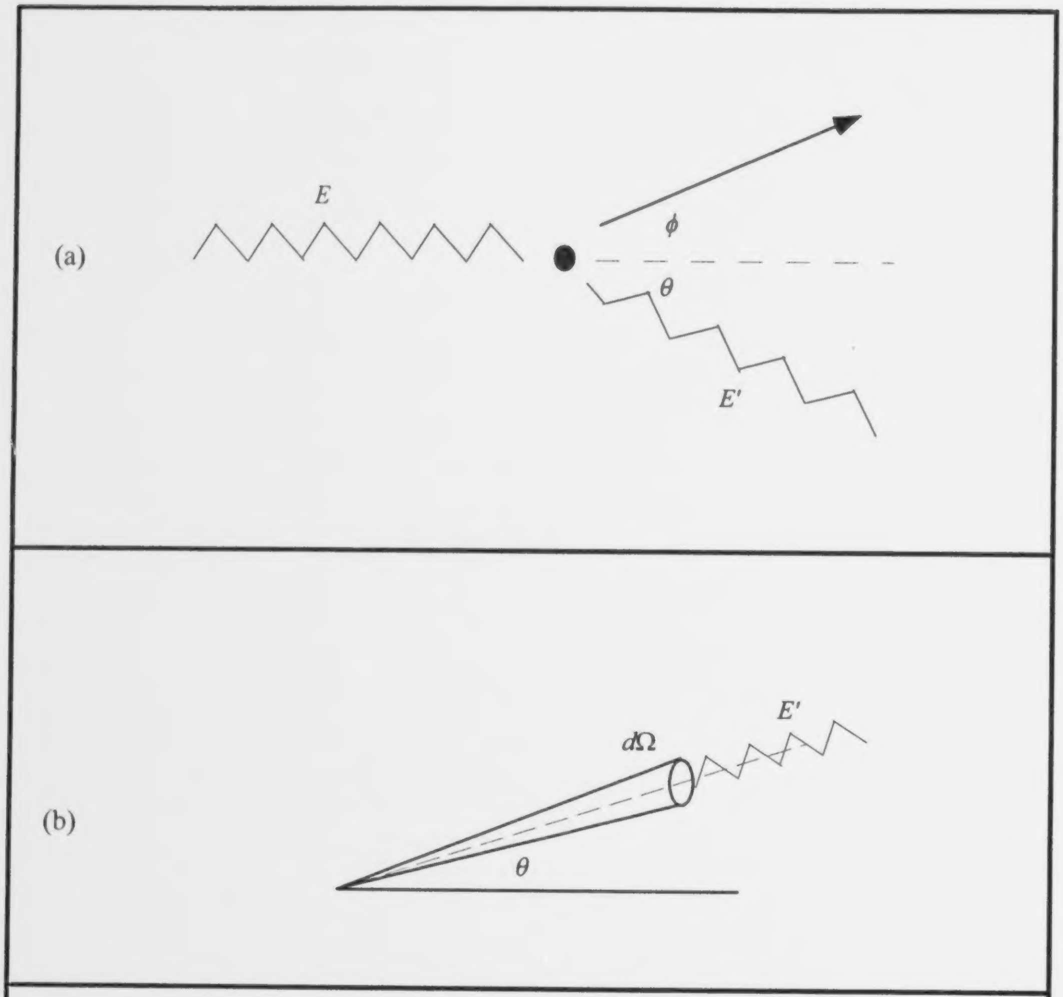

Figure 2: (a) Illustration of Compton scattering and (b) differential Klein-Nishina solid angle for scattering

electron is equal to the difference between the incident photon energy, E, and the binding energy, that is,

$$T_e = E - BE \tag{5}$$

It is important to note that: 1) this process cannot take place if the photon energy is less than the binding energy of the electron with which it interacts and 2) no scattered photons are produced in this process. The probability of a photoelectric interaction, τ, depends strongly on the photon energy and the atomic number, Z, of the absorbing medium. It is directly proportional to the fourth power of the atomic number and inversely proportional to the third power of the photon energy (43-45). That is,

$$\tau \, \alpha \, \frac{Z^4}{E^3} \tag{6}$$

Thus, photoelectric interaction is the dominant interaction process for low energy photons and high atomic number materials. Photoelectric absorption increases abruptly as the photon energy becomes equal to the binding energy of the orbital electron involved in the interaction and decreases rapidly, by a $\frac{1}{E^3}$ fall-off, as the photon energy exceeds the electron binding energy. Electron binding energies at which this takes place are known as absorption "edges".

Rayleigh Scattering

Rayleigh scattering (also called coherent or elastic scattering) is an interaction that occurs between a photon and an atom as a whole in which the photon is re-emitted with only a slight change in direction (i.e. scattered) and no loss of energy. Essentially, the incident photon (electromagnetic radiation) has an oscillating electric field associated with it that sets the electrons in the atom into momentary vibration. The oscillating electrons collectively emit electromagnetic radiation to form the scattered photon (44). Note that the oscillating electrons act as a whole (hence coherent) and the scattered photon has the same wavelength as the incident photon (hence elastic, since no energy is lost). This process generally takes place at relatively low photon energies and is rather infrequent in nuclear medicine, accounting for less than five percent of all interactions (8).

Attenuation under conditions of Narrow and Broad Beam Geometries

An arrangement of the radioactive source, attenuating medium and detector that is designed to minimize the recording of scattered photons is called *narrow beam geometry* (Figure 3(a)). Conversely, an arrangement in which many scattered photons are recorded by the detector is called *broad beam geometry* (Figure 3(b)). Narrow beam geometry requires that: 1) the beam be collimated at the source to ensure that a narrow beam is directed onto the attenuating medium and 2) the beam that exits the medium be collimated at the detector to prevent the detection of photons that are multiply scattered.

Unfortunately, nuclear medicine imaging is characterized by broad beam conditions, thus suffers from the effects of photons that have been multiply scattered. Some of these effects are described in the following section and methods to correct for them are discussed in Chapters 3 and 4. Under conditions of narrow beam geometry, the attenuation of a photon beam of intensity, N_0, directed onto an attenuator of thickness, T, can be described by the relationship:

$$N = N_0 e^{-\mu T} \tag{7}$$

where N is the photon beam intensity emerging from the attenuator and μ is the linear attenuation coefficient. The linear attenuation coefficient is defined as the fraction of primary photons that interact per unit thickness of attenuator (44). Strictly, μ is the total linear attenuation coefficient because it represents the sum of the interaction coefficients for the different interaction processes in the medium, that is,

$$\mu = \tau + \sigma_C + \sigma_R \tag{8}$$

where σ_C and σ_R are the Compton and Rayleigh scattering coefficients respectively, and τ is the photoelectric absorption coefficient. Thus μ is dependent on photon energy and the type of attenuating material.

Effects of the Interaction Processes

The interactions of gamma radiation from a radiopharmaceutical in a patient have three major effects in nuclear medicine. They decrease the available information about the study, degrade image quality and increase patient dose. The radiation emitted from a patient containing a radiopharmaceutical consists of two components. One is the primary radiation coming directly from the radioactive material (i.e. no interaction), and the other is the secondary radiation produced by Compton interactions in tissue. The former is desirable for nuclear medicine imaging while the latter is most undesirable, but there is no simple way of separating the two components.

A photon emitted from a given location in a patient may undergo several Compton scatter interactions before it is absorbed or exits the patient. If the photon escapes the patient and is detected by the gamma camera, it may be detected (recorded) at a location in the image that does not correspond to its location of origin in the patient. The lack of correlation between the location of origin and detected location of scattered photons results in a loss of resolution and degradation in image quality. This reduces the diagnostic quality of the image and affects the accuracy of activity quantification as counts from scattered events (misplaced photons) are added to the image.

The amount of absorption and scatter produced by a given radionuclide depends on the location and distribution of the radionuclide in, and the size of, the patient. For example, sources that are deep in the body will appear less active than identical sources close to the surface due to the removal of a greater proportion of primary photons by photoelectric absorption, thus producing a lower photon fluence at the detector. At the same time, the number of scattered events in the body increases resulting in an increased contribution of scattered photons in the image. This is demonstrated in Figure 4. Figure 4(a) shows a simple source-phantom configuration

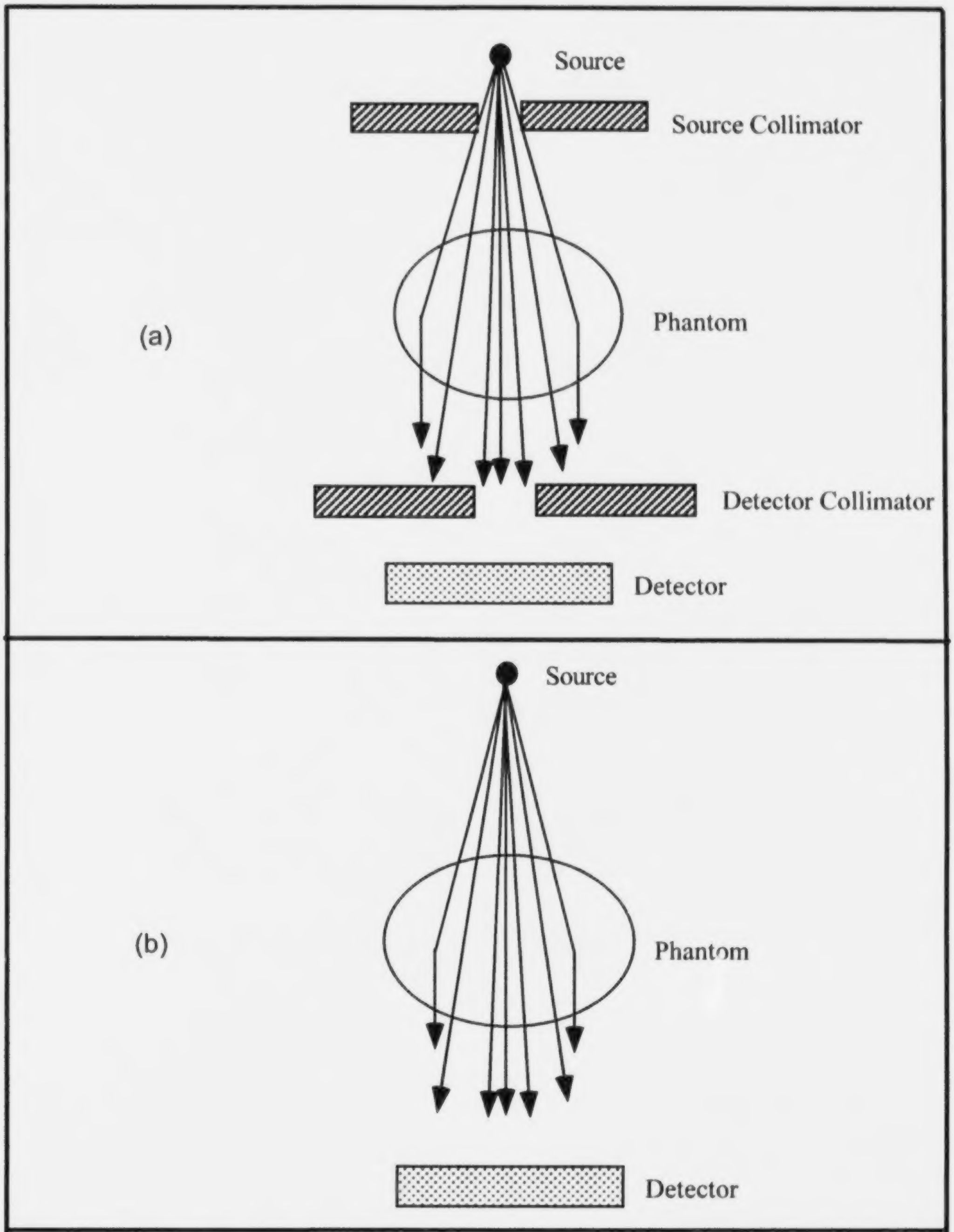

Figure 3. Narrow beam (a) and broad beam (b) geometries

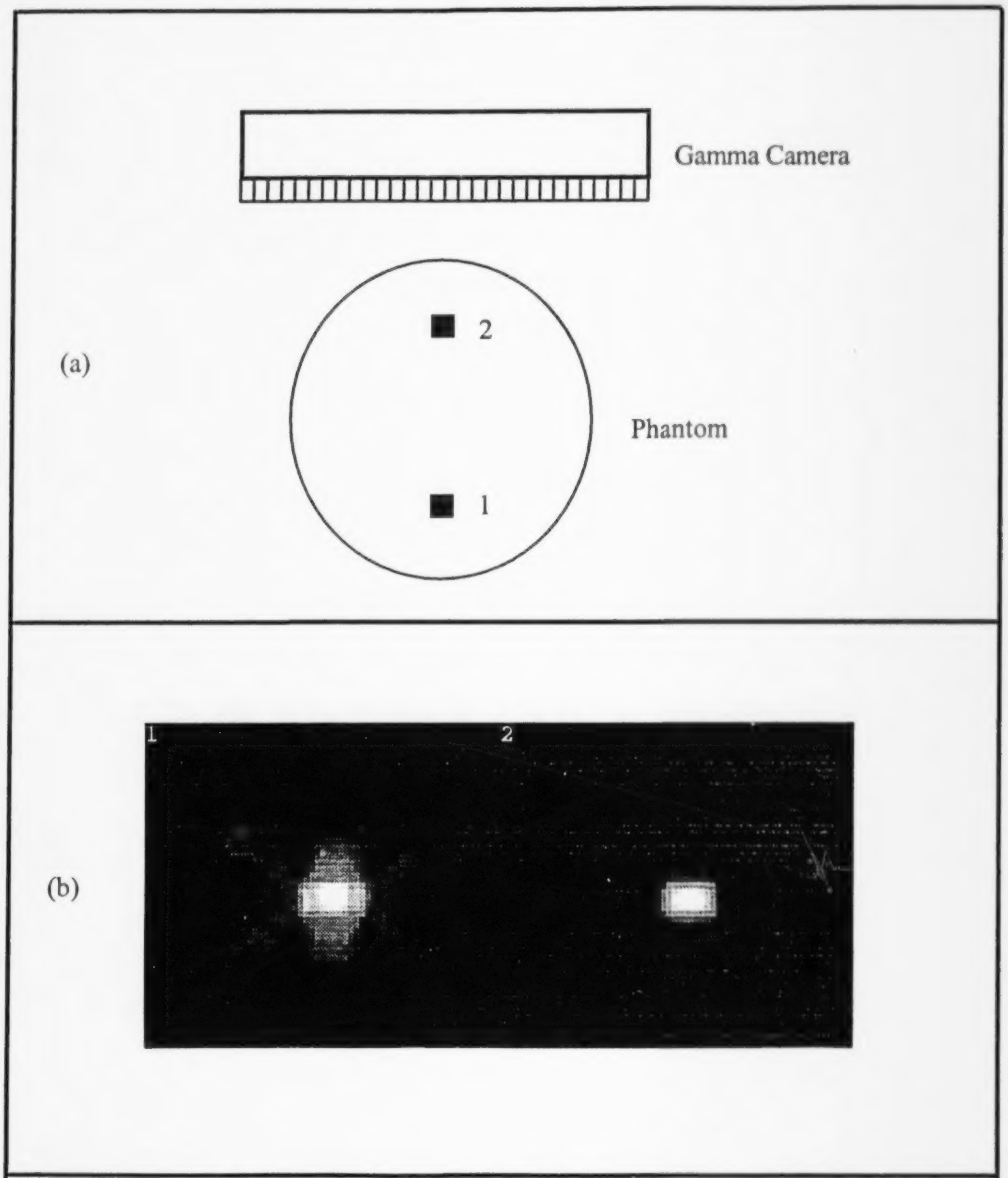

Figure 4. (a) Cross section of phantom with sources 1 and 2. Only one source present at any given time. 1 = 16 cm depth and 2 = 4 cm depth. (b) Images 1 and 2 correspond to source locations 1 and 2 respectively.

for a technetium-99m point source at different depths in a perspex phantom. The images obtained at two different source depths are shown in Figure 4(b). Note the well defined image of the line source at 4 cm depth as compared to the broadened and degraded image of the same source at 16 cm depth.

Nuclear medicine imaging procedures involve the use of quantities of radioactive material that are sufficient to produce an image of acceptable diagnostic quality while minimizing the radiation dose to the patient. The Compton and photoelectric interaction processes serve to increase patient dose as a consequence of energy deposition in the body from the interactions. It is important to note that energy absorbed (dose) from the interaction processes by the atoms and molecules of living cells in the body represents the first step in a complex chain of events that may ultimately lead to radiation induced damage. Further discussions on the effects of energy deposition in the body from the interaction processes can be found in textbooks on Radiobiology and will not be presented here. An excellent textbook on the subject is that of Hall (46).

2.2 Activity, Calibration and Radionuclides

Activity and Calibration

The *activity* of a radionuclide (or radioactive material) is the total number of atoms in it that disintegrate (decay) per unit time. The activity, $A(t)$, at anytime, t, is given by the relationship:

$$A(t) = A_0 e^{-\lambda t} \qquad (9)$$

where A_0 is the initial activity ($t = 0$) and λ is the *decay constant*. The decay constant is defined as the probability of a decay occurring per unit time (sec^{-1}) for a single atom. The decay constant has a characteristic value for each radionuclide. The unit of activity is the becquerel (Bq) and is defined as 1 disintegration per second. A terminology that is often associated with activity is the *half-life* ($T_{1/2}$) of the radionuclide. The half-life (also referred to as the physical half-life) is defined as the time required for the radionuclide to decay to 50 percent of its initial activity level. An important consideration in nuclear medicine in regards to patient dose is the time that it takes for the administered radiopharmaceutical to be eliminated from the body. This is expressed in terms of the *biological half-life* which is defined as the time required by the body to eliminate 50 percent of the radiopharmaceutical or any substance by the regular biological processes. The combined effect of the two is called the *effective half-life* and is given by the relationship:

$$\frac{1}{T_E} = \frac{1}{T_P} + \frac{1}{T_B} \qquad (10a)$$

or

$$T_E = \frac{T_P \cdot T_B}{(T_P + T_B)} \tag{10b}$$

where T_E is the effective half-life, T_B is the biological half-life and T_P is the physical half-life.

One of the most important steps in nuclear medicine imaging is the accurate measurement of the activity of a radionuclide (radiopharmaceutical) prior to its administration to a patient. The procedure is essential as this is the only way to ensure that a patient gets the prescribed activity for the desired investigation. This is often called the dose and is obtained by measuring the activity using a calibrated instrument called a *dose calibrator* or *activity calibrator*.

Radionuclides

Nuclear medicine imaging utilizes several radionuclides for organ investigations. Some examples are technetium-99m (140 keV), gallium-67 (93, 185, 300 keV), thallium-201 (68-80 keV), indium-111 (172, 247 keV) and xenon-133 (81 keV). However, technetium-99m is, by far, the most widely used radionuclide in nuclear medicine (47). This is due to: 1) its "ideal" physical properties and 2) the conception and development of the molybdenum-99/technetium-99m (^{99}Mo/^{99m}Tc) generator by Stang in 1957 at Brookhaven National Laboratory (48-50).

The practice of diagnostic nuclear medicine requires the use of radionuclides that have a high abundance of clinically useful photons and few, if any, particulate emissions. Gamma cameras are optimized for photon energies close to 140 keV, which is a compromise between photon attenuation in patients and detection efficiency. Photons whose energies are much lower than 140 keV are largely attenuated by the body, increasing patient dose without contributing to image formation. Those that are much higher than 140 keV escape the body but have poor detection efficiency. In addition, the radionuclide should have relatively short half-life, long enough to complete the study but short enough to minimize patient dose.

The characteristics of ^{99m}Tc satisfy these requirements making it "ideal" for nuclear medicine imaging. These characteristics include: 1) the emission of 140 keV gamma photons which are almost ideal for the energy range (70 - 360 keV) in nuclear medicine, 2) short half-life of 6 hours, 3) absence of beta radiation or any other particulate radiation that would only serve to increase patient dose, 4) readily combines with several pharmaceuticals to form appropriate radiopharmaceuticals and 5) practical availability to hospitals/medical centres worldwide through ^{99}Mo/^{99m}Tc generators.

The ^{99}Mo/^{99m}Tc generator is a system containing molybdenum-99 (called the parent), which has a relatively long half-life (67 hours) and continually decays to produce technetium-99m (called the daughter) in such a way that the technetium-99m can be separated for clinical use. This system provides a solution to the supply and storage problems that the relatively short half-life of technetium-99m would otherwise present.

2.3 Gamma Camera Imaging

The first nuclear medicine imaging devices were collimated Geiger-Muller detectors used in the late 1940s. They were used primarily to obtain mechanically scanned, point by point maps of the distribution of Iodine-131 (^{131}I) in the thyroid gland and required the use of large quantities of ^{131}I due to low efficiency of the detector. A significant advance occurred in 1951 with the introduction of the rectilinear scanner by Ben Cassen (51). The detector of the rectilinear scanner scanned over the organ of interest in a raster pattern forming the image line by line as a pattern of dots. The major drawback of the rectilinear scanner was that only a single resolution element could be viewed at any one time, thus scanning times were long and the scanner could not image rapidly changing radiopharmaceutical distributions in the body. In 1957, one of the most significant advances in nuclear medicine imaging devices was the introduction of the gamma camera or Anger camera by Hal Anger (52). With this system, all resolution elements within the organ or region of interest can be viewed simultaneously. Thus, it provided the capabilities for short imaging times and dynamic studies whereby rapidly changing radiopharmaceutical distributions can be imaged. It still forms the basis of nuclear medicine imaging today.

The performance and limitations of the gamma camera have significant effects on the diagnostic quality of the image obtained and the quantitative ability of this modality. In the following sections, a brief discussion of the basic principles of operation is presented and the functions of the major components and their influences on gamma camera performance are thoroughly discussed.

Basic Principles of Operation

The basic components of the gamma camera are shown in Figure 5. Essentially, the detector is placed over the region of interest (i.e. region containing the radiopharmaceutical) and as close as possible to the patient. The collimator is used to preserve the spatial distribution of the gamma photons emitted from the patient onto the front surface of the detector crystal as a gamma image of the radiopharmaceutical distribution. The photons interact with the crystal via photoelectric absorption and Compton scattering, thus deposit energy in the crystal. The energy deposited is converted by the crystal into light photons (i.e. scintillation). An array of photomultiplier tubes (PM tubes) viewing the back surface of the crystal collects the light photons and converts them into electronic signals. The signals from the PM tubes are fed into computing circuits (position and energy summation circuits) that use the input signal to determine the location and energy of the event. If the energy from the scintillation event lies within a predetermined energy window, the signal will be accepted and the corresponding image element will be incremented. A more detailed

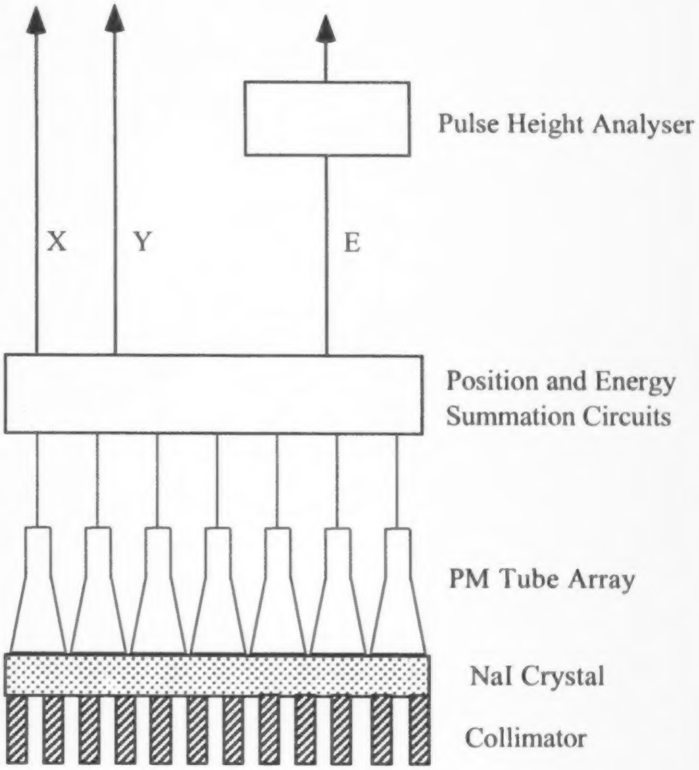

Figure 5. Basic components of the gamma camera

discussion of the functions, characteristics and effects of the major components is given in the following sections.

Collimators

The collimator plays an integral role in the image formation process. It is constructed from a metal that is a good absorber such as lead or tungsten and is used for projecting an image of the radiopharmaceutical distribution in the patient onto the front surface of the detector crystal. It consists of a regular pattern of closely spaced holes that are positioned so that each point on the crystal surface has a direct view of only one point on the surface of the body. The holes are separated by thin walls called septa. Thus the collimator restricts the direction from which photons traveling towards it are detected and only those photons within a certain acceptance angle, defined by the collimator hole geometry, are detected. Others are absorbed by the collimator. This process of collimation is referred to as *absorptive collimation* and determines to a large extent the spatial resolution of the gamma camera image. Absorptive collimation is an inherently inefficient process because most of the photons traveling towards the collimator are absorbed by it.

The performance of the collimator is characterized by its *efficiency* (sensitivity) and *resolution*. Collimator efficiency is the fraction of photons emitted by a source that pass through the collimator holes. This is typically a few percent or less (53). Collimator resolution is defined as the full width half maximum (FWHM) of the radiation transmitted through the collimator from a line source. Both characteristics are strongly affected by the size, shape and length of the collimator hole, the acceptance angle and septal thickness. Figure 6 shows the geometry for a parallel hole collimator. Holes can be hexagonal, round, square or triangular in shape, however hexagonal hole shape is generally used for close packing. The collimator resolution, R_c, for a source at some distance, b, from the collimator is given by the relationship:

$$R_c \approx d\left(\frac{l_e + b}{l_e}\right) \qquad (11a)$$

or

$$R_c \approx (l_e + b)\tan\theta \qquad (11b)$$

where l_e, is the effective length of the collimator hole, d is the hole diameter. Equation (11) indicates the dependence of resolution on the distance of the source from the face of the collimator. A large source to collimator distance results in poor resolution (Figure 7), hence it is important that the collimator be brought as close as possible to the patient for imaging. Small hole length and large hole diameter implies wide acceptance angle and results in poor resolution. This geometry, however , provides for increased collimator efficiency as a greater proportion of photons emitted by the source will pass through the collimator. Consequently, it is important that the design parameters of the collimator hole be chosen such that there exists a reasonable

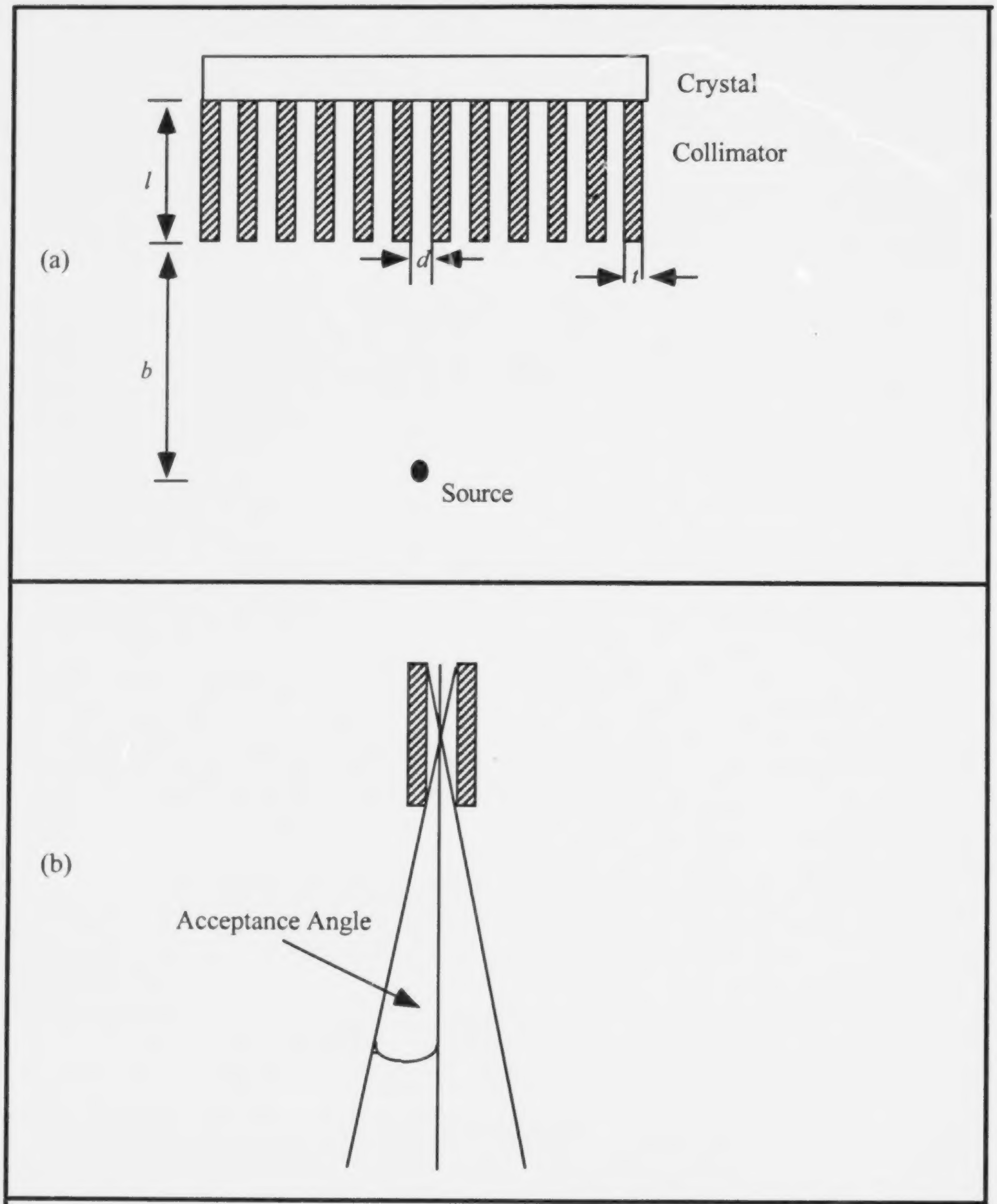

Figure 6: Illustration of collimator geometry and acceptance angle

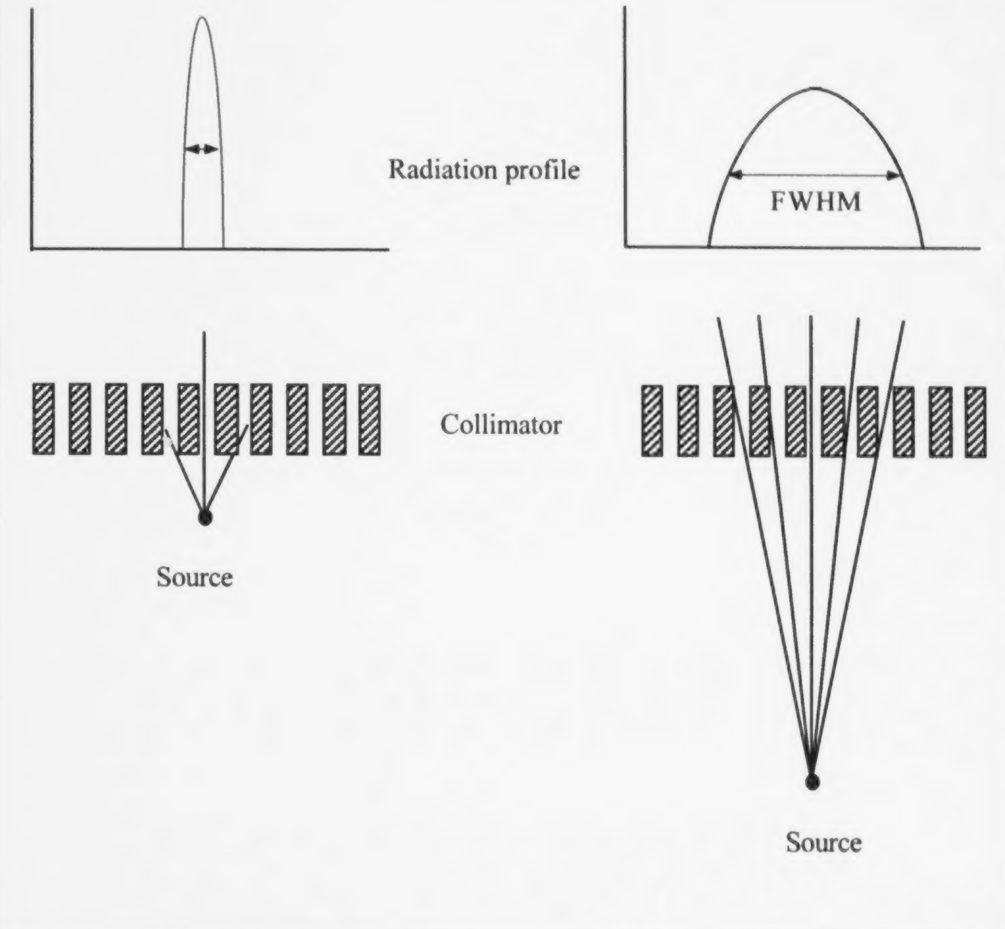

Figure 7. Illustration of changes in collimator resolution with source to collimator distance

compromise between collimator efficiency and collimator resolution. The conflicting constraints between efficiency and resolution is the single most significant limitation on gamma camera performance.

The influence of septal thickness on resolution and efficiency is also very important. A primary concern in collimator design is to ensure that septal thickness is sufficient to prevent photons from penetrating through a septum while minimizing the total area occupied by the septa. If the septal thickness is too thin for the energy of the radionuclide to be detected, significant septal penetration will occur and the image will appear blurred (i.e. poor resolution). It is generally required that septal penetration be less than 5 percent. This is essential if a spatially accurate gamma image is to be projected onto the crystal. The desired septal thickness depends on the energy of the gamma photons to be detected. For low energy photons (e.g. ^{99m}Tc, 140 keV), a collimator with relatively thin septa (low-energy collimator) is adequate. This provides for higher sensitivity resulting from increased holes per unit area due to thin septa. Typical septal thickness for low energy collimators is less than 0.5 mm lead (53). However, for higher energy photons, a collimator with relatively thick septa (medium energy collimator) is required which implies fewer holes per unit area and therefore reduced sensitivity.

There are several types of collimators, each designed with different hole orientations for specific functions. These include parallel hole, converging, diverging, fan beam and pin hole collimators. The parallel hole collimator consists of holes that are parallel to each other and perpendicular to the face of the detector crystal. It projects a gamma image onto the detector crystal that is the same size as the actual radionuclide distribution in the patient. They are the most frequently used collimators in nuclear medicine. A converging collimator consist of holes that converge to a focal point in front of the collimator. This collimator projects a magnified image of a source placed between the collimator face and the focal point. A diverging collimator consists of holes that diverge from the collimator face. It produces a minified image of an object placed in front of it and the minification increases as the object is moved away from the collimator. A fan beam collimator is a hybrid of the converging and parallel hole collimators and is generally used in SPECT imaging. It consists of holes that converge along a line parallel to the axis of rotation. Collimators of the converging type provide increased sensitivity because the object is viewed by more holes, thus "sees" a larger area of the crystal. They are useful for imaging small organs.

Detector Crystal

The detector crystal is a thin (~ 13 mm) large diameter (40 - 50 cm) sodium iodide-thallium activated, (NaI(Tl)), crystal. The function of the crystal in the gamma camera is to absorb gamma photons and convert them into light photons. The crystal is hermetically sealed in an aluminum "can" with a transparent glass (optical window) at one side to permit the exit of scintillation light from the crystal to the PM tubes. Typical aluminum thickness is less than 1 mm. The inside surface of the aluminum jacket is coated with a white aluminum oxide reflector to reduce loss of light. Gamma photons projected onto the crystal will interact with, and transfer energy to, orbital electrons in the crystal. Sodium iodide has a relatively high atomic number due to iodine (I, atomic number = 53) and so most of the interactions will be photoelectric absorption (Section 2.1). Approximately one light photon is emitted in the NaI(Tl) crystal for every 25 eV of energy deposited by the gamma photon (8, 53). For example, when a ^{99m}Tc (140 keV) photon is absorbed by the crystal, approximately 140,000/25, i.e. 5,600 light photons are produced. The light photons exit the crystal via the glass window at the back surface and are subsequently collected by the PM tubes.

Photomultiplier Tube Array and Computing Circuits

The backsurface of the NaI(Tl) crystal is viewed by an array of PM tubes that are optically coupled to the glass window at the backsurface of the crystal. A transparent optical coupling grease is used between the crystal and the PM tubes to minimize internal reflection. The function of the PM tubes is to convert the light (scintillation) photons into electrical signals and to amplify them. Each PM tube consists of a photocathode and a set of dynodes (typically 8 - 10) enclosed in an evacuated glass tube. The photocathode is a photoemissive surface located on the inside front surface of the PM tube entrance window (i.e. the area viewing the crystal). The dynodes are coated with a material having relatively high secondary emission characteristics. Light photons from the crystal interact with the photocathode and eject electrons from it by the photoelectric process. The electrons are accelerated and focused onto the first dynode by a voltage difference between the dynode and the photocathode. Each incident electron ejects several secondary electrons from the dynode. These electrons are then accelerated and focused onto the second dynode by an identical voltage difference between the first and second dynodes. This multiplication process continues at each dynode stage until the electrons are collected at the anode. Thus the initial current pulse produced by a flash of light is amplified by the PM tube to a measurable output signal which is proportional to the number of light photons that the PM tube collects.

Generally, a scintillation event in the crystal is viewed by several PM tubes. The fraction of photons collected by each PM tube depends on its location with respect to the event. Those closest to the event will collect most of the light photons, thereby providing the largest output signals. The signal from each PM tube is further amplified and subsequently divided into two signals. One signal goes to the positioning circuit to determine the coordinate (x,y) location of the event in the crystal and the other goes to the energy summation circuit. The energy summation circuit sums the signals from the PM tubes to produce a signal that is proportional to the total number of light photons collected by the PM tubes, which in turn is proportional to the energy deposited in the crystal by the gamma photon. If this signal falls within a predetermined energy range (energy window), then it will be accepted and stored in an image matrix at the location determined by the positioning circuit. Otherwise, the signal will be rejected and will not contribute anything to the image.

Intrinsic Efficiency, Energy and Intrinsic Resolution

The performance of the NaI crystal and electronic circuitry of the gamma camera is determined by several parameters. These include energy resolution, intrinsic spatial resolution and intrinsic efficiency. The energy resolution of the gamma camera is a measure of its ability to distinguish between events depositing different energies in the crystal. It is characterized by the FWHM (Full Width, Half Maximum) of the photopeak energy of the radionuclide, divided by the photopeak energy, and is typically 10 - 15 percent for ^{99m}Tc, 140 keV photons. Intrinsic spatial resolution is a measure of the ability of the NaI crystal and electronic circuitry to accurately distinguish separate radioactive sources or different activity concentrations that are in close proximity. It is primarily affected by statistical fluctuations associated with the scintillation events in the crystal, the collection of light photons by the PM tubes and subsequent production of electrical signals. Approximately two-thirds of the scintillation photons reach the photocathode of the PM tubes and typically, only 20 - 25 percent of the light photons that are incident on the photocathode will contribute to the electrical signal from the PM tubes (8).

Intrinsic spatial resolution is also affected by the thickness of the NaI crystal. A thin crystal permits less spreading of light before reaching the PM tubes hence improves resolution. However, a thin crystal will absorb fewer gamma photons and therefore reduces the intrinsic efficiency of the camera. Thus, there is a design compromise between the intrinsic efficiency of the camera, which increases with crystal thickness, and intrinsic resolution, which degrades with crystal thickness. The intrinsic efficiency is also affected by the energy of the incident photon. Photon energies that are too high will result in less photoelectric absorption in the crystal, thereby reducing the efficiency of the camera.

Effect of Count Rate on Detector Performance

Every radiation detector requires a finite time to process (record) an event. This finite time is called the *deadtime*. During this time, the camera is unable to process any other event and valid interactions will be ignored (lost). In the gamma camera, the minimum deadtime is determined by the scintillation process in the NaI crystal and the associated electronics. In clinical nuclear medicine, deadtime values for gamma camera systems are typically in the range 2 - 10 μsec, depending on the aforementioned factors, source scatter geometry and selected energy window (53). For a 5 μsec deadtime, approximately 10 percent of the counts are lost at a count rate of 2×10^4 cps. If a second event (interaction) occurs during the processing time interval of the first, the two events will be perceived by the electronic circuitry as a single event. Consequently, if one of the events were within the photopeak window, the combined apparent energy of the two events will exceed the acceptable energy window, thus both events will be rejected. This phenomenon is known as *pulse pileup* and occurs at high count rates. Pulse pileup can produce significant count losses for "hot" sources resulting in artificially low count rates, thereby affecting the accuracy of activity quantification.

Random Errors in Image Counts

The disintegration rate of the radioactive sources used in the experiments undergoes random variations from one moment to the next. Thus, the counts recorded in successive measurements of a source are not exactly the same. This variation can be described by a Poisson distribution. One solution is to take a large number of measurements and use the average counts as an estimate of the "true value". However, in nuclear medicine imaging, this would require multiple image acquisitions of the same source distribution and geometry. This is impractical in routine nuclear medicine imaging and generally the imaging procedure is done once for a given source distribution and geometry. The error associated with counts in the image obtained is given by $SD = \sqrt{N}$, where SD is the standard deviation for a radioactive sample and N is the number of counts. The number of counts in the image is determined from ROIs drawn around the images.

Chapter 3

Correction Methods for Accurate Activity Quantification

As indicated in the Introduction (Chapter 1), the two most influential factors on the accuracy of activity quantification are Compton scatter and photoelectric absorption. Consequently, most of the investigations in activity quantification are focussed on ways of correcting for these phenomena and subsequently provide for accurate activity quantification. Several correction methods have been proposed, some dating as far back as the late 1960s (54, 55). In this chapter, the fundamental principles, applications and limitations of some of the methods are discussed under three broad categories: 1) window methods, 2) broad beam linear attenuation coefficients and attenuation correction maps and 3) buildup factors.

3.1 Window Methods

Dual Energy Window Method

Ehrhardt and Oberley (56) proposed the use of dual energy windows in 1972 to correct for Compton scatter in rectilinear scanning. The technique was subsequently applied to gamma camera planar imaging by Bloch and Sanders (10) in 1973 and to

SPECT imaging by Jaszczak *et al.* (15) in 1984. It is achieved by first obtaining images in two energy windows, the conventional photopeak window and a lower-energy scatter window, simultaneously (Figure 8). Compton corrected images can then be obtained by subtracting a fraction, k, of the Compton region image, I_s, from the photopeak image, I_p. The corrected image, I_{cor} is given by:

$$I_{cor} = I_p - k \cdot I_s \tag{12}$$

The dual energy window method is based on the assumption that the image obtained from events collected in the secondary window is a close approximation to the spatial distribution of the scattered photons detected in the photopeak window. This assumption is incorrect because the scattering angles of photons detected in the secondary window are different from those for the scattered photons detected in the photopeak window. This is evident from Equation 1 whereby for an energy window of 126 keV - 154 keV (typical ^{99m}Tc, 140 keV photopeak window), photons will have scattering angles between 0° and 53°, and for a secondary window of 92 keV - 125 keV (typical), photons will have scattering angles of between 55° and 154°. In addition, the probability that photons may have undergone multiple scatter is greater for those detected in the secondary window than for those detected in the primary window. Hence, the scattered photons detected in both windows are not from the same location in the object (patient) and therefore it is inappropriate to use one to make corrections on the other.

The accuracy of the correction will depend, to a large extent, on the value of *k*. This will vary with scatter distribution within the spectrum which is dependent on source size, acquisition geometry and energy resolution of the camera (17, 19, 57-63).

Changes in the proportion of scatter in different energy intervals of the spectrum with source depth have been reported by Filipow *et al.* (64). In addition, distortion is introduced in the spectrum when distributed sources are used and background activity is present (65). Also there is significant difference in the scatter/photopeak ratio for different organs (66), and the estimated scatter distribution from the lower energy window is not identical to the shape of the scatter distribution within the photopeak window, hence it is difficult to achieve accurate correction (59, 60, 63).

The primary task of this method is to determine the value of k that optimizes the correction procedure for a specific class of source geometry and energy window settings. The value of k can be determined analytically (10), experimentally (15, 56, 63, 67-69) or by Monte Carlo simulations of the systems (59, 60, 62). However, a variable k value might be necessary in order to improve accuracy.

Dual Photopeak Window Method

King *et al.* (18) proposed the possible use of a dual photopeak window method for Compton scatter correction in SPECT and planar imaging. The basis of this method of scatter correction is that Compton scattered photons contribute more to the lower energy portion of the photopeak than to the high energy side. In this method the photopeak window (20% symmetric energy window) is divided into upper and lower halves (Figure 9) and a regression relationship established between the ratio, R_c, of counts within each of the halves and the scatter fraction, S_f, for the counts within the total photopeak window. The regression relationship is expressed by:

$$S_f = A{R_c}^B + C \tag{13}$$

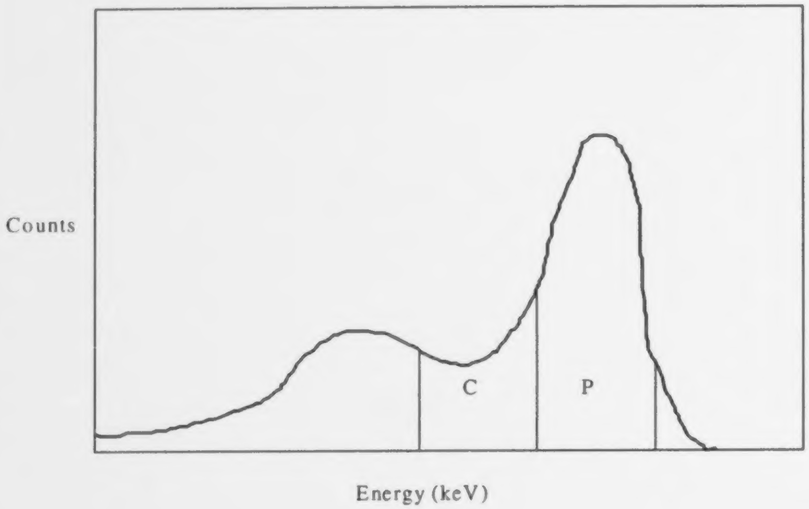

Figure 8. Dual energy windows with lower energy scatter window,C,and photopeak window, P.

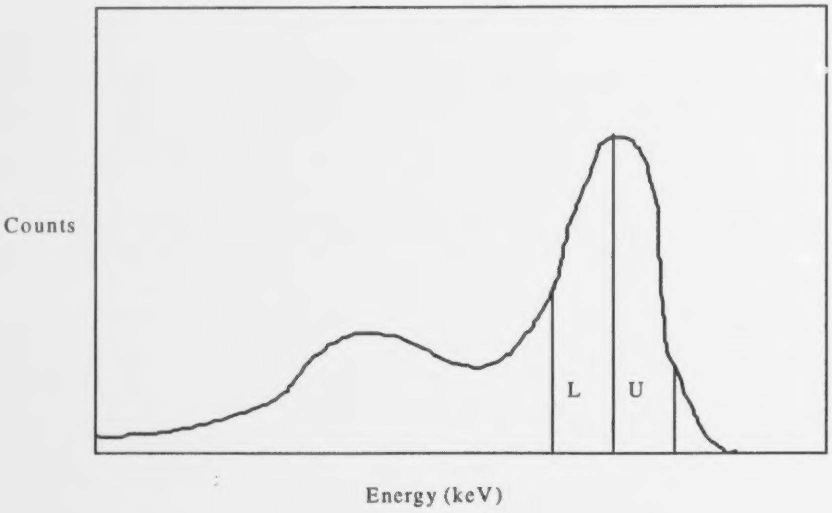

Figure 9. Dual photopeak windows with lower half, L, and upper half, U.

where $R_c = \frac{I_{uw}}{I_{lw}}$, I_{uw} and I_{lw} are the image counts in the upper and lower energy windows respectively. A, B and C are regression coefficients which are determined experimentally.

The method produced accurate results for phantom studies (18) and has potential applications for scatter correction in organ activity quantification. However, there are some limitations associated with the use of this method. For low count images it may produce scatter estimates that are noisy since only half of the photopeak events are used for forming each image. For good counting statistics, increased imaging time would be required which would increase the likelihood of patient motion artifacts and reduce the number of cases that can be done when compared to similar camera systems employing the full photopeak window for each image.

A common limitation presented by this method is the increased number of energy windows that are required for simultaneous acquisition of radionuclides of multiple energy photons such as gallium-67, thallium-201 and indium-111 which cannot be achieved on most of the currently available gamma cameras. In addition, it requires that calibration studies be done for each system and pair of energy windows to determine the regression coefficients of Equation 13. The calibration studies are done using physical phantoms, therefore the regression coefficients obtained are not truly representative of the clinical situations for which they are to be applied. In addition, the principle of the method makes it sensitive to gamma camera electronic drift, hence it may be necessary to redo the calibration studies periodically to maintain accuracy.

Asymmetric Window Method

Rejection of scattered photons in the image can be improved by setting the energy discriminator so that the energy window is shifted slightly to the higher energy region of the photopeak. In other words, the lower energy cutoff is closer to the photopeak energy than the higher energy cutoff (Figure 10). This technique was initially proposed for rectilinear scanning (54, 70-73) and subsequently applied to gamma camera planar imaging (9, 12-14) and SPECT imaging (17). The rationale behind this is that Compton scattering will reduce the energy of the scattered photons enough to allow discrimination through energy window selection.

Several studies have demonstrated improved contrast and quantification using this method (9, 12-14, 17). However, the method presents several drawbacks. The energy loss from each scattering event is not large enough to allow for discrimination of all scattered events through energy window settings. For example, ^{99m}Tc photons (140 keV) undergoing scatter of angles up to 45 degrees will still be within an energy interval that is only 7% below the photopeak energy. Thus, there exists great likelihood for scatter to be included even when a narrow window is selected. In fact, given the energy resolution of a NaI(Tl) gamma camera (10 - 15%), scattered events would be detected even with the lower baseline value set at the photopeak energy. Another problem with this technique is that primary photons are being eliminated while excluding scatter, thus reducing the sensitivity of the system. Furthermore, if the window is made too narrow in an effort to reduce scatter, then a compromise would have to be made between poor counting statistics and significantly increased acquisition time, neither of which is desirable. Thus, there is no location of the energy discriminator that can optimize the correction process.

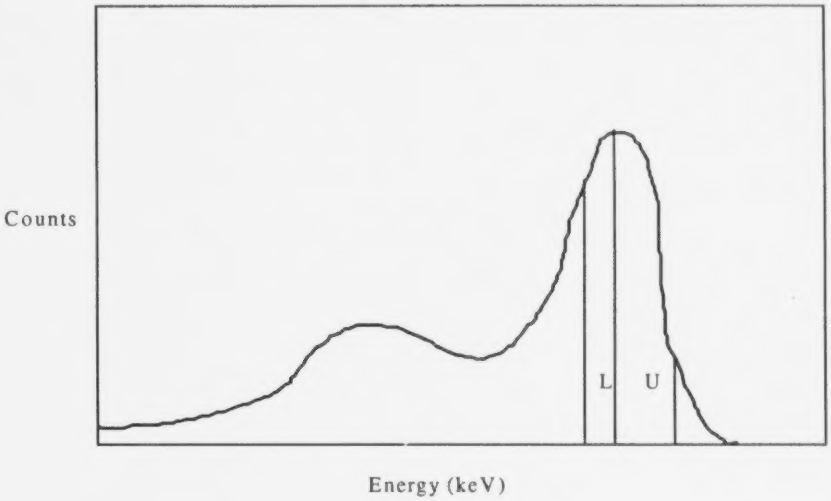

Figure 10. Asymmetric energy windows with lower photopeak window, L, shifted towards the upper photopeak window, U.

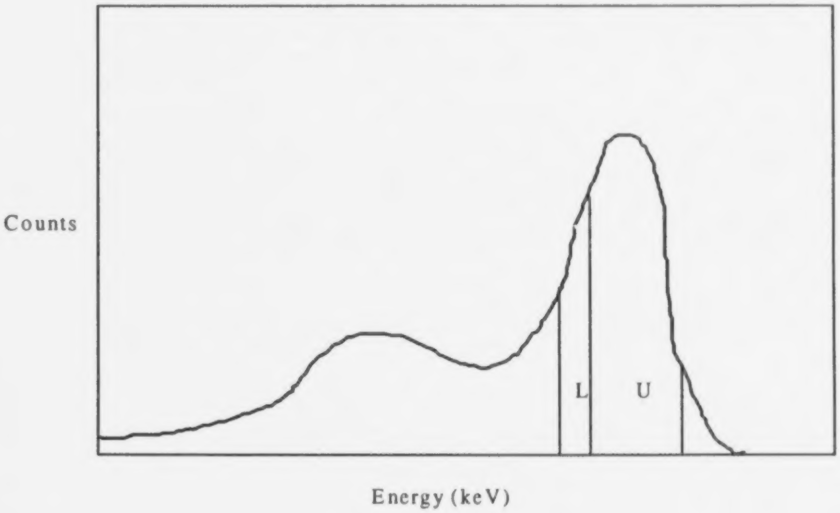

Figure 11. Asymmetric energy windows with upper photopeak window, U, extended to the lower photopeak window, L.

Logan and McFarland (74) have proposed a variation of this method whereby the conventional photopeak window is selected and is divided into two unequal subwindows (Figure 11). The scatter content of the two subwindows is assumed to be the same and the corrected image I_{cor} is given by the difference between the upper photopeak energy window image I_{upw} and the lower photopeak energy window image I_{lpw}. That is,

$$I_{cor} = I_{upw} - I_{lpw} \tag{14}$$

This approach results in significant loss of gamma camera sensitivity because a large percentage of unscattered photons is removed. For the reported study (74), about 20 percent of the unscattered photons are removed. This relatively large rejection of primary photons prevents accurate quantification and thereby reduces interest in this approach. In addition, the selection of the line dividing the photopeak is crucial for the accuracy of this method and may vary across the face of the camera due to changes in energy response as reported by King *et al.* (18).

3.2 Attenuation Coefficients and Correction Maps

One of the underlying problems with some of the proposed methods of correction for attenuation and the buildup of scatter in projection data, is the assumption that the human body is homogeneous. A common approach to correction is to use an effective linear attenuation coefficient, μ_{eff}, measured for a broad beam geometry, thus including the detection of scattered events (Section 2.1) rather than the theoretical (tabulated) value of μ that corresponds to narrow beam geometry where scattered photons are excluded. Typically, for a tissue equivalent material such as water and 140 keV photons, μ_{eff} = 0.12 cm^{-1} and μ = 0.15 cm^{-1}. This approach assumes that a proportion of the absorbed primary photons can be adequately compensated for by scattered photons detected in the projection. However, as Jaszczak *et al* (15) and Gilland *et al* (75) have shown, this assumption can result in significant errors.

The fundamental problem with this approach is that the body consists of different tissue types, each with a different density and cannot be correctly represented by a single linear attenuation coefficient value. For example, the thorax contains bone (density = 1.85 gcm^{-3}), soft tissue (density = 1.0 gcm^{-3}) and lung (density = 0.3 gcm^{-3}) which vary significantly in their attenuating capabilities. Therefore, appropriate correction requires the use of correction maps that take into account the different tissue types and accurately describe the density distribution in the body. These maps can be obtained from transmission imaging in SPECT or computed tomography (CT). In the following sections, some of the methods using: 1) a single effective linear attenuation coefficient value and 2) correction maps are discussed.

Geometric Mean Method

Estimation of corrected count rates, C_{cor}, from a source in an attenuating medium can be obtained from the geometric mean of anterior and posterior gamma camera images (22, 76) as indicated in Figure 12 using the relationship:

$$C_{cor} = \left(C_a \cdot C_p\right)^{1/2} \cdot \exp\left(\mu_{eff} T / 2\right) \tag{15}$$

where T is the thickness of the phantom (patient), μ_{eff} is the broad beam linear attenuation coefficient and C_a and C_p are the anterior and posterior count rates. The attenuation correction term, $\exp\left(\mu_{eff} T / 2\right)$, is derived from the equation:

$$N_t = N_o \cdot \exp\left(-\mu_{eff} T\right) \tag{16}$$

where N_o is the count rate from a transmission source in air and N_t is the count rate obtained with the patient placed between the source and detector. This method has useful applications but suffers from a major drawback inherent in its principle. The major drawback with this method is the fact that it assumes constant attenuation of photon intensity with source depth, hence does not correct for the contribution of scatter to the counts obtained. This assumption is not valid for the relatively wide window settings used in nuclear medicine. It has been shown that the broad beam linear attenuation coefficient varies from 0.081 cm^{-1} for a source at 1 cm depth to 0.122 cm^{-1} for a source at 15 cm depth in tissue equivalent material using a 30% window (77). In addition, the method does not take into consideration the effects of source thickness and inhomogeneity of the attenuating medium. Source thickness and inhomogeneity effects in vivo may be as high as 20% each (78). There are reports of overestimation of activity, by this method, of 42.6% to 50.9% using ^{111}In as tracer (76) and up to 20% for distributed ^{99m}Tc sources (79).

Fleming (23) adopted a modified approach to this method using anterior, posterior and lateral images. The lateral image is used to determine source thickness which is accounted for in the correction using the equation:

$$C_{cor} = \left(C_a \cdot C_p\right)^{1/2} \cdot \exp\left(\mu_{eff} T / 2\right) \cdot \left(\mu_{eff} X/2 \,/\, \sinh \mu_{eff} X/2\right) \tag{17}$$

where X is the source thickness and the other terms are as before. It has been shown (22) that correction for source thickness will provide slight improvement in the accuracy of the method. One of the problems associated with this approach is the need for accurate thickness measurement from the lateral image. Typically, an error of 1 cm in thickness measurement produces 5 percent error in activity quantification by this approach (23, 78). In addition, the fundamental problem presented by the use of a single linear attenuation coefficient value remains unsolved.

Transmission-Emission Method

The use of transmission measurements for error correction was first described by Evans (80) in 1937 for whole body counting. The method has been adopted by several investigators for planar imaging (20, 22, 81) and SPECT imaging (29, 30, 34, 39, 82-84). The setup for transmission-emission imaging generally requires that a line or flood source be mounted (placed) opposite to the face of the gamma camera and the patient centrally placed between the source and camera. Figure 13 shows a typical setup for a line source. The images can be acquired using two approaches: 1) the transmission image is acquired prior to the emission image and 2) the transmission and emission images are acquired at the same time (simultaneous transmission-emission imaging). The general form of the correction term for both approaches is given by Equation 16. In the first case, a transmission image of the patient is acquired followed by an in air image of the transmission source. After injection of the radiopharmaceutical into the patient, emission images are then acquired with the patient placed in the same position, hopefully, that the transmission image was obtained. This approach has the advantage of the same radionuclide being used for the transmission and emission sources and does not suffer from the problem of cross contamination of scatter (see second approach below) since the two images are acquired separately. However, it suffers from two major disadvantages: 1) the acquisition time is significantly increased and 2) there is significant likelihood of errors due to inaccurate spatial correlation between the transmission and emission images that are separately acquired. Macey and Marshall

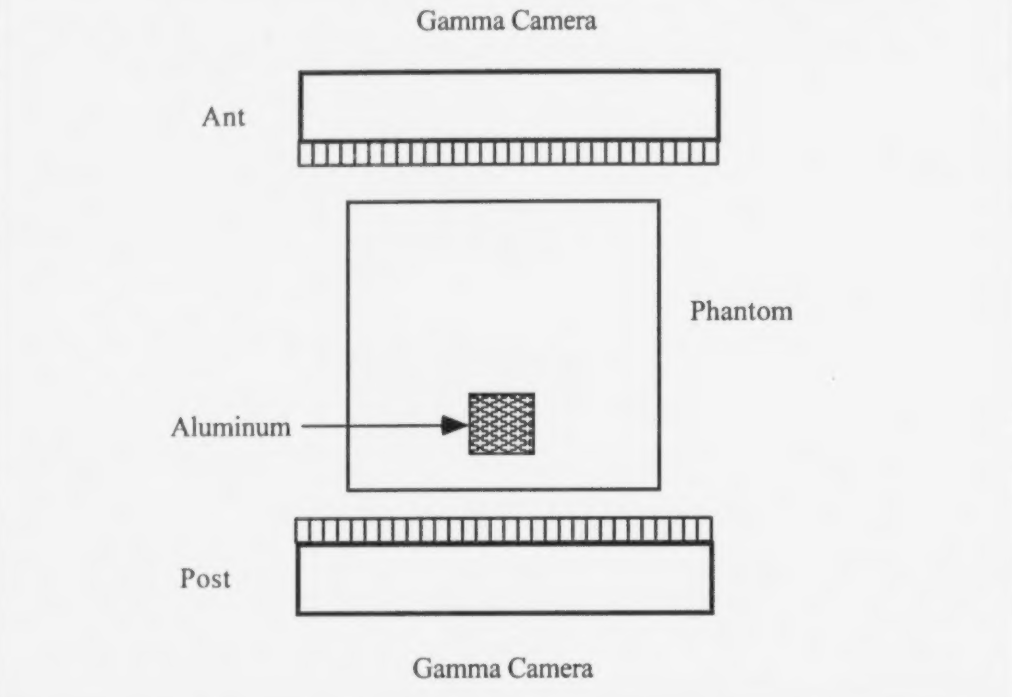

Figure 12. Geometry of nonhomogeneous phantom and gamma cameras

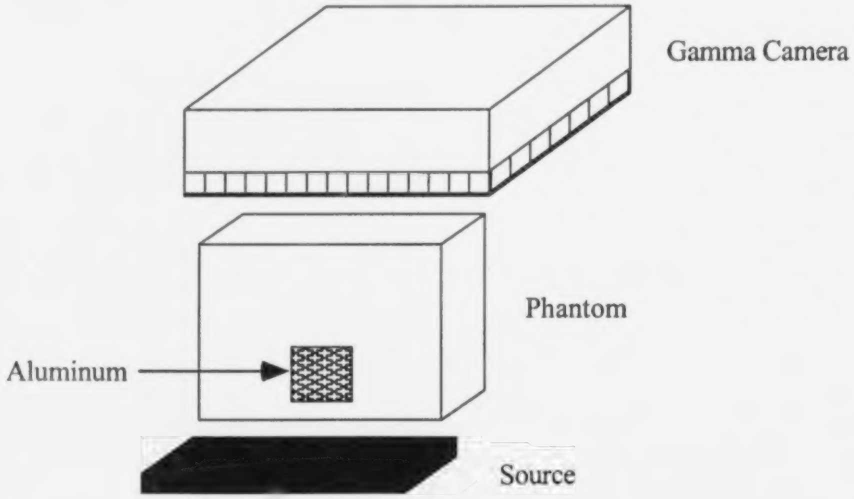

Figure 13. Geometry of setup for transmission measurement using a flood source

(22) applied this approach to planar imaging and reported that errors of less than 10 percent were achievable for soft tissue and bone activity quantification.

The second method has the advantage of reduced imaging time and better spatial correlation between the transmission and emission images since they are acquired simultaneously, but requires the use of two different radionuclides (i.e. photon energies). Generally the higher energy radonuclide (e.g. ^{99m}Tc, 140 keV) is used as the emission source and the lower energy radionuclide (e.g. ^{153}Gd, 98 and 103 keV) is used as the transmission source. This is done to prevent cross contamination of the emission data with scattered photons from the transmission study. However, corrections must be made to the transmission data to remove contamination due to scattered photons from the emission study. Note that there is always the likelihood of scattered photons from the higher energy radionuclide being detected in the energy window for the lower energy radionuclide.

Different techniques have been applied to correct for scatter contribution from the emission source in the transmission image (83, 84). Tan *et al* (39) used a tightly collimated scanning line source and electronically collimated detector for SPECT imaging and reported improved accuracy. However, the accuracy of simultaneous transmission-emission imaging will depend, to a large extent, on the ability of the technique applied to eliminate cross contamination of the emission and transmission data. In addition, this approach requires hardware changes to most cameras in order to provide support for a flood or scanning line source. Recently, some gamma camera manufacturers have started to provide these hardware requirements on their systems.

Some investigators who have adopted this method have used the same radionuclide for the transmission and emission sources. They therefore used the attenuation coefficient calculated from the transmission source as the emission source attenuation coefficient. Strictly, this is not correct because the measuring conditions are different. The effects of scattered radiation are considerably greater for an internal source than an external source and will produce different attenuation coefficients (78). Thus accurate quantification requires that the various exponential coefficients be determined separately. In addition, if transmission and emission scans are done separately care must be taken to ensure accurate spatial correlation between both and whenever possible, simultaneous transmission-emission scans should be done instead.

Chang Algorithm

The Chang attenuation correction algorithm (24), developed for SPECT imaging is currently used by some gamma camera manufacturers. In this technique, the reconstructed images are multiplied by a correction matrix obtained from the relationship;

$$C(x,y) = \left[\frac{1}{M} \sum_{i=1}^{m} \exp\left(-\mu l_{\theta_i}\right) \right]^{-1} \qquad (18)$$

where M is the number of projections, l_θ is the distance between point (x, y) and the boundary of the medium at projection angle, θ. The attenuation correction factor is an average value over all projection angles. The technique provides good approximate correction in uniformly attenuating media but may produce regions of overcorrection or undercorrection in nonhomogeneous media because it relies on the use of an effective linear attenuation coefficient value. However, the technique can be applied with some success to nonhomogeneous media by modifying the exponential term to produce an attenuation correction map that accounts for variation in linear attenuation coefficients (83).

3.3 Buildup Factor Method

The attenuation of photons in nuclear medicine imaging involves broad beam conditions (Figure 4). Under such conditions a considerable amount of scattering occurs in the attenuating medium surrounding or overlying the radioactive source in the patient. Harris *et al.* (85) have reported the variation in linear attenuation coefficient values with energy window settings and source depth under broad beam conditions. The buildup factor is the factor by which transmission is increased in the broad beam conditions, relative to narrow beam conditions (53). The buildup factor, $B(d)$, is defined as:

$$B(d) = \left(R/R_0 \right) \cdot \exp(\mu d) \tag{19}$$

where R is the count rate measured for depth, d, in a phantom, R_o is the count rate measured in air at same source to collimator distance, μ is the narrow beam linear attenuation coefficient. The method is based on the use of anterior and posterior image count rates and a set of buildup factors. The buildup factors can be derived from a calibration study using physical phantoms (31, 32) or by Monte Carlo techniques (34, 40). Once the buildup factors are obtained, Equation 19 can be applied to anterior and posterior image count rates for correction. There are reports of successful applications of the buildup factor method for cardiac studies (33), activity quantification in patients with hepatic disorders (86), activity quantification in lungs (81) and for kidney activity uptake (87).

The significant difference with this approach from the others in this section is that the buildup factor removes the requirement in the exponential term for correction due to scatter contribution and replaces it by a simple multiplicative factor. Thus, the linear attenuation coefficient used is that of narrow beam conditions and is independent of source depth, window width and other parameters that influence linear attenuation coefficients under the broad beam conditions imposed by nuclear medicine. Wu and Siegel (31) showed that the method provides error of less than 5%. The use of the buildup factor obviates the need for an external source to measure patient transmission and enables depth measurement to be obtained without the use of lateral views. This was the method adopted in this research to correct for scatter. In this case a buildup function was derived using Monte Carlo simulations.

Chapter 4

Theoretical Considerations of New Method and General Concepts of Monte Carlo Simulations

Despite the fact that several methods have been proposed to correct for errors in activity quantification, none has been adopted as the standard method for clinical use. In this chapter, the theory and general concepts of a new method that provides accurate activity quantification is developed and presented.

4.1 Theory

A planar image in nuclear medicine represents the projection of a 3D distribution of activity in the body onto a 2D imaging plane. In order to accurately correct for attenuation and scatter in planar imaging it is absolutely necessary that these phenomena be considered in the context of the 3D distribution of the activity. This is possible if we know the density distribution of the volume being imaged. The approach used here requires the creation of a set of density maps describing the volume, from which the planar image is obtained, so that appropriate attenuation correction factors can be calculated for each projection. These factors can be easily calculated from the set of density maps.

Consider a point source in a region of the body (Figure 14). If the uncorrected anterior and posterior emission images of this region are denoted by $M_a(i, j)$ and $M_p(i, j)$ respectively, then for each projection, the line sum of pixels along the ray of view, $\gamma(\theta, r)$, through the 3D structure will be the value of the pixels in $M_a(i, j)$ and $M_p(i, j)$ corresponding to this ray of view. For any projection at angle, θ, and for any ray, r, in the projection, attenuation in each pixel can be determined. Denoting the set of density maps that describe the density distribution for the transverse slices of this region by $\rho(i, j, k)$, where ρ is the density of the medium, attenuation corrected pixel counts for each planar image can be derived from the product of the uncorrected pixel count of the planar image and the line sum of the attenuation corrected pixel values along the ray of view, $\gamma(\theta, r)$. Thus, the attenuation corrected anterior emission image, $M_{ca}(i, j)$, can be expressed as:

$$M_{ca}(i,j) = M_a(i,j) e^{{}^{\mu}\!/_{\rho} \cdot \Delta s \cdot \left[\sum_k \rho(i,j,k)\right]_d} \tag{20}$$

and the corrected posterior emission image, $M_{cp}(i, j)$, can be expressed as:

$$M_{cp}(i,j) = M_p(i,j) e^{{}^{\mu}\!/_{\rho} \cdot \Delta s \cdot \left[\sum_k \rho(i,j,k)\right]_{t-d}} \tag{21}$$

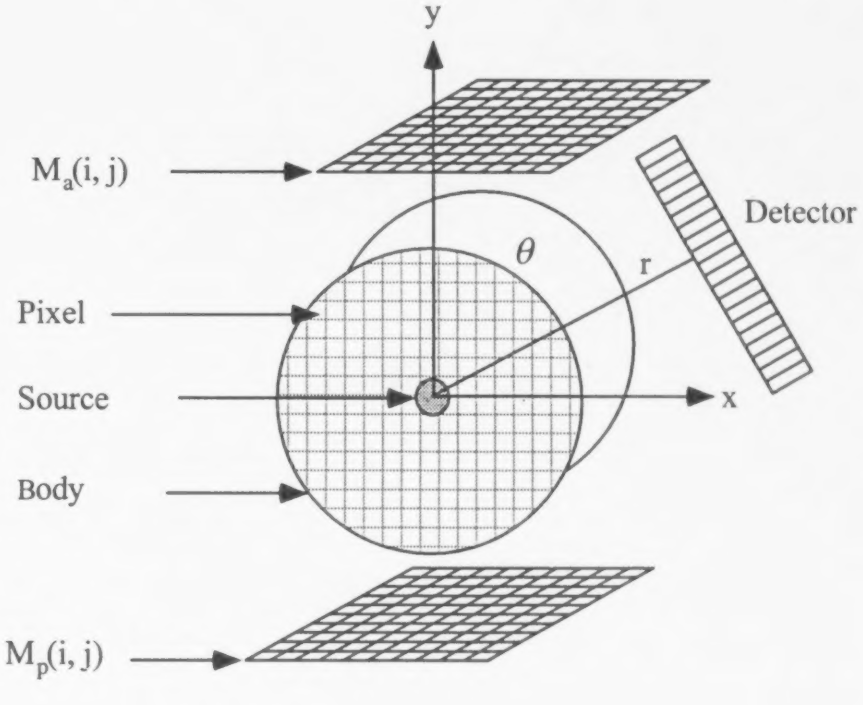

Figure 14. Transverse section of body containing a point source. Ma(i,j) and Mp(i, j) are the anterior and posterior uncorrected emission images respectively and r is an index for a ray at projection angle, θ.

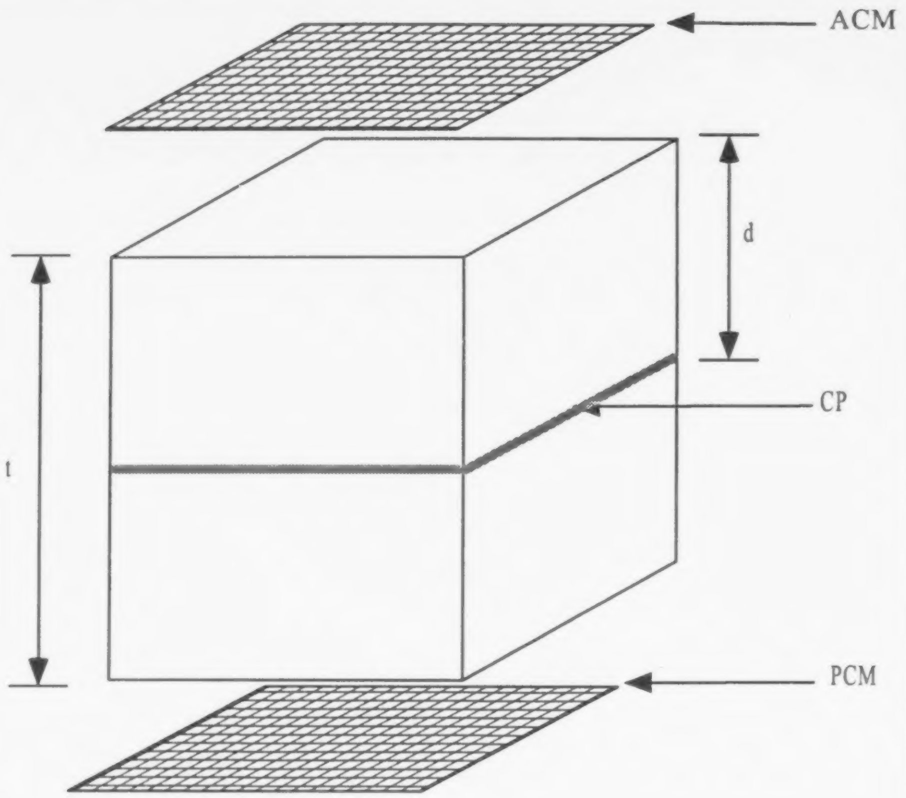

Figure 15. Volume of height, t, and coronal plane, CP, at depth, d. ACM and PCM are the anterior and posterior 2D correction maps respectively.

where Δs is the in-plane pixel size of the transverse slices, ${}^{\mu}\!/_{\rho}$ is the mass attenuation coefficient, d is the depth from the anterior surface to the coronal plane through the centre of the source and t is the thickness of the body (Figure 15).

The contribution of scatter to the projection data must be taken into account in the correction process. Following an approach developed by Ljungberg and Strand (34) and applied to SPECT imaging, a Monte Carlo simulation was performed using the Simind code (88) to determine the buildup of scatter. Monte Carlo techniques can be used to separate the primary events, Φ_p, and secondary events, Φ_s, so that the buildup function, $B(d)$, for source at depth, d, can be obtained from the expression:

$$B(d) = \frac{\Phi_p(d) + \Phi_s(i,j,k)}{\Phi_p(d)} \tag{22}$$

The buildup factor is the same for all pixels in the imaging plane for a given depth and (i,j,k) relate to the scattering medium. The anterior emission image corrected for attenuation and the buildup of scatter is therefore given by the equation:

$$M_{ca}(i,j) = \frac{M_a(i,j)e^{{}^{\mu}\!/_{\rho}\cdot\Delta s\cdot\left[\sum_k \rho(i,j,k)\right]_d}}{B(d)} \tag{23}$$

and the posterior image is given by the equation:

$$M_{cp}(i,j)=\frac{M_p(i,j)e^{\mu/\rho\cdot\Delta s\cdot\left[\sum_k \rho(i,j,k)\right]_{t-d}}}{B(t-d)} \tag{24}$$

The foregoing equations are exact only for a point or a plane source. However, utilizing an important property of the geometric mean, whereby the geometric mean of opposing projections effectively collapses a distributed source onto a plane of activity in the central plane (53, 89), allows the theory to be extended to the case of a 3D distribution. Hence, using equations (20) and (21), it is reasonable to write the following approximate relationship:

$$\left(M_{ca}\cdot M_{cp}\right)^{1/2}=\left(M_a\cdot M_p\right)^{1/2}e^{\mu/\rho\cdot\Delta s\cdot\left[\sum_k \rho(i,j,k)\right]_{1/2}} \tag{25}$$

Thus, if the count rates of the anterior and posterior corrected images of equations (23) and (24) are given by M_A and M_P respectively, then the absolute activity, A, is given by:

$$A=\frac{(M_A\cdot M_P)^{1/2}}{E} \tag{26}$$

where E is the gamma camera detection sensitivity expressed in counts per unit activity per unit time.

4.2 Monte Carlo Technique

Monte Carlo technique is a computational procedure that involves the use of random numbers to simulate real physical situations. The technique is used to obtain detailed computer simulations of how ionizing radiation is transported through matter. When a photon traverses the body it interacts with the constituent atoms and nuclei. The photon gets scattered or absorbed, deposits energy and produces secondary particles in the medium (Section 2.1). These processes occur statistically in nature. Hence, it cannot be known exactly how far a given photon will travel in tissue before it interacts. By means of Monte Carlo technique, one can use random numbers to pick individual flight distances for a large number of simulated photons so as to produce the photon attenuation (distribution) that is observed in nature. By this process individual photon histories can be studied and details of each interaction recorded. To achieve this, it is necessary to obtain the relevant physical data that govern photon transport in tissue such as the photon cross sections for interactions with the principal elements that comprise tissue: hydrogen, oxygen, carbon and nitrogen, for a given photon energy. These are then folded into Monte Carlo algorithms in such a way that a sequence of random numbers will have the photons in computations doing statistically what they do in nature.

The validity of Monte Carlo simulations in nuclear medicine has been presented by several authors (19, 34, 38, 58, 90), and is appropriate for modelling a wide variety of physical situations. In particular, it is used for modelling nuclear medicine imaging (detector) systems, phantoms, the interaction processes, detector performance parameters and radionuclides with complex decay schemes. The power and sophistication of the Monte Carlo technique allows for detailed investigations that present experimental techniques are unable to provide and is by far the most successful method for the simulation of stochastic processes in a scattering medium (91). The accuracy of the technique is due primarily to the fact that the computational procedure very closely approximates real physical situations.

Monte Carlo techniques were used in this research work initially, to simulate responses from homogeneous and nonhomogeneous phantoms representing various body sections from neck to midthigh and to simulate activity distribution in different regions (organs) of the phantoms. Subsequently it was used to simulate the buildup of scatter in projection data. In the initial stage, the use of a theoretical model provided the advantage of being able to study the effects of absorption and scatter on activity quantification in a wide variety of clinical situations prior to the beginning of laboratory work. The information obtained using the theoretical model helped to provide guidance as to the physical models required for the investigations before actually building the phantom (Section 5.1), and also to determine the experimental setup required. Later the technique was used to simulate buildup factors in each image pixel for the scatter correction procedure mentioned in the previous section. The simulations of buildup factors and their applications are described in Chapters 5 and 6.

Brief Description of the Monte Carlo Code

The Monte Carlo code is based on sampling uniformly distributed random numbers to simulate photon histories and the different possible types of interactions. Radioactive decays are sampled within a defined source volume. The photons emitted from the decay are followed in the phantom (body). Interactions are simulated according to the relative interaction probability of each process for the constituent atoms of the medium. A random number determines whether the emitted photon is a primary photon or if the photon will be scattered in the phantom. For the primary case the photon penetrates the phantom without interaction and is followed in a direction towards the detector. For the case of a scattered photon a random number determines how many orders the photon will be scattered before escaping the phantom. An isotropic direction is then sampled as the photon is followed step by step towards the detector. The probability $P(d)$ of a photon traveling a distance, d, in the medium can be determined by the relationship:

$$p(d) = \frac{\int_0^d e^{-\mu x}\,dx}{\int_0^{d_{\max}} e^{-\mu x}\,dx} \tag{27}$$

where $d_{\max}$ is the distance from the source to the surface of the phantom (or thickness of the crystal). A random number is then used to determine the photon pathlength, d, within $d_{\max}$, thus giving

$$d = -\frac{1}{\mu}\cdot\ln\left[1 - RN\cdot\left[1 - e^{-\mu d_{\max}}\right]\right] \tag{28}$$

where RN is a random number substituted for $P(d)$ in Equation 27. Cross section data (92) for the interaction types are stored in reference tables and are fitted to the current photon energy by linear interpolation. The interaction type is selected by a random number according to the relative probability of each type of interaction. The interaction will be: 1) photoelectric absorption if $RN \cdot \mu < \tau$; 2) Compton scattering if $\tau \leq RN \cdot \mu < (\tau + \sigma_c)$; 3) Rayleigh scattering if $(\tau + \sigma_c) \leq RN \cdot \mu < (\tau + \sigma_c + \sigma_r)$. After escaping from the phantom, a sub-routine checks if the photon will pass the collimator. The simulation of the collimator is based on geometric calculations to check whether the photon will pass through one of the collimator holes. If the photon does, it is followed in the crystal until it is absorbed or escaped. The centroid of the energy imparted by the photon is calculated and used to determine the apparent position of the event. If the magnitude of the imparted energy is within a predefined energy window, then the photon history weight is added to an image matrix in a cell corresponding to the centroid of the imparted energy. This entire process is then repeated for as large a number of photons as is required to build up a statistically significant response. A more detailed description of the code can be found elsewhere (88).

Theoretical Models

Several models of homogeneous and nonhomogeneous phantoms were simulated to study the effects of scatter on the accuracy of activity quantification under various imaging conditions prior to the commencement of physical experiments. The simulation of various source-phantom configurations requires that the geometries of the source and phantom be defined at run-time. Either or both source and phantom can be rectangular, cylindrical or ellipsoidal. A point source can also be used. To simulate the homogeneous phantom, the appropriate cross section data (from reference tables) for the phantom material to be simulated were used. For the nonhomogeneous phantom, a set of integer matrices that described the density in a transverse region of the phantom were used. These were simulated in cases where the density distribution is restricted to regions of regular geometry in a phantom. However, for clinically realistic density distributions these are best obtained from computed tomography slices (Sections 5.1 and 6.1) and then incorporated into the Monte Carlo program. This is demonstrated in Chapter 6 where the technique is used to simulate the buildup of scatter in human tissues. In the modelling process, a point at the centre of the phantom defines the centre of the coordinate system and all source positions in the phantom were defined with respect to this point. Standard nuclear medicine imaging setups and gamma camera parameters were modelled for 140 keV photons.

Chapter 5

Experimental Validation of New Method using Physical Phantoms

5.1 Materials and Methods

Design and construction of the phantom

A phantom was designed and built that enabled source location and patient geometry to be easily varied and activity measured for the purpose of validating the new attenuation correction method proposed. The phantom is comprised of 400 small removable rectangular perspex blocks (tissue equivalent inserts), each with dimension 1 cm x 1 cm by 7 cm length. It has cross sectional dimensions of 20 cm x 20 cm and is 7 cm in length. Several sets of small blocks of identical dimensions to the perspex blocks were made using different attenuating materials such as aluminum to simulate bone and foam to simulate lungs. Some of these blocks have a hole (8 mm diameter and 5 cm length) in them and are capped. This allows for the insertion of radioactivity in a desired region of the phantom so that gamma camera emission images of that region can be obtained. The design of the phantom (Figure 16) allows it to be easily transformed from a homogeneous state to a variety of nonhomogeneous configurations that model the effects of nonhomogeneous media within the field of

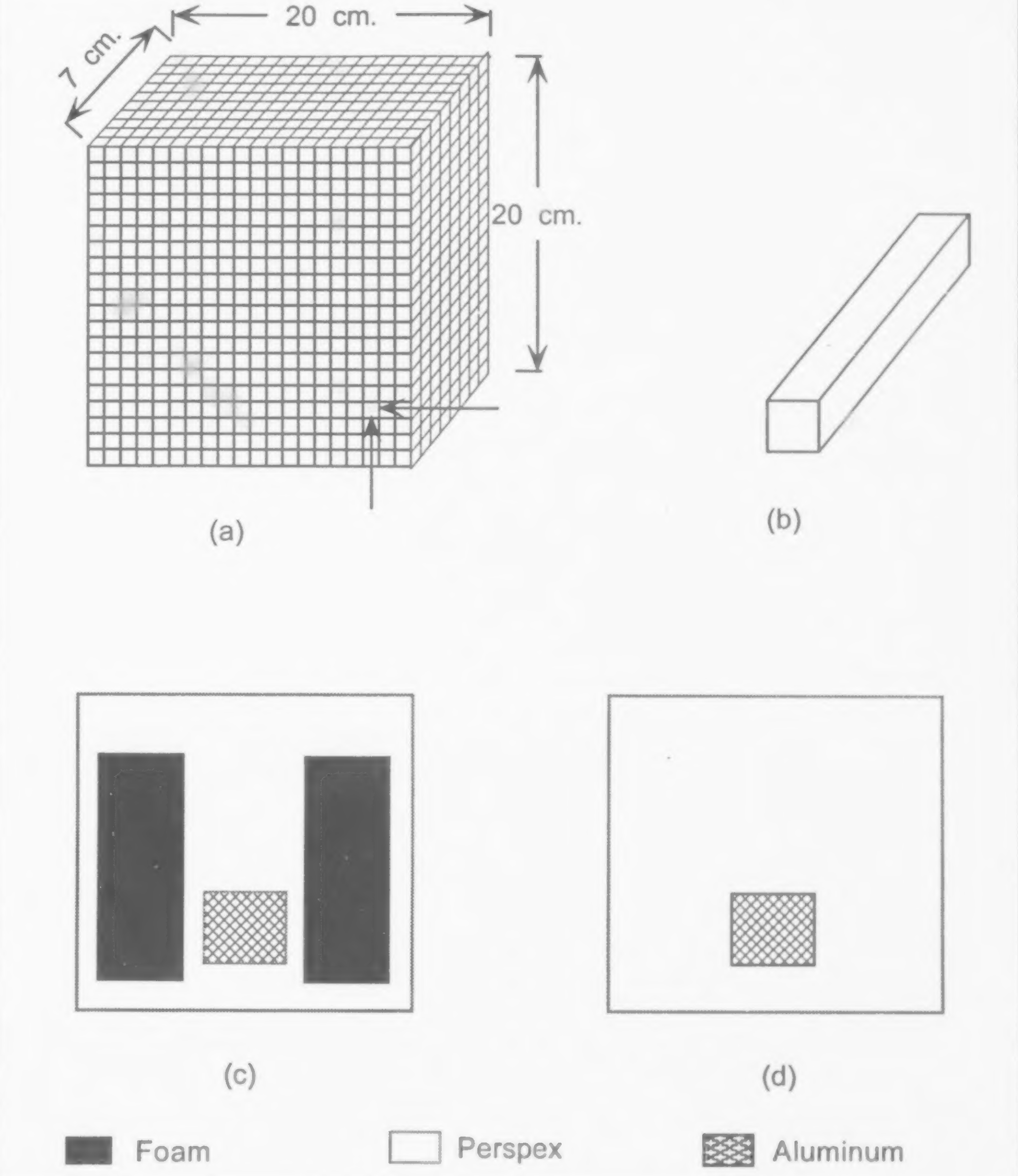

Figure 16. Design of phantom shown in (a). The arrows point to one of the small rectangular perspex blocks (b) of which the phantom is comprised. (c) is the cross section of the thoracic configuration consisting of 4 cm x 4 cm aluminum (spine) and two 14 cm x 7 cm foam inserts (lungs). (d) is the cross section of the abdominal configuration consisting of a 4 cm x 4 cm aluminum insert.

view (similar to that of the human thorax and abdomen). The size of organs and body cross sections can be varied as required, within the limits provided by the size and quantity of the inserts available.

Thoracic and Abdominal Phantom Configurations

To configure the thoracic and abdominal phantom, certain blocks were removed from the 20 cm x 20 cm perspex phantom and replaced with different tissue equivalent inserts that provide appropriate simulation of the desired body cross section. The configuration used for the thoracic phantom (Figure 16c) consists of: 1) a 4 cm x 4 cm aluminum block located in the lower region and along the central vertical axis of the phantom simulating backbone and 2) two 7 cm (width) x 14 cm (height) blocks of foam located laterally and symmetrical about the central vertical axis of the phantom, simulating lungs. For the abdominal phantom (Figure 16d), backbone was simulated as described above and all other structures in the abdomen were assumed to be adequately simulated by perspex. Complex abdominal arrangements were obtained by further replacement of perspex blocks with other tissue equivalent inserts in various regions of the abdominal phantom.

Computed tomography

CT scans of the homogeneous and various nonhomogeneous configurations of the phantom were obtained using a GE HiSpeed Advantage scanner. CT transverse slices of 5 mm thickness were acquired in a 512 x 512 matrix of 16 bit signed integer pixels.

The x-ray beam energy selected was 120 kVp. The images were transferred from the acquisition computer via network to a Sun Advantage Window Workstation and subsequently to floppy disks. A program was written in C to reduce the 512 x 512 matrix to 128 x 128 and to convert the Hounsfield numbers to density. This created a consecutive set of density maps from the CT slices. The matrix size reduction was done to make the data more manageable on a 486 PC. The conversion of CT numbers to density can introduce errors in the results depending on the accuracy of the assumptions made in such conversion. Several equations have been proposed (such as Fleming 1988) for relating CT number to density based on a number of assumptions. However, the approach taken in this paper was to write a program that directly assigns the CT numbers obtained to the actual density of each material in the relevant pixels. The densities of the materials were verified in our chemistry laboratory prior to this procedure and are presented in Table 1 (Tables are on pages 93 and 94).

Nuclear medicine imaging

Planar acquisitions of the phantom were obtained using a Picker 2000 (dual head) gamma camera system. Both detectors were fitted with low-energy, high-resolution, parallel hole collimators. A 20% symmetric energy window (E_{min}= 126 keV and E_{max}= 154 keV) was used to acquire projection data from ^{99m}Tc sources onto 64 x 64 matrices. Several experiments were performed in which planar images of line and volume sources were acquired for all homogeneous and nonhomogenoeus phantom configurations for which CT scans were obtained. Volume sources were comprised of several hollow tissue equivalent inserts that were filled with ^{99m}Tc. For the imaging procedures, the phantom was positioned centrally between the cameras, on the patient couch, and 5 cm from each collimator. The acquisition time for each image was 2 minutes. The activity of all sources used was measured at the beginning of each experiment using a calibrated well counter. Corrections were made for radioactive decay during the procedures.

Using the configurations depicted in Figure 17, two phantom studies were performed: the first with a 22.2 MBq line source at different locations along the central, vertical axes, and the second along a vertical line 5 cm off centre through the phantom. The locations of the line source are indicated in the figure by full circles and are 2 cm apart. A similar configuration was measured using two line sources in the central, vertical axis. The sources were initially separated by 2 cm at the centre of the phantom and were subsequently moved apart, symmetrically, by 2 cm increments towards each detector to a maximum separation of 12 cm. Images of the line source in air were obtained for reference purposes. For all images regions of interest (ROI) were defined for each source and count rates in each ROI determined. This was done for in-air, uncorrected, attenuation corrected and attenuation + buildup corrected images. The ROI in each image was defined 5 times to establish a value for the standard error of this measurement. The geometric means of opposing views of these images were then determined.

In addition, ^{99m}Tc transmission scans (Section 3.2) of the aforementioned phantom configurations were obtained. The emission sources were replaced by the appropriate tissue equivalent blocks and images of a ^{99m}Tc line source (22 cm length and 0.8 cm diameter), centrally positioned under the phantom and perpendicular to the patient couch, were acquired. The transmission scans were done to determine effective linear attenuation coefficients for use in the geometric mean method for the purpose of comparison with our new method. The effective linear attenuation coefficient was calculated using Equation 16.

Phantom studies were also performed using the source-detector configurations shown in Figures 18, 19 and 20. In Figure 18, a 22.2 MBq line source was placed in the locations indicated in a relatively complex nonhomogeneous phantom consisting of aluminum, perspex, water and foam. The foam and water had cross sectional dimensions of 3 cm x 3 cm each. Water was inserted in the phantom using hollow perspex inserts. Projection profiles for the uncorrected, attenuation corrected, and attenuation + buildup corrected images were obtained. This experiment was repeated with the line source replaced by a 2 cm x 2 cm volume source for the purpose of investigating the effects of a larger source on the projection profiles. The activity of all volume sources was 37 MBq. In Figure 19, two line sources, each with an activity of 18 MBq, were imaged along the central horizontal axis. One source was kept at the centre of the phantom and the other placed at 2, 4, 6 and 8 cm from the centre. In Figure 20, the 22.2 MBq line source was imaged at locations indicated at depths of 6, 10 and 14 cm below the anterior surface of the phantom. For each location indicated, calculations were done to quantify the source activity at (i) the true source depth and (ii) assumed source depths from 2 to 18 cm below the anterior surface of the phantom.

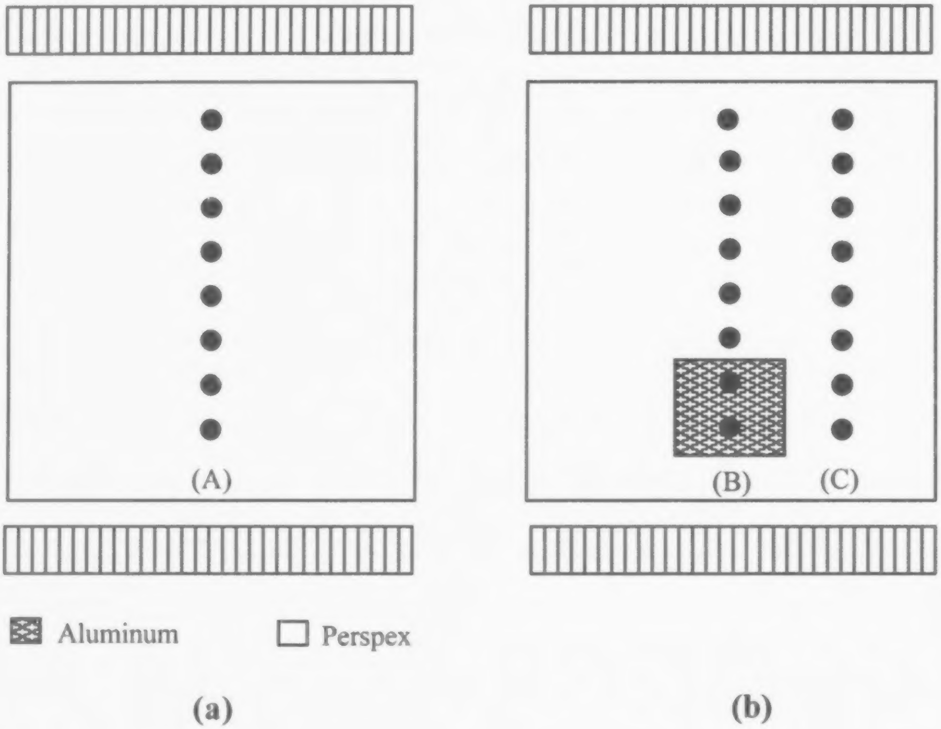

Figure 17.. (a) Transverse section of homogeneous perspex phantom with line source configuration (A). (b) Transverse section of nonhomogeneous phantom, which consists of perspex and a 4 cm x 4 cm aluminum block, with line source configurations (B) and (C). Each configuration was used under two conditions: (i) Only a single source present at any given time and (ii) Two sources present at any given time and were vertically separated. The gamma camera positions are shown above and below the phantom.

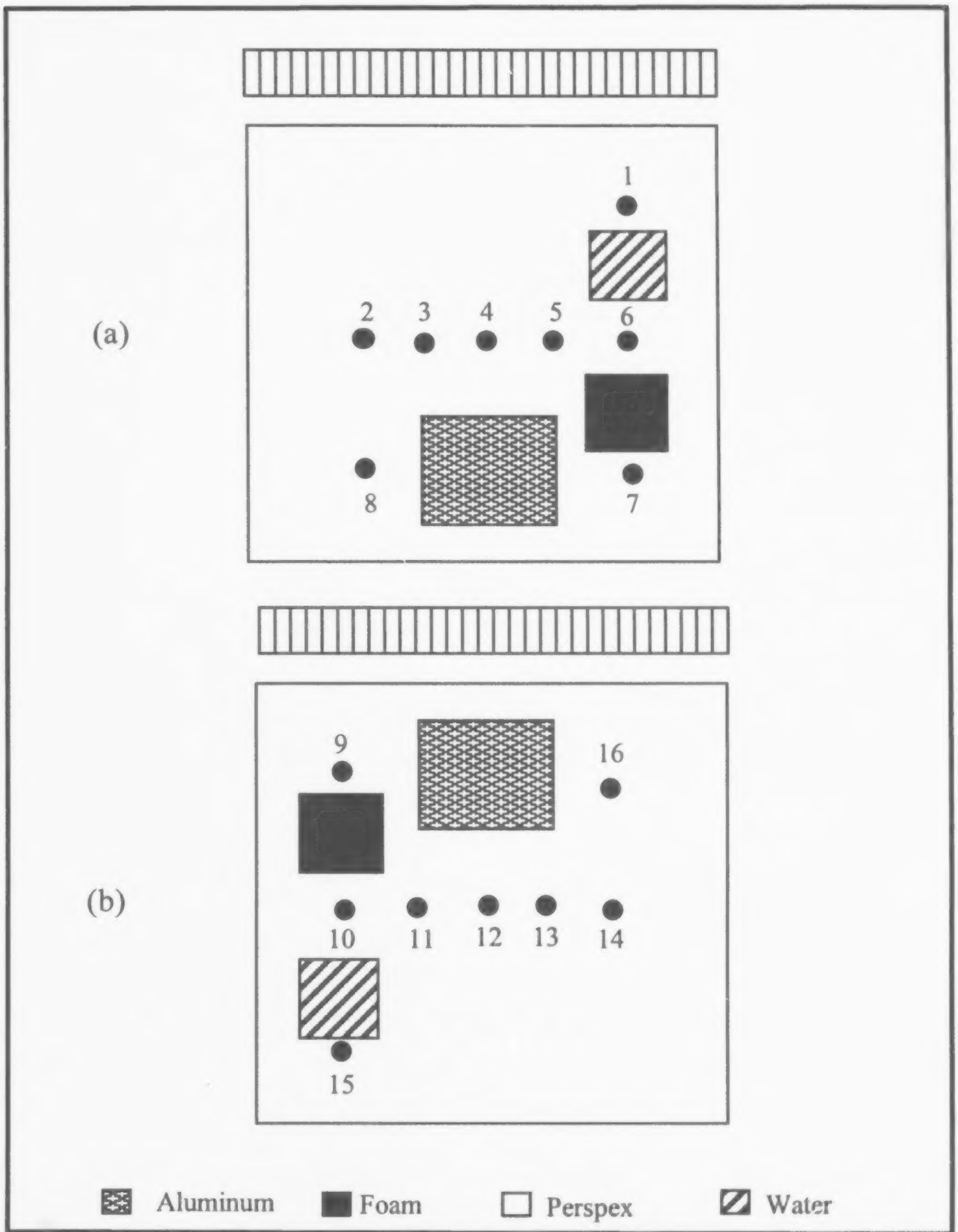

Figure 18. Transverse section of nonhomogeneous phantom with line source configuration (1 -16). The phantom consists of perspex, 4 cm x 4 cm aluminum, 3 cm x 3 cm water and 3 cm x 3 cm foam. Only one source was present at any given time. The gamma camera positions are shown at the top of each phantom arrangement.

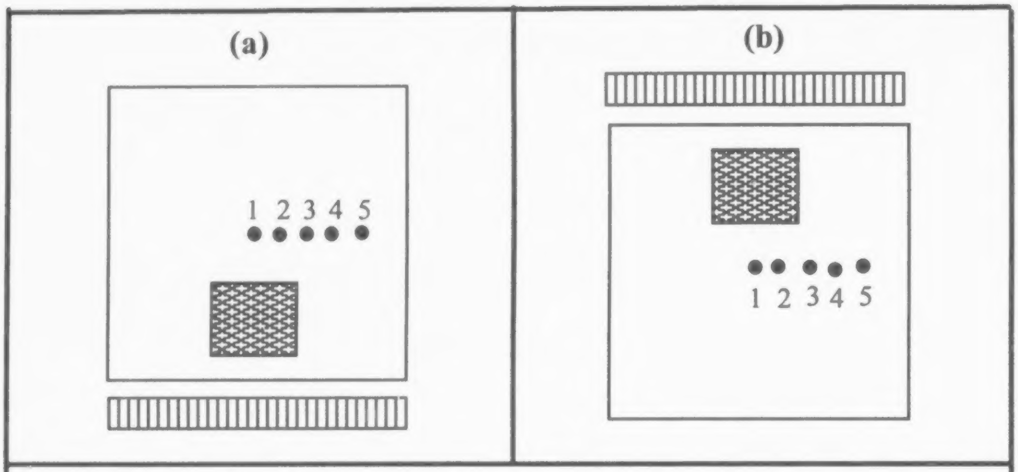

Figure 19. Transverse section of nonhomogeneous phantom horizontally separated sources. Two sources were present at any given time. Source 1 was kept in position while the second source moves to positions 2, 3, 4 and 5, each 2 cm apart.

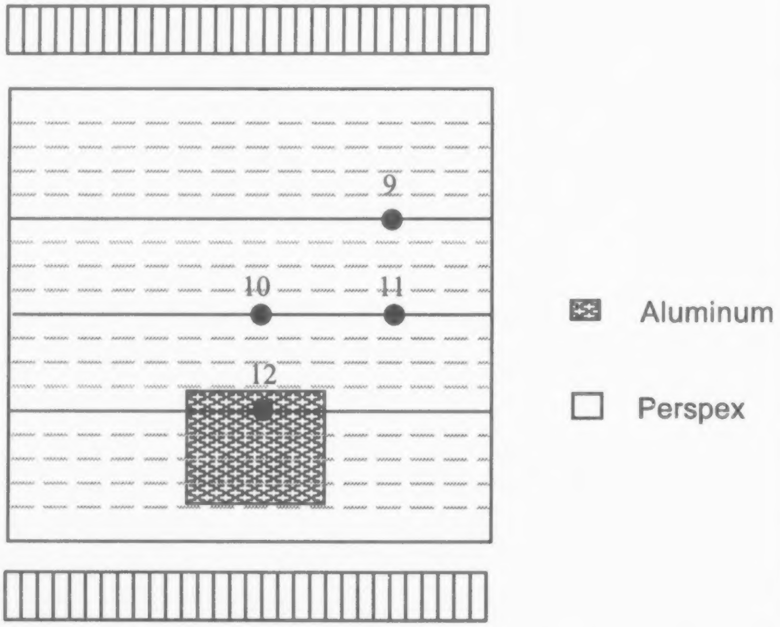

Figure 20. Transverse section of nonhomogeneous phantom with source positions (9 - 12). This configuration shows the actual depth of the source (solid line) and assumed depths (dashed line). Assumed depths varied by 1 cm step from 2 cm to 18 cm and only one source present at any given time. The gamma camera positions are shown above and below the phantom.

A thorough investigation of the scatter distribution at various depths in the perspex phantom was performed in order to study changes in the scatter content of the emission data with respect to source location in the phantom. To perform this investigation, a PC was interfaced with a multichannel analyzer (MCA) connected to the gamma camera. Energy signals from each camera were sent to the MCA. Energy spectra were recorded for a constant live time for a line source and for two horizontally separated point sources at various depths from 0 - 16 cm in the phantom. The point sources were initially separated by 2 cm at each depth in the phantom, then the process repeated for 6 cm and 10 cm separations. The PC communicated with the MCA via ProCom (a commercial communication software) and the spectral data recorded by the MCA for each source location were stored in the computer for subsequent processing.

Activity quantification was performed on several volume sources that were studied. For the abdominal phantom, a 2 cm x 2 cm source was inserted at the centre of the phantom and imaged. This was subsequently replaced by a 4 cm x 4 cm source for which images were also acquired. Further imaging of the abdominal phantom was performed with a 2 cm x 2 cm source placed at the centre of the spine. For the thorax phantom, images of activity in the lungs, spine and centre of the thorax were acquired. The lung sources were prepared from a 5 ml water solution containing 37 MBq of ^{99m}Tc. This was pulled up in a syringe and carefully injected into each lung so that the activity was reasonably distributed over the volume. For the spine, a 2 cm x 2 cm source was inserted for imaging. Note that only one volume source was present in the phantom at any given time.

For correct image scaling, the dimension of the acquisition pixels was determined. Images of two point sources placed at a known distance along the patient couch and 5 cm from each collimator were acquired. This procedure was repeated for the sources placed across the couch. The effective pixel size was calculated and used for precise alignment calculations.

Finally, in order to perform quantification the sensitivity (efficiency) of the gamma camera was determined. Five sources of activities 10.2, 18.7, 37.8, 73.9 and 103.6 MBq were used for the sensitivity experiments. To achieve this, a small beaker containing one of the sources was placed on the face and at the centre of one collimator and 30 cm from the other. Ten 1 minute counts were obtained for the source and the procedure repeated for the other sources. The sensitivity, E, was determined from the relationship:

$$E = \frac{C}{A \cdot t} \qquad (29)$$

where C is the average counts, A is the activity and t is the acquisition time.

Determination of 2D correction maps

The set of density maps obtained from CT images of the phantom provides a fairly accurate description of the density distribution on a pixel by pixel basis over the entire volume imaged. Determination of attenuation correction maps for planar imaging requires that the density information over this volume be accurately represented in 2D. In order to achieve this, an algorithm was developed that projects the 3D information provided by the set of consecutive density maps and creates opposing pairs of accurate 2D correction maps (Figure 2). The CT array that describes the volume consists of n 128 x 128 matrices, where n is the number of transverse slices required for the correction process. The source depth in the phantom was defined as the number of voxels from the surface of the phantom to the coronal plane through the centre of the distribution. In this case, the matrix size used was 64 x 64. The algorithm has a user interface that, among other things, allows the user to define the coronal depth of the activity distribution in the phantom and to select the desired matrix size of the projected anterior and posterior correction maps . The matrix size selected is the same as that used for the nuclear medicine acquisitions. Using the pixel and voxel dimensions, alignment parameters between the volume and the projected 2D arrays were calculated. Alignment parameters were defined in terms of the transverse voxel slice and sagittal voxel slice that correspond to specific rows and columns of the projected data. Subsequent to the data input, the program integrates along each ray of view over all voxels from the defined coronal plane to the anterior surface to form the anterior 2D correction map. It does the same for the posterior correction map. For any phantom configuration for which CT scans are obtained, the pair of 2D correction maps that are subsequently produced can be applied to nuclear medicine scans of that phantom configuration. Hence, only one set of CT scans is required for a given phantom configuration.

A separate program was used to convert the nuclear medicine data to a format consistent with that of the correction maps and to apply the correction maps to the uncorrected planar images as described in the theory section. An IBM RS/6000 model 570 computer was used to run the programs. The attenuation corrected images obtained were subsequently transferred to a 486 PC where all the data analyses were performed. A summary of the main steps involved in the correction algorithm is given next.

Summary of correction algorithm

Calculation of 2D correction maps from 3D (CT) data

1. Enter user parameters.
2. Calculate ROI.
3. Calculate the number of slices needed.
4. From the coronal depth, calculate attenuation integrals (ant and post) for slice $A(i,j)$.
5. Repeat step 4 for Volume of Interest (VOI), $A(i,j,k)$.
6. Write attenuation integrals for $A(i,j,k)_d$ and $A(i,j,k)_{T-d}$ to correction map file.
7. Calculate final correction maps using step 6 data.

Apply correction to nuclear medicine images

8. Convert nuclear medicine data to appropriate format (i.e. as in correction maps from CT data).
9. Calculate alignment of nuclear medicine images and correction maps
10. Calculate the corrected nuclear medicine images.

Simulation of buildup function

Monte Carlo simulations of the phantom configuration described in Figure 16 were done to determine the buildup of scatter in the projection data. The code was executed on a 486 PC. A 5 cm ^{99m}Tc line source was simulated at various depths in the phantom shown in Figure 16(a). The line source was varied in depth from 2 to 18 cm by 2 cm steps along a centrally located, vertical line. The lung substitute used in this work, foam (density = 0.02 g/cm^3), has density significantly lower than perspex (density = 1.19 g/cm^3). Consequently, separate buildup factors were simulated for the lung inserts (Figure 16(c)). There was no significant difference in buildup for the source at various depths in the foam, hence a single factor for the line source at the centre of the lung substitute was used. Events from the line source were simulated to interact with a NaI detector. The simulated detector incorporated a low-energy, high-resolution collimator and an energy window setting of 20% centered on the photopeak of the simulated ^{99m}Tc source. The simulated phantom-detector system setup and parameters closely modelled the situation described earlier for nuclear medicine imaging. The events detected in a pixel of the simulated image matrix of the line source were separated into a primary part, Φ_p, and a scattered part, Φ_s. The buildup function was then calculated using equation (3).

Additionally, buildup functions were simulated for energy window settings of 15%, 25% and 30%. This was done in order to investigate variations in the buildup of scatter with window width using the Monte Carlo code. The simulations were performed using the same gamma camera parameters and setup described earlier for the 20% window.

Summary of procedures for new method

Figure 24 provides an illustration of the stages involved in the current method and how the nuclear medicine and CT images are combined to produce corrected nuclear medicine images. Essentially, the phantom is first scanned by CT and nuclear medicine images of the phantom are subsequently obtained for various source-phantom configurations and activity distribution. The CT slices obtained are fed into algorithm

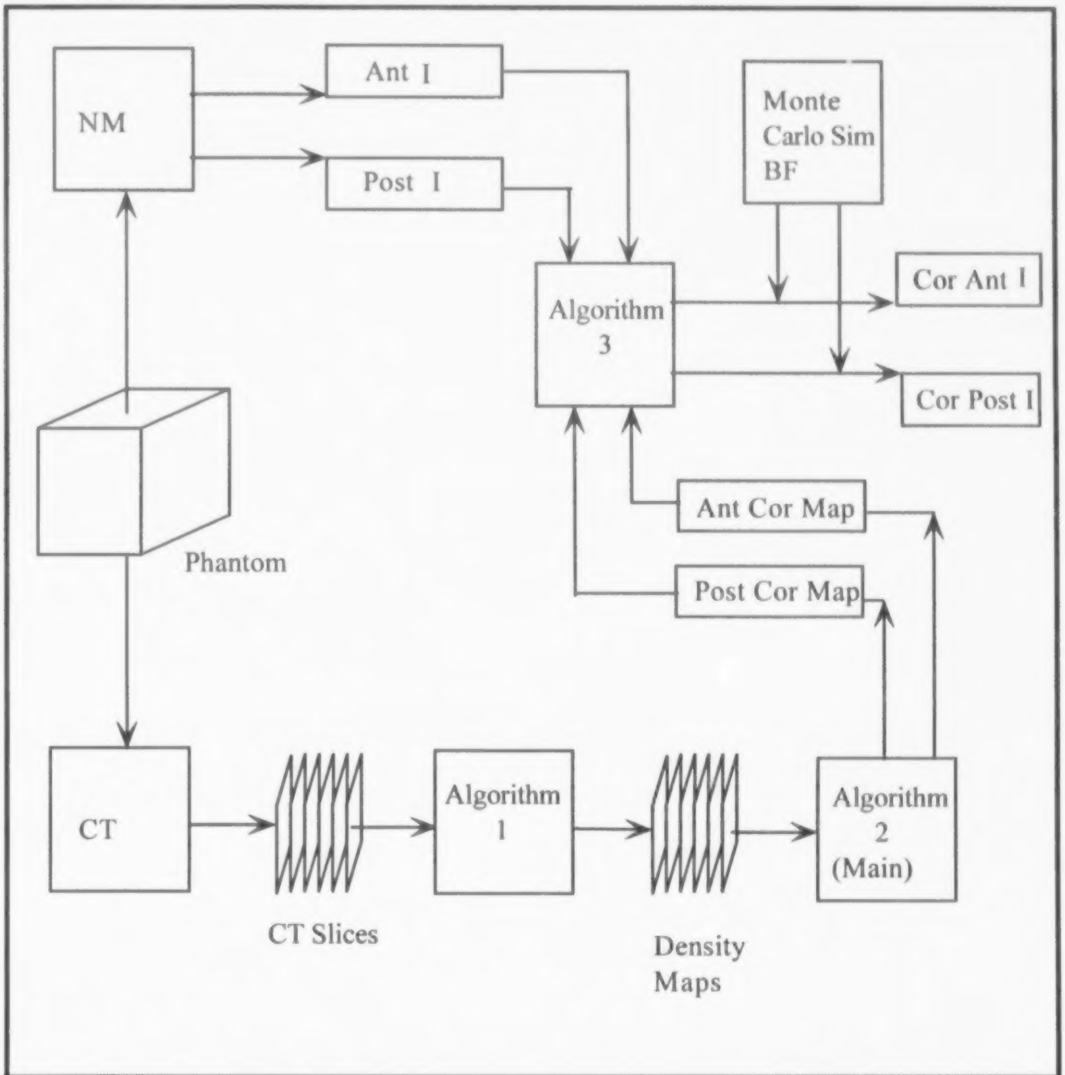

Figure 21. Flow diagram of the new method. NM = nuclear medicine, CT = computed tomography, Ant I = anterior nuclear medicine image, Post I = posterior nuclear medicine image, Cor Ant I = corrected anterior nuclear medicine image, Cor Post I = corrected posterior nuclear medicine image, Ant Cor Map = anterior correction map, Post Cor Map = posterior correction map.

1 where the image matrix is shrunk from 512 x 512 to 128 x 128 and the slices are converted to a set of consecutive density maps. Note that CT scanning is required to be done only once. The density maps obtained can be applied to subsequent nuclear medicine studies of similar phantom configuration or anatomical geometry. The output of algorithm 1 (i.e. the set of consecutive density maps) is fed into algorithm 2. This is the main algorithm and it is here that the attenuation integrals are calculated with respect to a defined coronal plane to produce a pair of 2D correction maps (anterior and posterior correction maps) and subsequently, inputs to algorithm 3. Nuclear medicine imaging of the phantom produces a pair of planar images (anterior and posterior) for which corrections are required. The pair of images are fed into algorithm 3 where the nuclear medicine data are converted to a format consistent with that of the 2D correction maps. In algorithm 3, the two pairs of image data are combined to produce a pair of attenuation corrected nuclear medicine images. Final correction is achieved by combining the output of algorithm 3 with Monte Carlo simulated buildup factors to correct for the buildup of scatter in the images, thus producing a pair of images with total correction.

5.2 Results and Discussion

Sensitivity

The sensitivity of the gamma camera used with a LEHR collimator was determined to be 83.6 counts MBq^{-1} sec^{-1} (3093 counts mCi^{-1} sec^{-1}). Figure 22 shows the results of the sensitivity experiments. Regression analysis was applied to the data from Table 2 using an equation of the form: $y = c_1x + c_0$. The coefficients obtained were $c_0 = -220.076$ and $c_1 = 93.625$. The coefficient of determination was 0.998. The results indicate that for the range of activity used, count rate varies linearly with activity. The sensitivity experiments served two purposes: 1) they provided the factor required to convert image counts to injected activity, thus essential for quantification and 2) they established the fact that there exists linearity between the range of activity used and the count rates obtained, thus indicating a consistent relationship between counts and activity.

Buildup Function Simulations

Figure 23 shows the graph obtained for the Monte Carlo simulated buildup factors. Multiple regression analysis was applied to the simulated data. A second order polynomial equation of the form: $a_0 + a_1d + a_2d^2$, where d is the source depth, was fitted to the simulated data for the homogeneous configuration of the phantom. The polynomial coefficients obtained were $a_0 = 0.99609$, $a_1 = 0.05952$, $a_2 = -0.00080$. The coefficient of determination of the simulated data was calculated to be 0.99974, which implies almost complete accuracy in the buildup function. The function indicates that the buildup of scatter in the projection data increases with source depth. Note that the function continues to change even at a depth of 20 cm (average patient thickness). This is why the use of an empirically derived, constant linear attenuation coefficient that assumes constant scatter contribution at all depths, cannot properly account for scatter and will produce inaccurate results.

The changes in buildup with energy window settings were also investigated. Energy windows of 15%, 25% and 30% were modelled and the results are presented in Table 3. The results indicate that the buildup of scatter increases with energy window width. This is not surprising because a large window accepts a greater proportion of Compton scattered photons and thereby provides for increased buildup. The values in Table 3 show a consistent trend of increased buildup with source depth for each energy window.

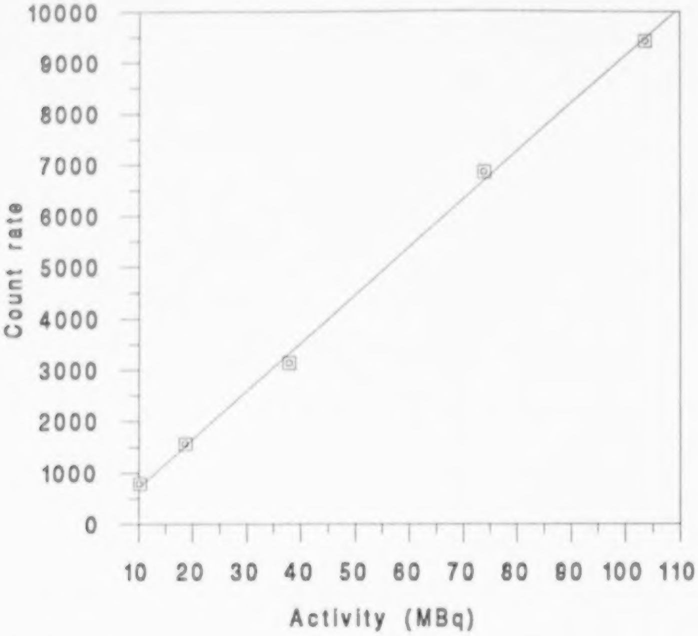

Figure 22. Results of sensitivity experiments

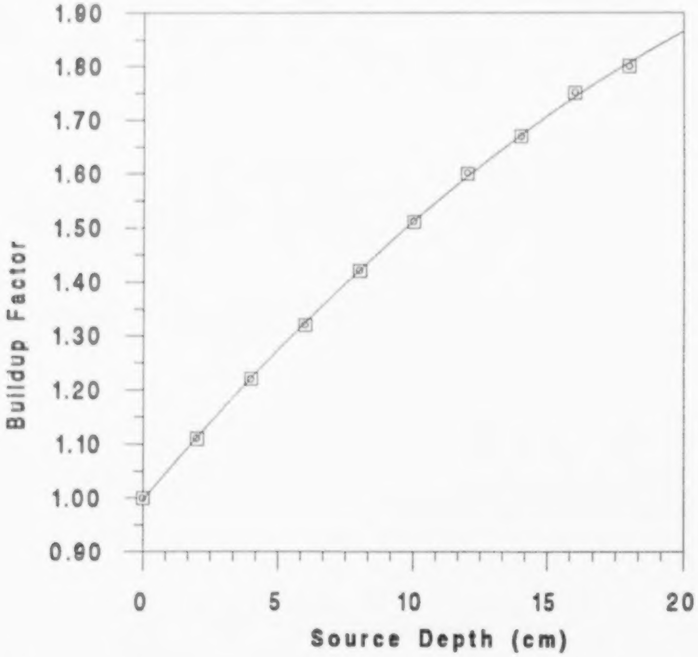

Figure 23. Monte Carlo simulated buildup function for ^{99m}Tc line source in perspex phantom using a 20% energy window.

Comparison of methods

Initial measurements performed on the homogeneous and nonhomogeneous phantom configurations in Figure 17 were assessed using two methods. The first is the geometric mean approach to planar imaging and the second is our new method that is proposed in this thesis. The results are presented in Figures 24 and 25. The effective attenuation coefficients determined for the geometric mean method from the transmission studies of the homogeneous and nonhomogeneous configurations were 0.155 cm^{-1} and 0.167 cm^{-1} respectively. The average activity value obtained (Table 4) from the homogeneous configuration for the geometric mean method is not surprising because, in general, this method works well in such situations with an appropriately defined broad beam attenuation coefficient. However, it becomes very inaccurate for a nonhomogeneous medium of significantly different densities (Table 1). Therefore, despite the fact that an effective attenuation coefficient was determined for the nonhomogeneous phantom, when the source was located in the overlap region of aluminum and perspex the geometric mean method undercorrected significantly and when the source was located in the nonoverlap region the method overcorrected significantly. Thus, no single linear attenuation coefficient value can be used to represent a medium of varied attenuation coefficients with values that are significantly different from each other.

The activity values indicate that the new method gives accurate results that are relatively consistent for the three situations tested. This is so because the new method takes into consideration the density variation within the medium and appropriately corrects for the contribution of scatter in the projection data. Note that for the three situations described (Figure 17), the new method produced an insignificant variation in activity quantification ranging from 100.4% ± 1.1 to 101.3% ± 1.07 of the actual activity. The GM method for the same situations produced variations ranging from 82.6% ± 1.92 to 115.5% ± 1.03 of the actual activity. The errors were determined from standard deviation calculations of line source activities in Figure 17.

The results of experiments that used two vertically separated sources are shown in Figure 25. This situation was used to simulate a distributed source in the body with activity concentrations that are vertically separated such as activity in the sternum and spine. The mean separation between them was used as the effective depth. Both methods showed a common trend of increasing estimated activity with vertical separation. However, the error appears to be less significant with the new method and only becomes significant as the sources approach opposite surfaces of the phantom.

Evaluation of new method using projection profiles

Projection profiles for sixteen source-detector arrangements (Figure 18) are shown in Figures 26(a-h) and 27(a-h) for the line source and Figures 28(a-h) and 29(a-h) for the volume source. The average count rate obtained for the line source in air was used as the 100% reference value. The results are summarized in Table 5 and demonstrate the significance of taking into consideration the buildup factor when correcting for attenuation. For instance, the uncorrected image obtained at projection, $\theta = 0^{\circ}$, gave an average count rate of 28.9%, relative to the in-air count rate, and when attenuation correction was applied to the image, an average count rate of 152.9% was obtained.

However, when attenuation + buildup were applied to the uncorrected image, the average count rate was 100.8%.

The projection profile of Figure 26(a) for the uncorrected image of the line source at position 1 (Figure 18(a)) gave significantly higher count rate than the other sources because it is closest to the detector. However, when corrected for attenuation and buildup, the resulting count rate was not significantly different from corresponding count rates for sources at other locations. The projection profile of Figure 26(d) for the line source at location 4 (Figure 18(a)) is slightly broader than the others. This is probably due to an increase in backscatter in the projection from the aluminum block directly below this location in the phantom. Otherwise, the shapes of the projection profiles were not significantly different for the various source locations indicated.

The line source at location 7 (Figure 18(a)) was one of the farthest sources from the detector and the photons emitted by this source were attenuated by foam, water and perspex before reaching the detector. Nonetheless, the projection profiles (Figure 26(g) for this source gave average count rates and full width half-maximum values that were comparable to those for sources closer to the detector. This is not surprising if we ignore the attenuation by foam and consider the fact that water with mean free path of 6.62 cm produces less attenuation than perspex of the same thickness, with mean free path of 5.98 cm for 140 keV photons. It seems, therefore, that there exists reasonable compensation for the increased depth of the source in this region of the phantom. However, the projection profiles of Figure 26(h) for the source at position 8 (same depth as position 7) had FWHM that were slightly greater than those of Figure 26(g) and produced a lower count rate for the uncorrected image. This reduced count rate is due to greater attenuation of photons by perspex from the source at position 8 than that at position 7 and the increased FWHM is due to greater scatter contribution in the projection data.

Figure 27 shows the projection profiles for the same source configuration imaged from 180° (Figure 18(b)). In general, the results compared very well with those obtained for the conjugate view (Table 5). The projection profile (Figure 27(b)) for the uncorrected image of the line source at location 10 gave a significantly higher count rate than in the previous phantom-detector configuration. This is due to the reduced attenuation caused by foam replacing perspex between the source and the detector. Similarly, the projection profile (Figure 27(d)) for the uncorrected image of the source at location 12 gave a significantly lower count rate than in the previous phantom-detector configuration due to increased attenuation produced by the aluminum, with density greater than twice that of perspex (Table 1). The slightly broadened profile observed is probably due to an increase in forward scatter from the aluminum block in the direct path of the photons. The projection profiles obtained when the line source was replaced by a volume source are presented in Figures 28 and 29. These profiles were broader than those of the corresponding line source. This is due to the distribution of the source over a greater number of pixels, thus producing slightly broader profiles.

Otherwise the features of the projection profiles were as discussed for the line source at positions corresponding to the volume source.

The effects on activity quantification of the presence of two or more sources horizontally separated (Figure 19) were investigated and the results are presented in Figure 30 and 31. This was done to simulate distributed activity in the body with concentrations that are horizontally separated such as "hot spots" in opposite ribs or in different regions of the spine. The projection profiles indicate that for the source separation studied, accurate quantification was achieved in each case. The overlap of projection profiles in Figure 30(a) is due to the inability of the gamma camera system resolution to completely separate events from the two sources that were relatively close to each other. However, their centroids, being 2 cm apart, were adequately resolved and are indicated by the peaks.

Effects of incorrect source depth estimation

Figure 32 compares the results of quantifying the source activity at correct (known) and incorrect (assumed) depths in the phantom for the source configuration shown in Figure 20. This procedure was performed to investigate the dependence of the new method on the accurate determination of the coronal depth required for the algorithm. The results indicate that it is not necessary to know *a priori* the actual depth of the source to obtain accurate results. Except for assumed source depths close to the surface of the phantom, the estimated activity values obtained were invariant with depth and reasonably consistent with the reference value. This invariance of activity quantification with depth can be accounted for by a fundamental property of the geometric mean, as illustrated in Figure 33, using spectral analysis of the line source at various depths (1 to 16 cm) in the perspex phantom (see next section). The slight overcorrection observed for assumed source depths close to the surface of the phantom are most likely due to inaccuracies in the buildup function which changes relatively rapidly towards the surface of the phantom. Also, the function was derived for pixels in a perspex phantom. Hence, when the source was assumed to be located in the region of the aluminum block and close to the surface, the overcorrection increases because the scatter contribution is greater than the buildup function indicates.

Spectral analysis

Counts were integrated over four regions of the energy spectrum recorded by the MCA for each source depth in the perspex phantom. The regions used were (1) 126 - 154 keV (20% photopeak), (2) 140 - 154 keV (upper half of photopeak), (3) 90 - 126 keV and (4) 30 - 90 keV. The geometric mean of the counts in each spectrum in each energy interval was calculated and the values plotted against source depth (Figure 33). The results indicate that the geometric mean of opposite views for each energy region does not vary significantly with depth. In fact, for the 126 keV to 154 keV range the geometric mean is almost unchanged for all depths. Figures 34 - 37 illustrate the variation of scatter in each region of the spectrum with depth from a single detector for a line (Figure 34) and distributed (Figures 35 - 37) sources. The results indicate that the proportion of counts in the scatter regions increased with source depth and seem to plateau at depths greater than 15 cm. The counts in the energy region 90 - 126 keV and 30 - 90 keV increased rapidly, initially, then continued to increase gradually with increased source depth. For the 90 - 126 keV energy range, this is due to a greater contribution of small angle scatter at energies near the photopeak for sources relatively close to the surface of the phantom and for the 30 - 90 keV energy range, this is due to an increase in the number of multiple scattered photons with increased source depth in the phantom.

Quantification of volume sources

The results of quantification experiments using volume sources are summarized in Table 6. Volume sources of cross sectional dimensions 2 cm x 2 cm and 4 cm x 4 cm, made up from hollow tissue inserts (perspex) that were filled with ^{99m}Tc and placed at the centre of the abdominal configuration (Figure 16(d)), gave estimated activity of 99% and 102.1% respectively. Accurate results were also obtained for a 4 cm x 4 cm volume source used to simulate a kidney in the abdominal phantom. For the 2 cm x 2 cm source placed at the centre of the spine in the abdominal phantom, estimated activity of 106.9% was obtained. Estimated activity for lung inserts (Figure 16(c)) of cross section 14 cm x 7 cm was 101.2% and that for the 2 cm x 2 cm tissue insert placed at the centre of the spine (Figure 16(c)) was 106.5%. Activity distribution for the volume sources was assumed to be uniform although the wall thickness of each small rectangular hollow block (tissue insert) that made up the volume is 1.0 mm. This assumption had no significant influence on the accuracy of the results. In the worst case, errors of less than 7% were obtained and this was only for sources in the aluminum volume. The overcorrection of activity quantification indicated by the results for the aluminum volume source, although not very significant, is most likely due to inappropriate correction for the aluminum volume by the buildup function which was derived for a line source in a perspex phantom. Errors obtained for the volume sources (Table 6) consist of combined errors for ROI selection and statistical variation in image counts. These errors are discussed in the following section.

Error Analysis

The results obtained using this method, like any other, are subject to errors. Identification and analysis of such errors form an essential part of experimental work. Likely sources of errors in this research are: 1) random errors in the image counts; 2) calculation of the density maps from CT transverse slices; 3) inability of the investigator to correctly reproduce ROIs for the same source; 4) injected activity and 5) attenuation and scatter of photons in the patient couch.

Errors due to statistical fluctuation in the image can be obtained from $SD = \sqrt{N}$, where SD is the standard deviation and N is the number of counts. In the quantification experiments (Figure 17), image counts were typically over 20,000. Thus the largest percentage uncertainty, V, is:

$$V = \frac{\sqrt{20000}}{20000} x\,100 = 0.7\%.$$

Hence errors due to counting statistics in the experiments using the configurations of Figure 17, were less than 1%. Additional errors were introduced in the quantification experiments from uncertainty in the definition of the size of the ROI used to delineate the source in each image. The ROI errors were determined by calculating the standard deviation, of the ROI counts for a given image and the results expressed as a percentage of the mean. The standard deviation is given by:

$$SD = \sqrt{\frac{\sum (x_i - \bar{x})^2}{n-1}} \tag{30}$$

where x_i and $\bar{x}$ are the individual and average ROI counts respectively. The product of the images produced a combined error, V_c, which was determined by error propogation methods (53) and is given by, $V_c = \sqrt{\left(E_{Ran}^2 + E_{ROI}^2\right)}$, where E_{Ran} and E_{ROI} are the percentage errors due to counting statistics and ROIs respectively. V_c was determined to be 1.22%. The error introduced by attenuation and scatter in the patient couch is typically less than 1% and was ignored. Those experiments that were evaluated using projection profiles produced errors in the range: 0.6% to 1.4%. These errors were primarily due to counting statistics. There is no easy way to determine values for some errors such as those introduced in converting the CT slices to density maps. However, these errors can be minimized by selecting appropriate ranges of Hounsfield numbers that do not overlap and are relatively far apart.

Table 1: Density and linear attenuation coefficient values for phantom inserts

Material	Density (gcm^{-3})	Narrow-Beam μ (cm^{-1})	Broad-Beam μ (cm^{-1})
Aluminium	2.7	0.390	0.365
Foam	0.02	N/A	0.0038
Perspex	1.17	0.174	0.155
Water	1.0	0.15	0.12

Table 2: Results of sensitivity experiments

Source	1	2	3	4	5
Injected Activity (MBq)	10.2	18.7	37.8	73.9	103.6
ROI Counts (Ave)	840	1563	3138	6250	8907

Table 3: Monte Carlo simulated buildup factors at various depths and energy window settings

Depth (cm)	15% Window	20% Window	25% Window	30% Window
2	1.06	1.11	1.17	1.21
4	1.16	1.22	1.32	1.38
6	1.23	1.32	1.47	1.55
8	1.32	1.42	1.59	1.69
10	1.40	1.51	1.71	1.82
12	1.51	1.60	1.81	1.93
14	1.58	1.60	1.92	2.04
16	1.68	1.75	2.0	2.15
18	1.72	1.80	2.07	2.23

Table 4: Percentage of actual activity estimated in various source-phantom configurations. The values in the table represent the averages for the three situations indicated.

Method	% actual Activity H	% actual Activity N-SO	% actual Activity N-NO
Geometric Mean	101 ± 1.07	82.6 ± 1.92	115.5 ± 1.01
New Method	100.9 ± 1.13	101.3 ± 1.07	100.4 ± 1.10

Key: H = homogeneous phantom, N-SO = nonhomogeneous phantom with source in overlapped region, N-NO = nonhomogeneous phantom with source not in the overlapped region.

Table 5: Percentage actual counts obtained from conjugate projections. The values in the table represent the averages for the three categories indicated.

Projection (^{0})	% Actual Counts UNC	% Actual Counts CNB	% Actual Counts CWB
0	28.9	152.1	100.8
180	31.1	149.5	101

Key: UNC = uncorrected , CNB = attenuation corrected without buildup and CWB = attenuation corrected with buildup.

Table 6: Results of volume sources in abdominal and thoracic phantom

Phantom	Volume Source Cross Section (cm^2)	Location	% Activity Uptake
Abdominal	2 x 2	centre of abdomen	99 ± 1.09
Abdominal	4 x 4	centre of abdomen	102.1 ± 1.11
Abdominal	2 x 2	spine	106.9 ± 1.38
Abdominal	4 x 4	kidney	103.2 ± 1.21
Thoracic	2 x 2	spine	106.5 ±1.19
Thoracic	14 x 7	lung	101.2 ± 1.10

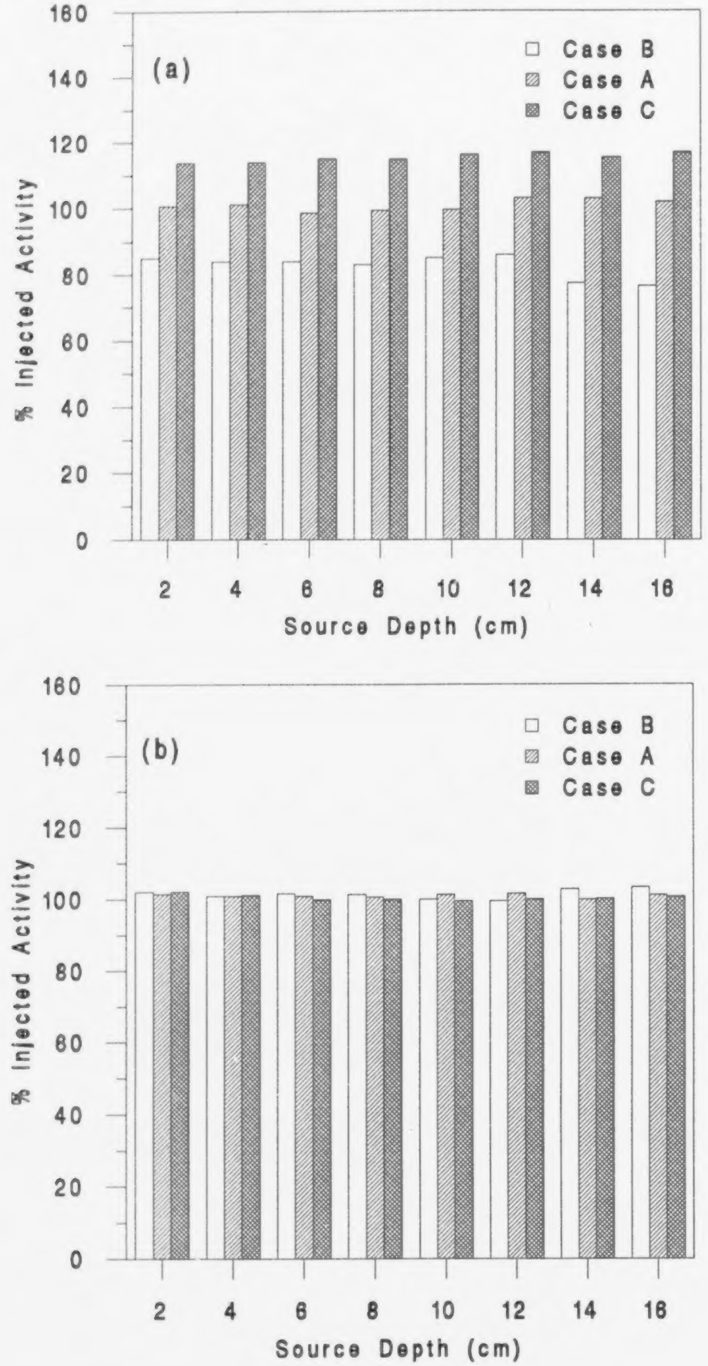

Figure 24. Results for the source configuration used in Figure 17 when only one source was present in the homogeneous phantom (A) and nonhomogeneous phantom for overlap region (B) and nonoverlap region (C). (a) Results obtained by the geometric mean method and (b) Results obtained by the new method.

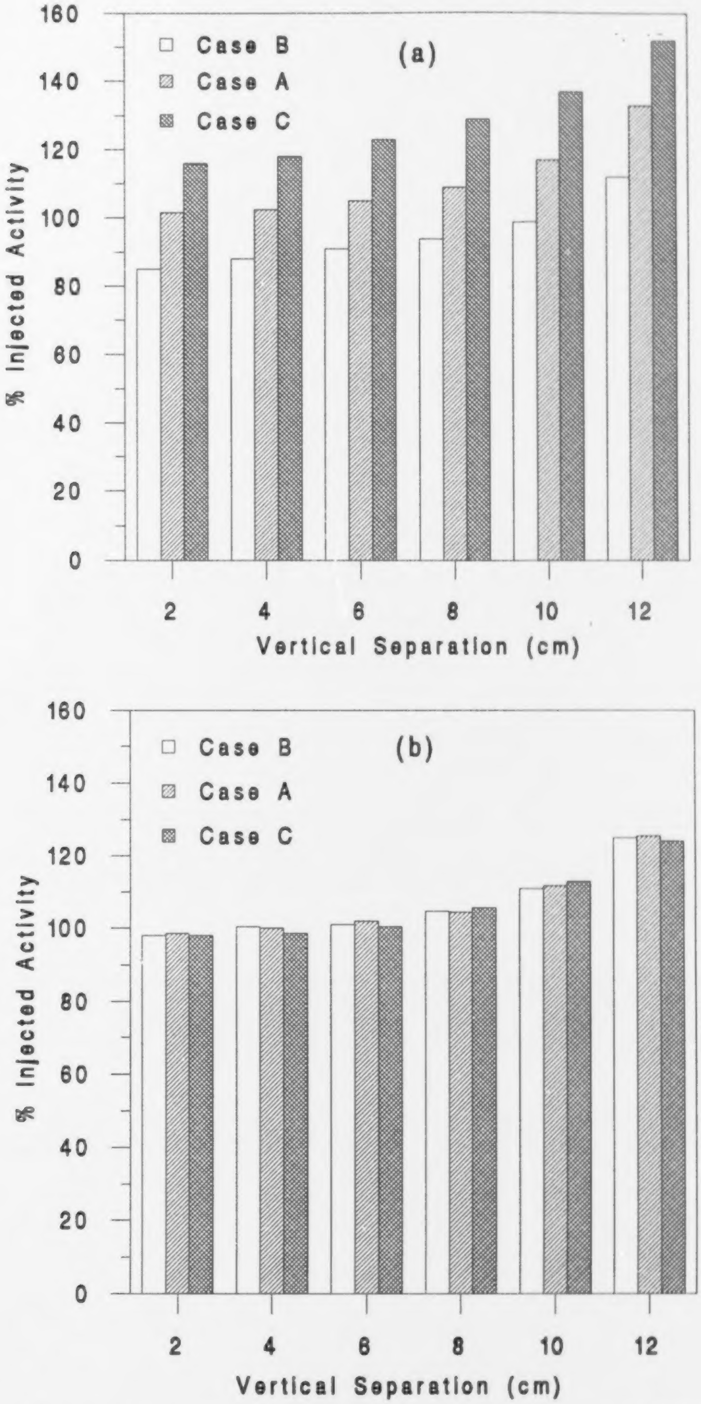

Figure 25. Results for source configuration used in Figure 17 when two source were present at any given time in the homogeneous phantom (A) and nonhomogeneous phantom for overlap region (B) and nonoverlap region (C). (a) Results obtained by the geometric mean method and (b) Results obtained by the new method.

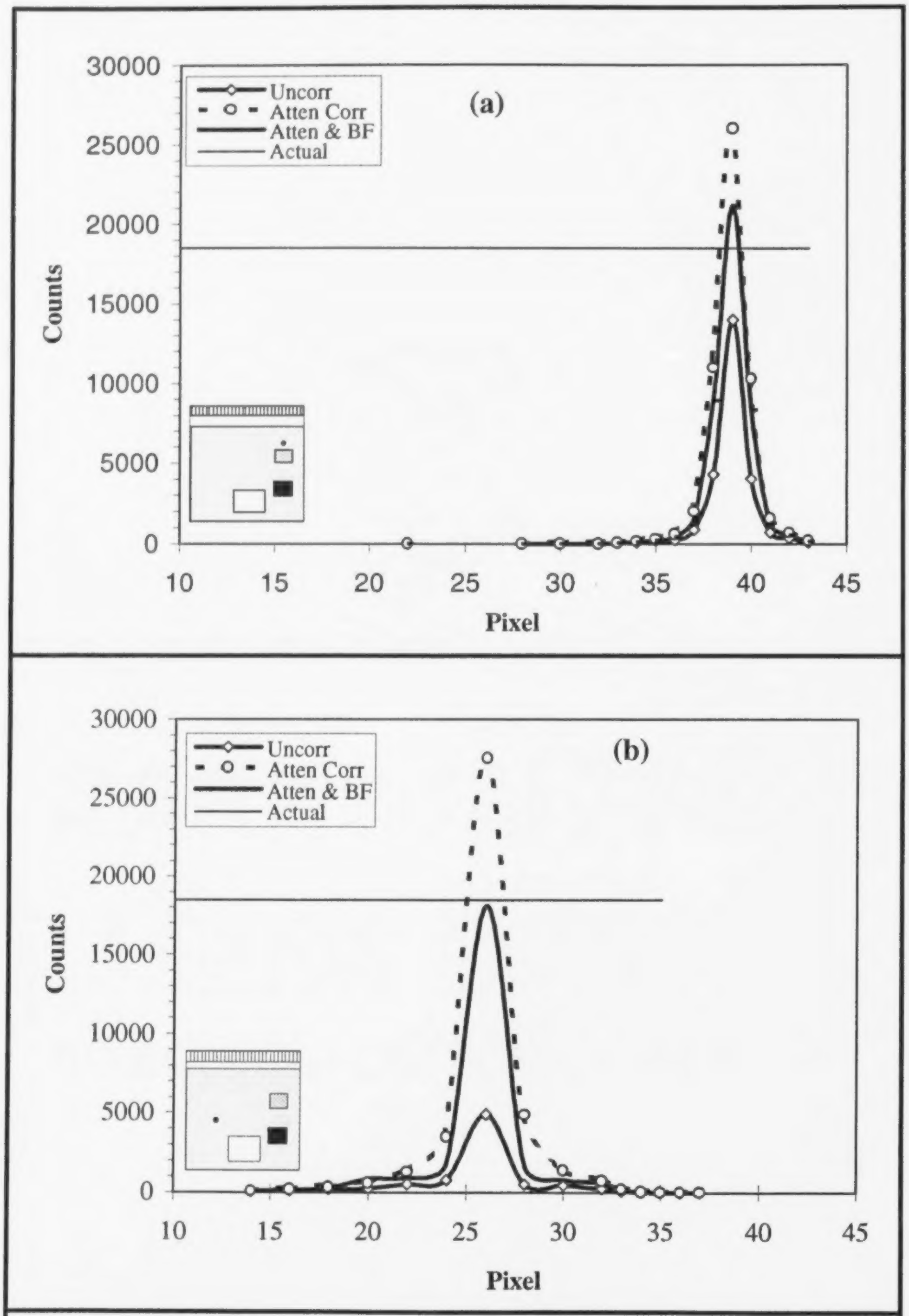

Figure 26. Projection profiles for source-detector configuration of Figure 18(a). Source positions are shown in lower left hand corner. a = 1; b = 2; c = 3; d = 4; e = 5; f = 6; g = 7 and h = 8.

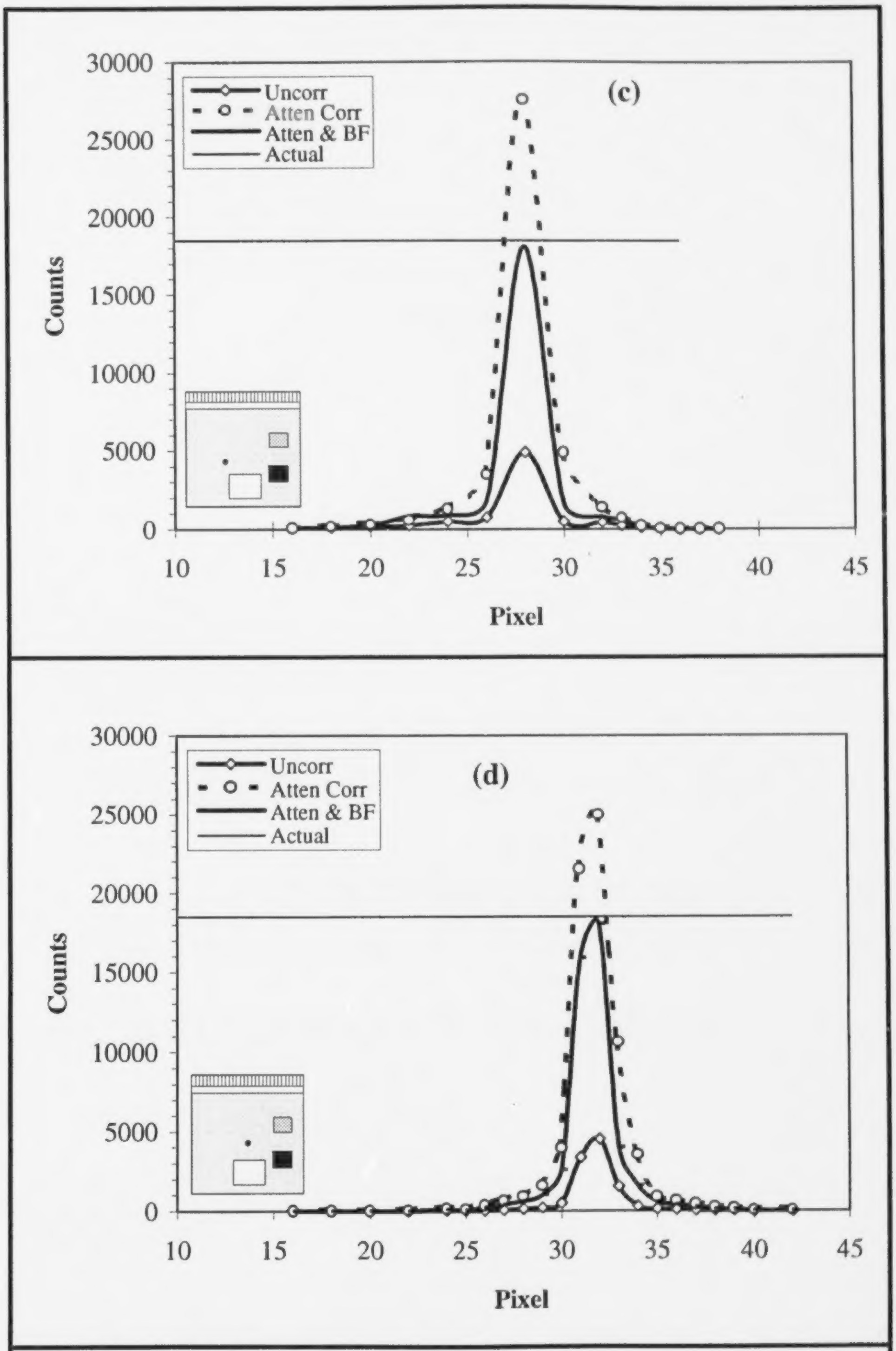

Figure 26 continued

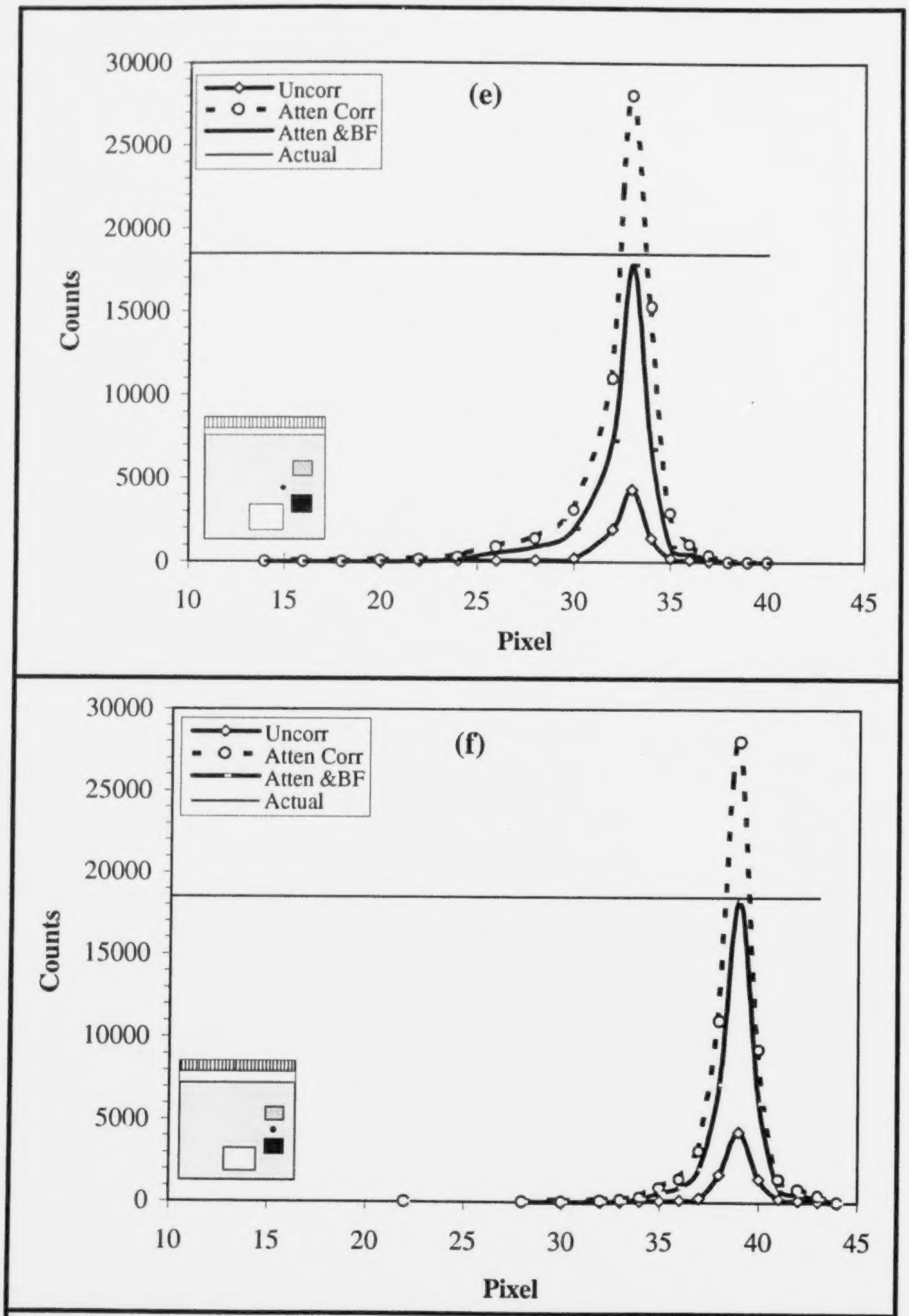

Figure 26 continued

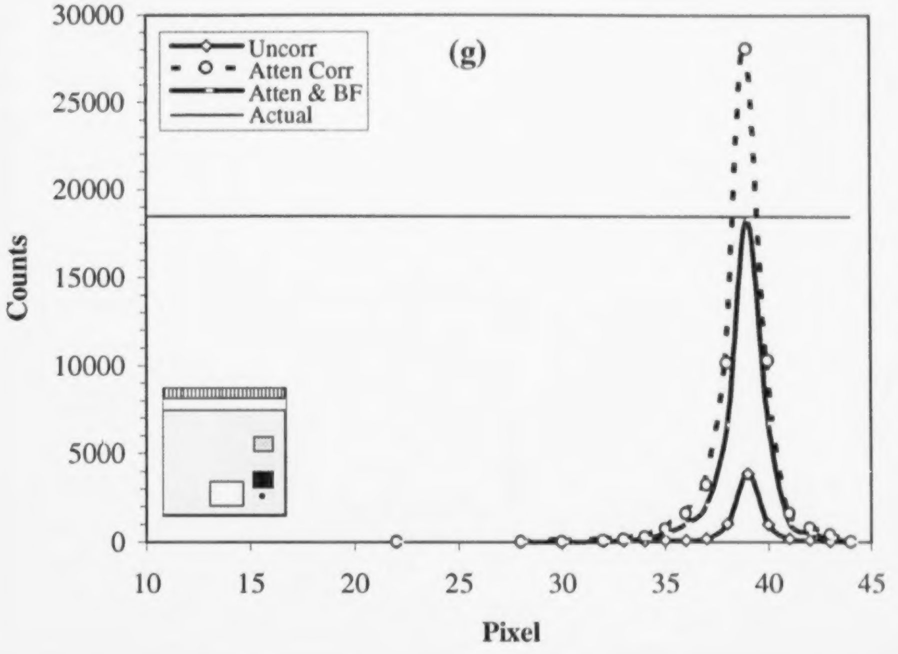

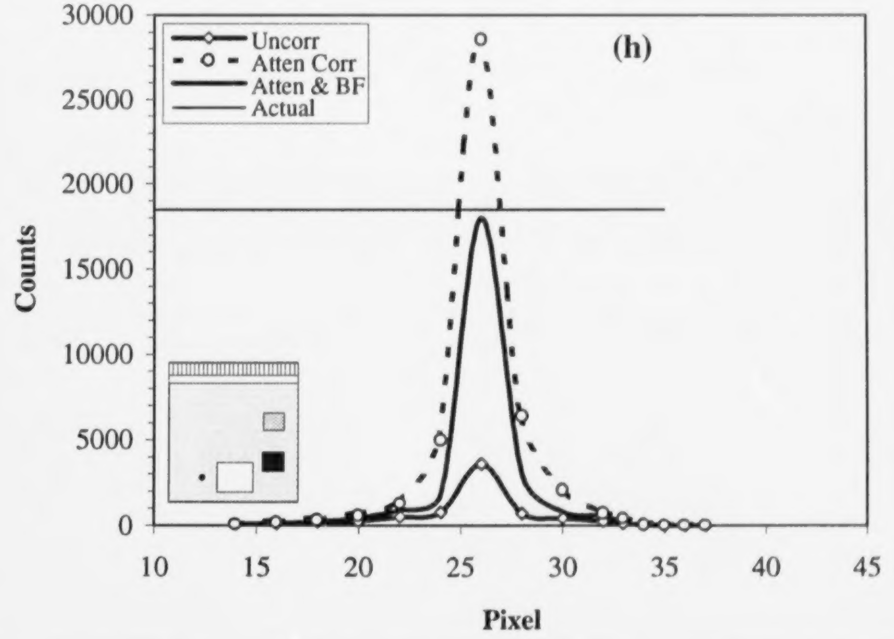

Figure 26 continued

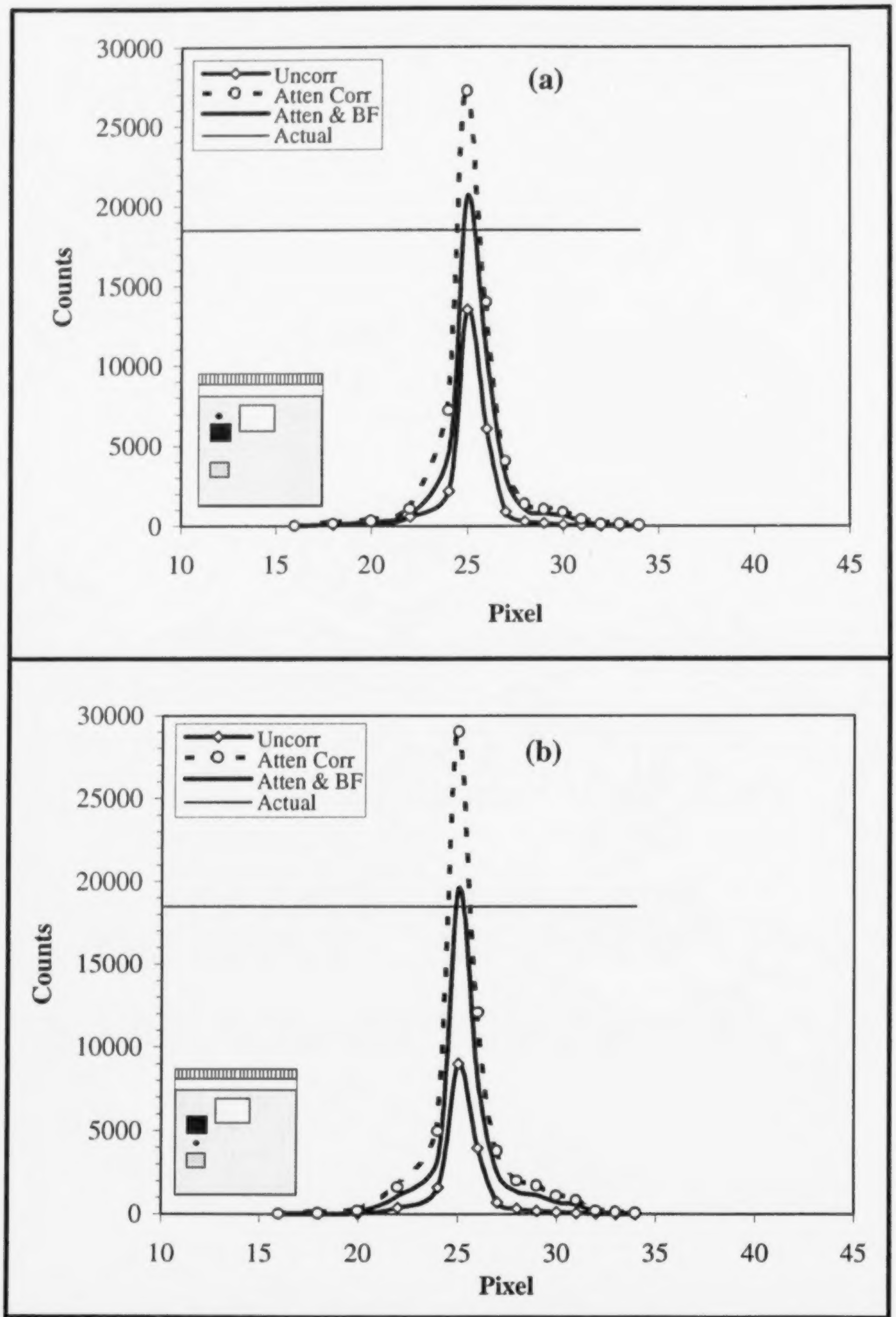

Figure 27. Projection profiles for source-detector configuration of Figure 18(b). Source positions are shown in lower left hand corner. a = 9; b = 10; c = 11; d = 12; e = 13; f = 14; g = 15 and h = 16.

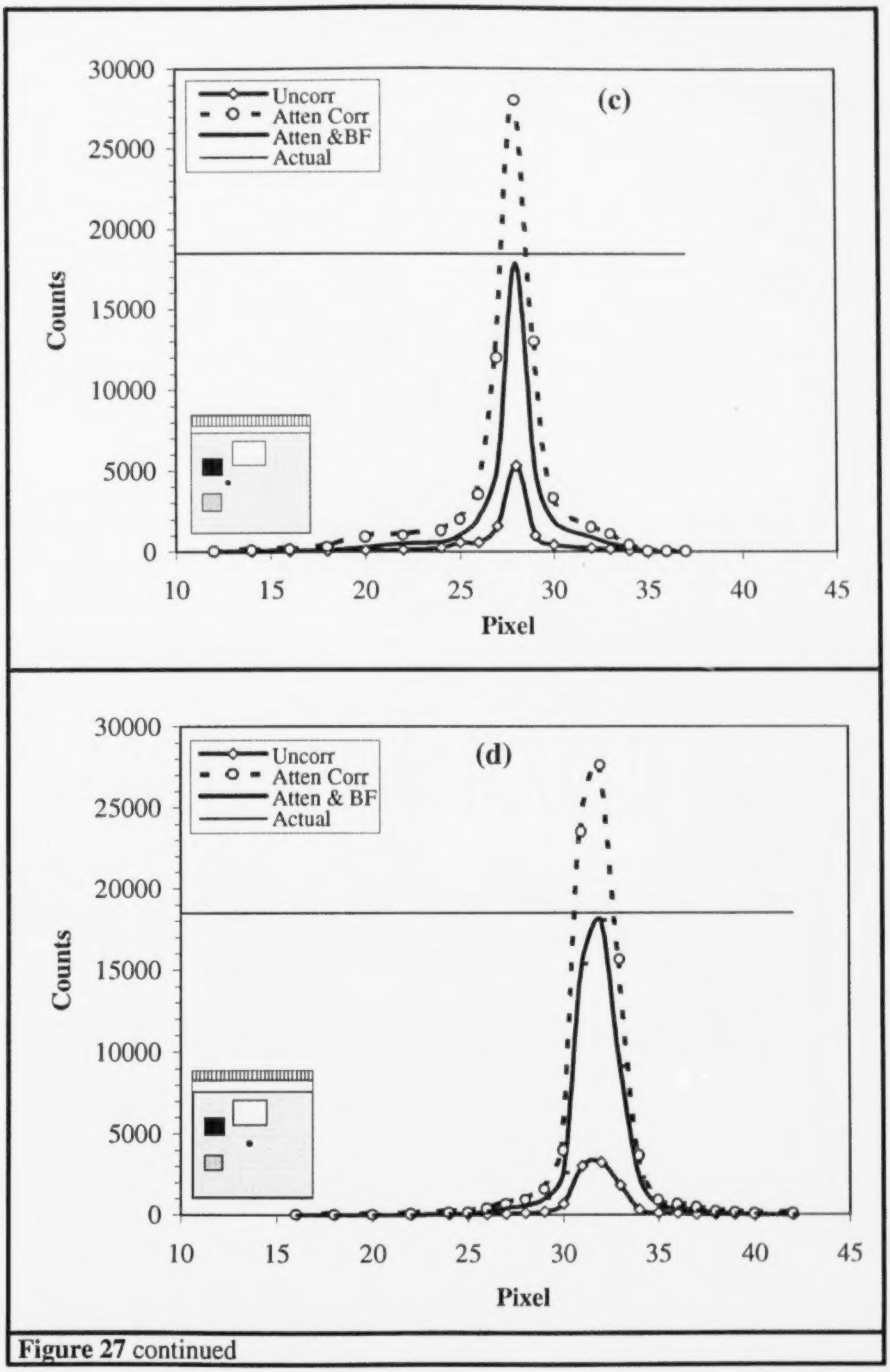

Figure 27 continued

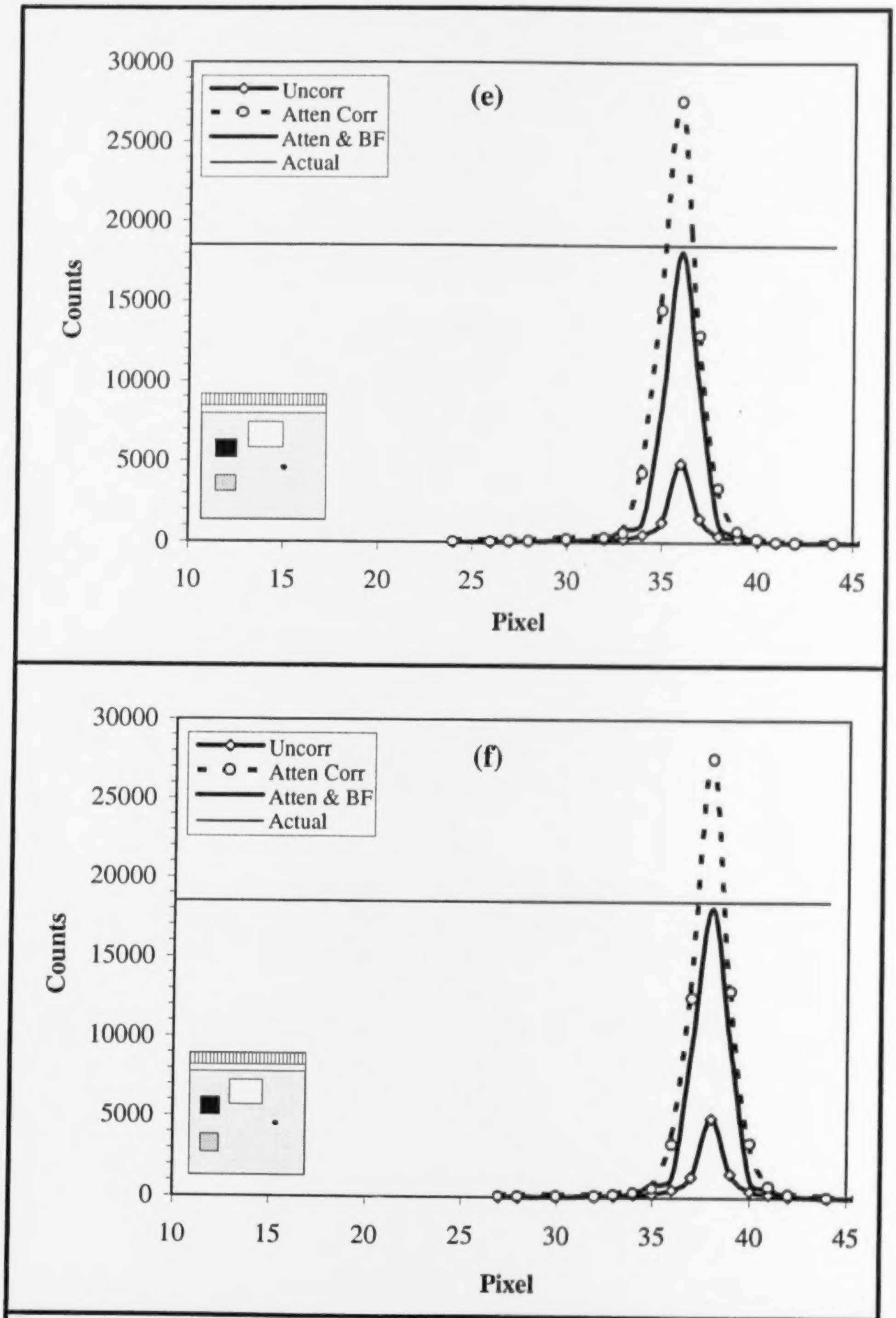

Figure 27 continued

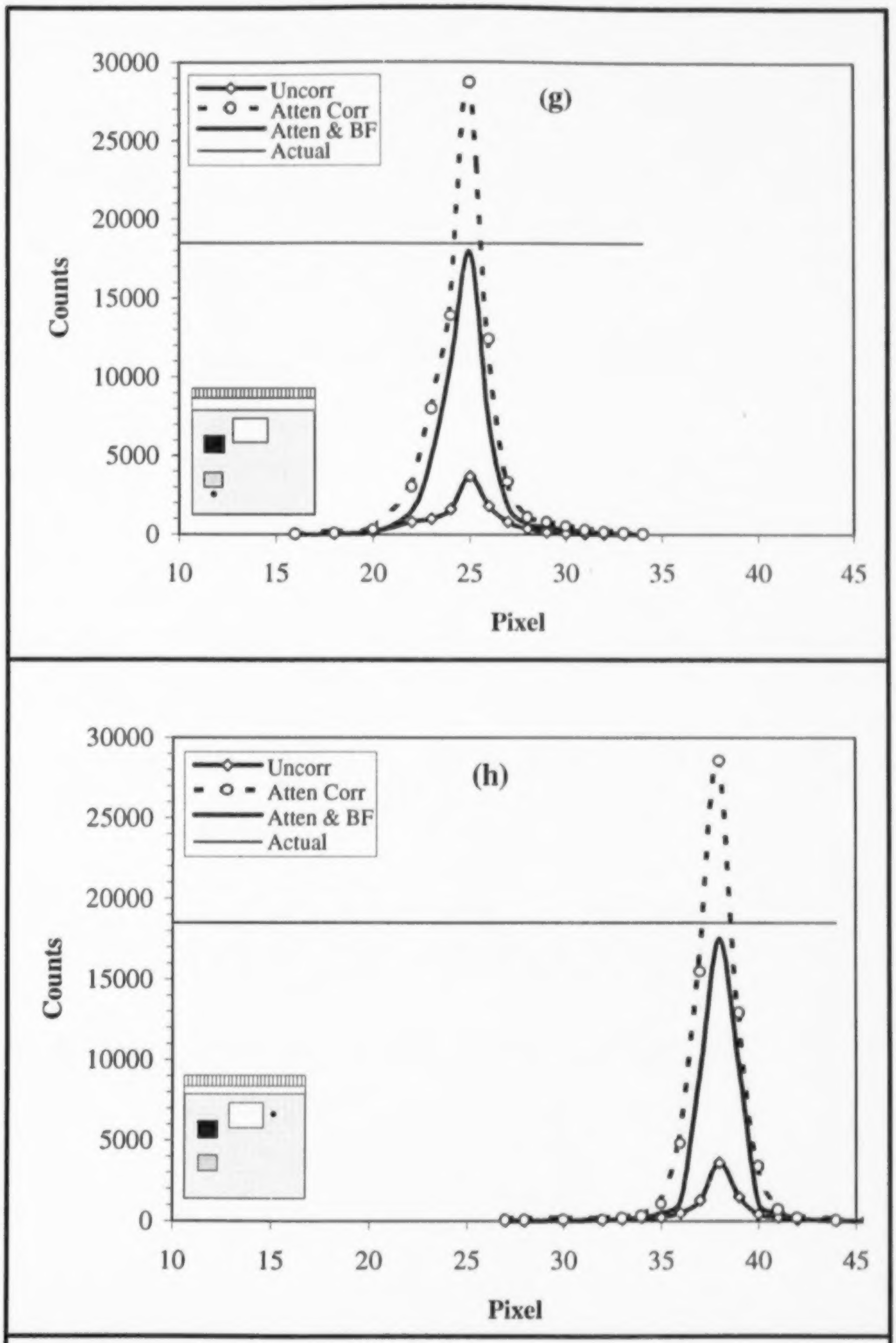

Figure 27continued

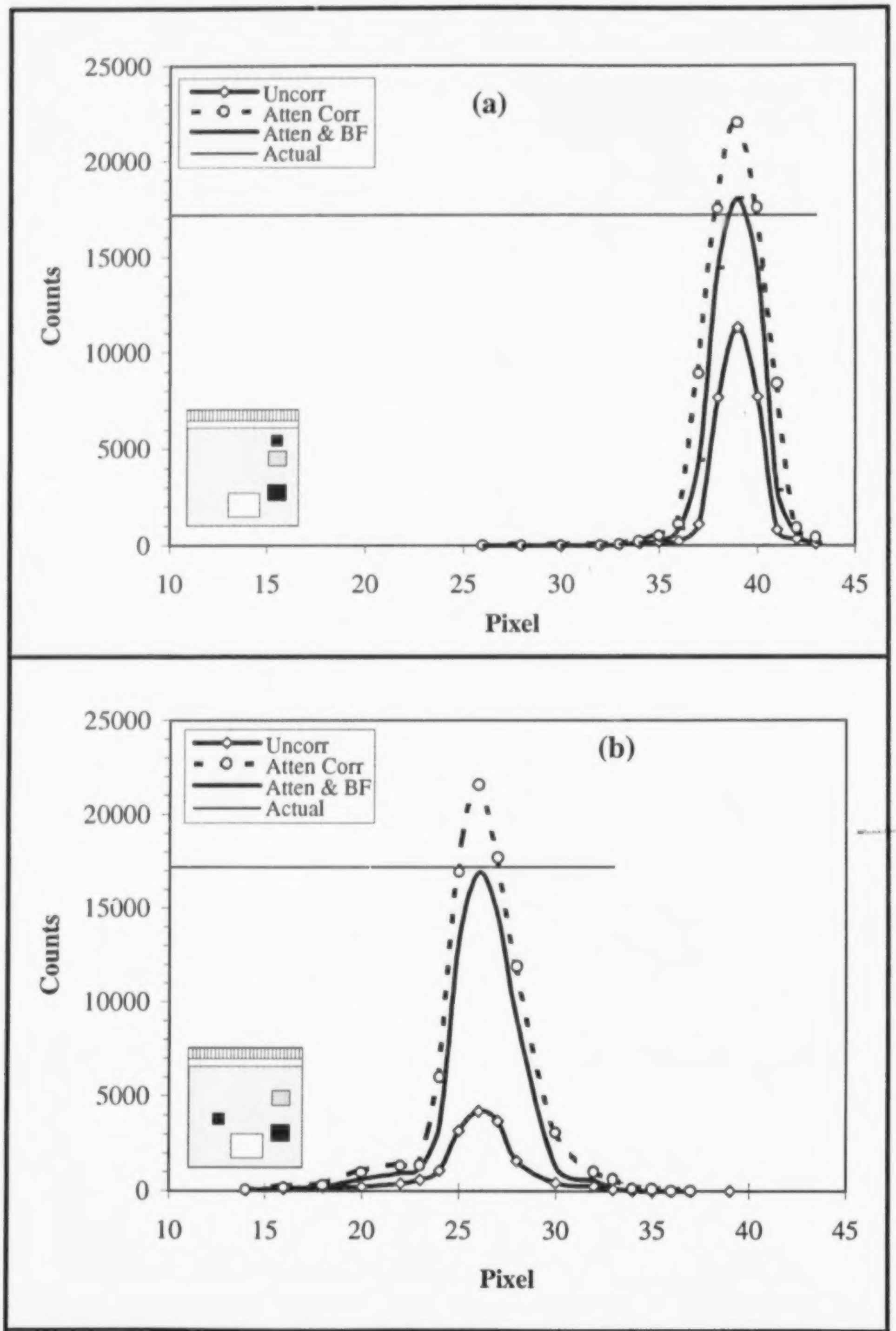

Figure 28. Projection profiles for source-detector configuration of Figure 18(a) using volume sources. Source positions are shown in lower left hand corner. a = 1; b = 2; c =3; d = 4; e = 5; f = 6; g = 7 and h = 8.

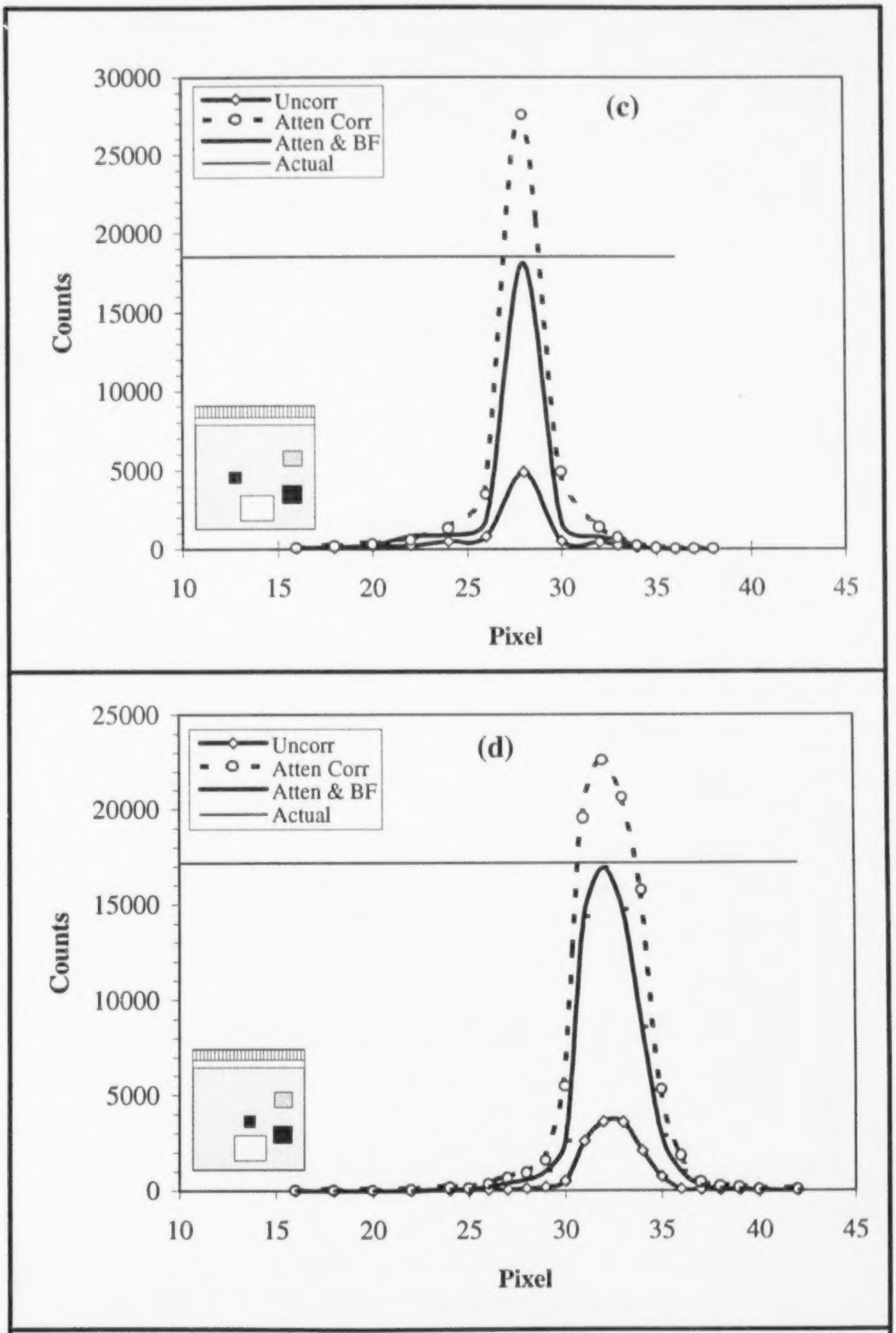

Figure 28 continued

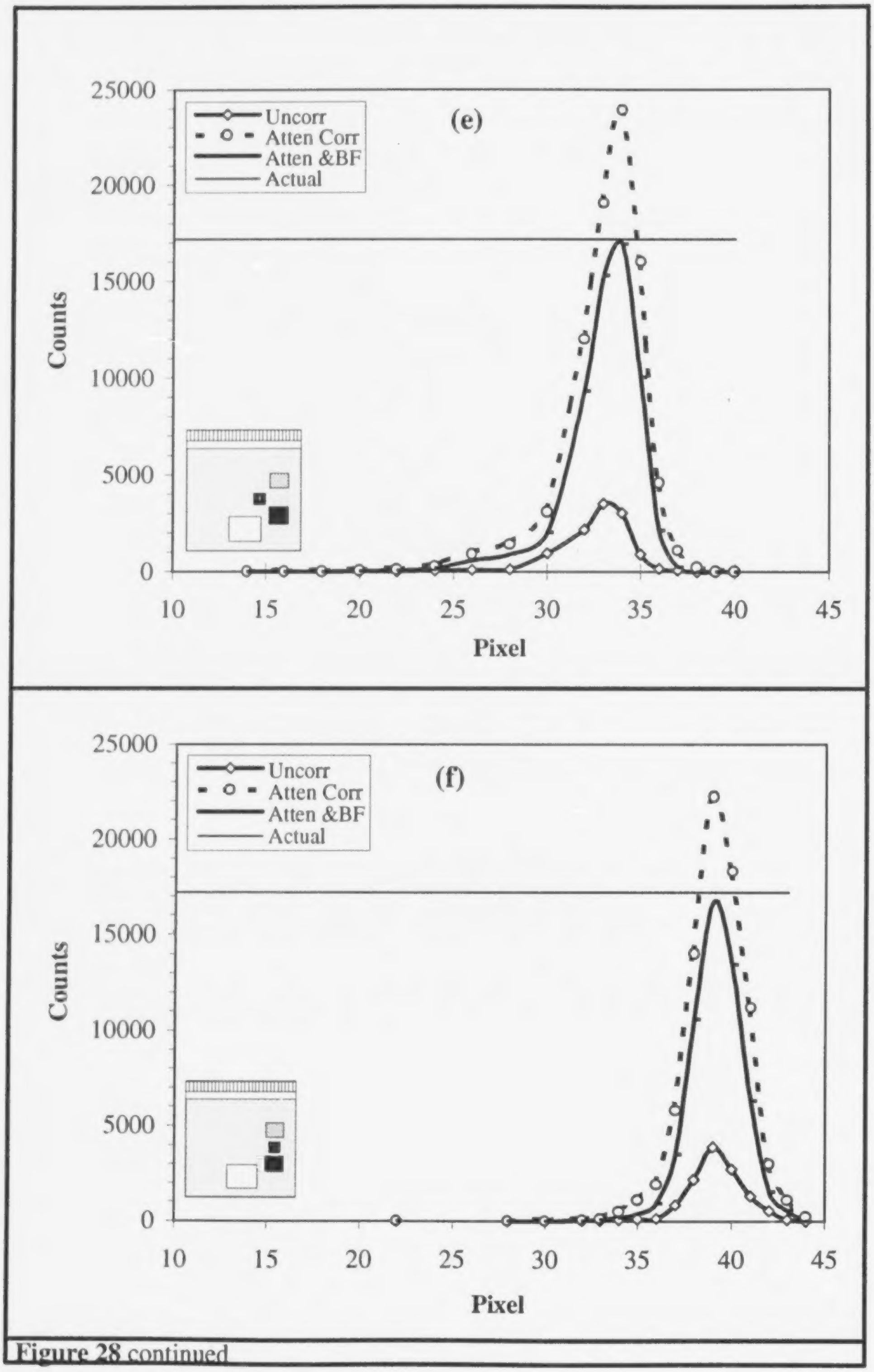

Figure 28 continued

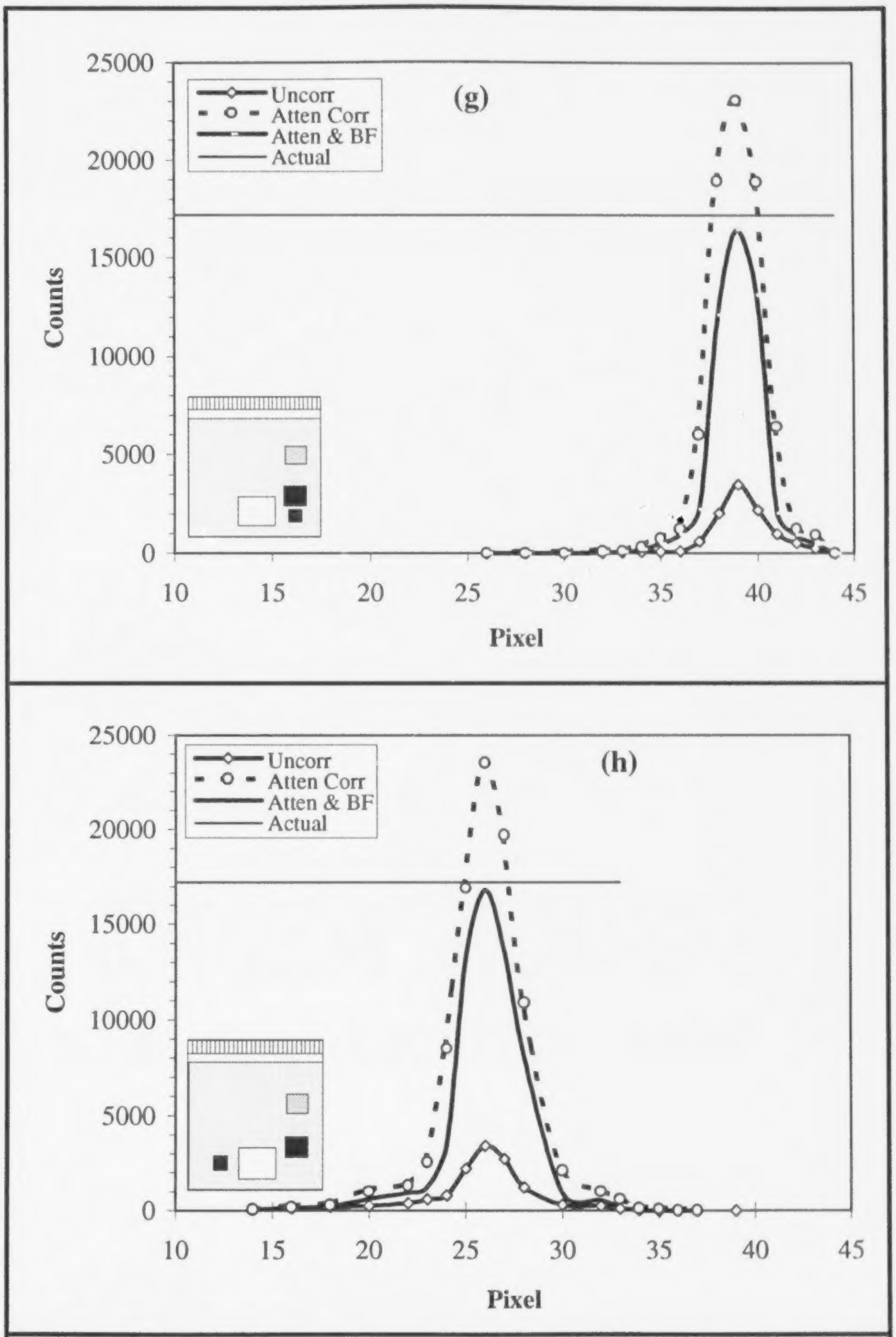

Figure 28 continued

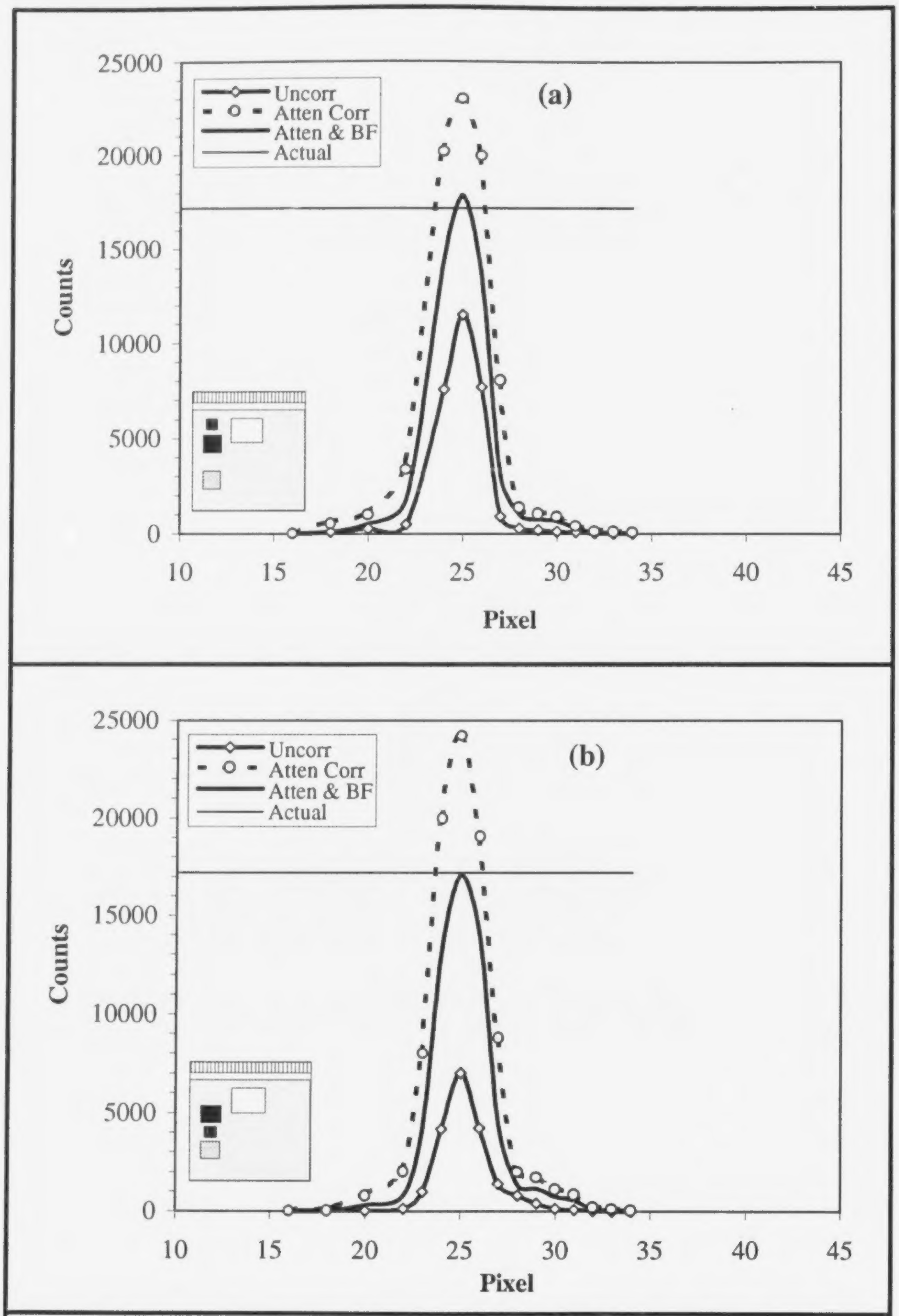

Figure 29. Projection profiles for source-phantom configuration of Figure 18(b) using volume sources. Source positions are shown in lower left hand corner. a = 9; b = 10; c = 11; d =12; e = 13; f = 14; g = 15 and f = 16.

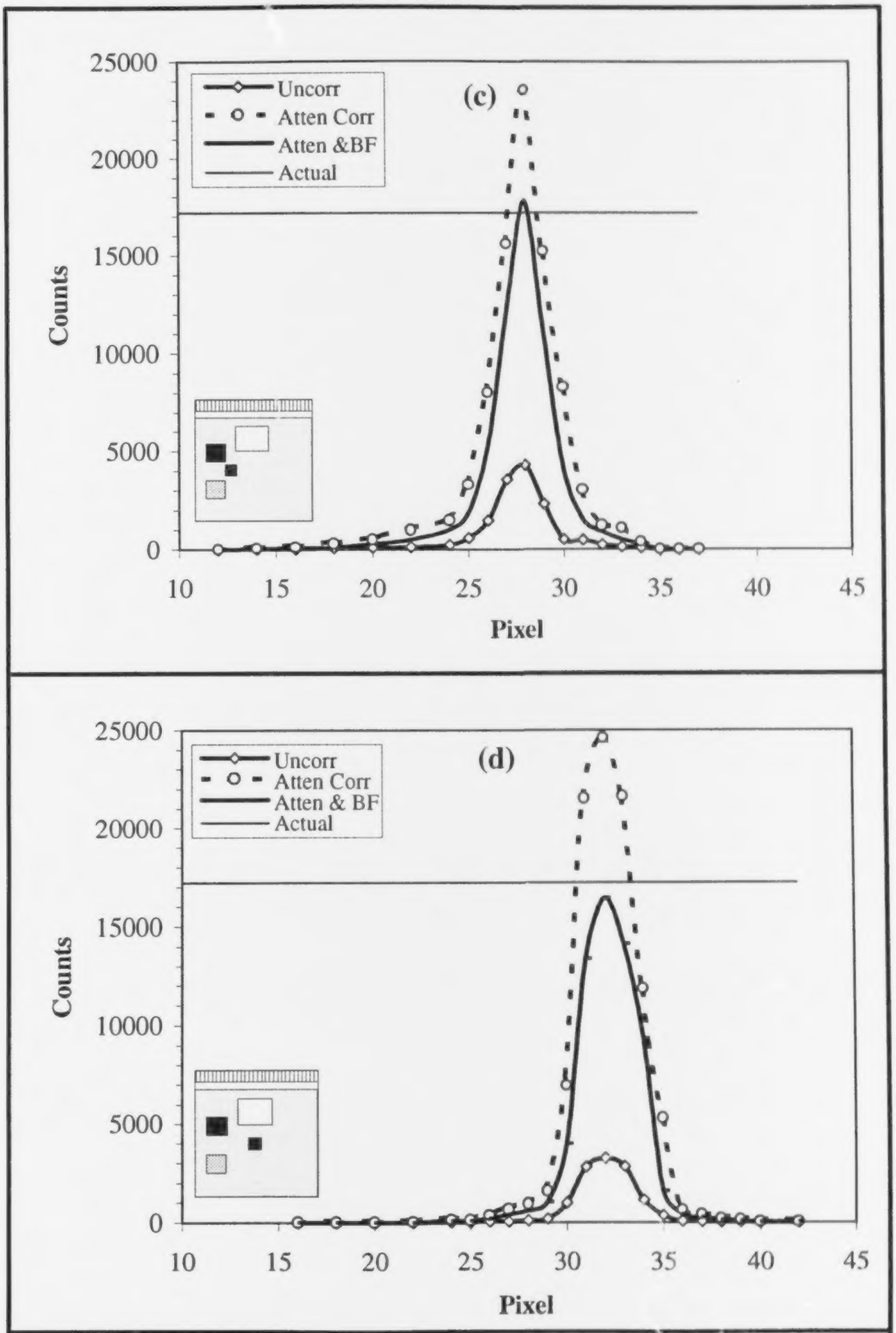

Figure 29 continued

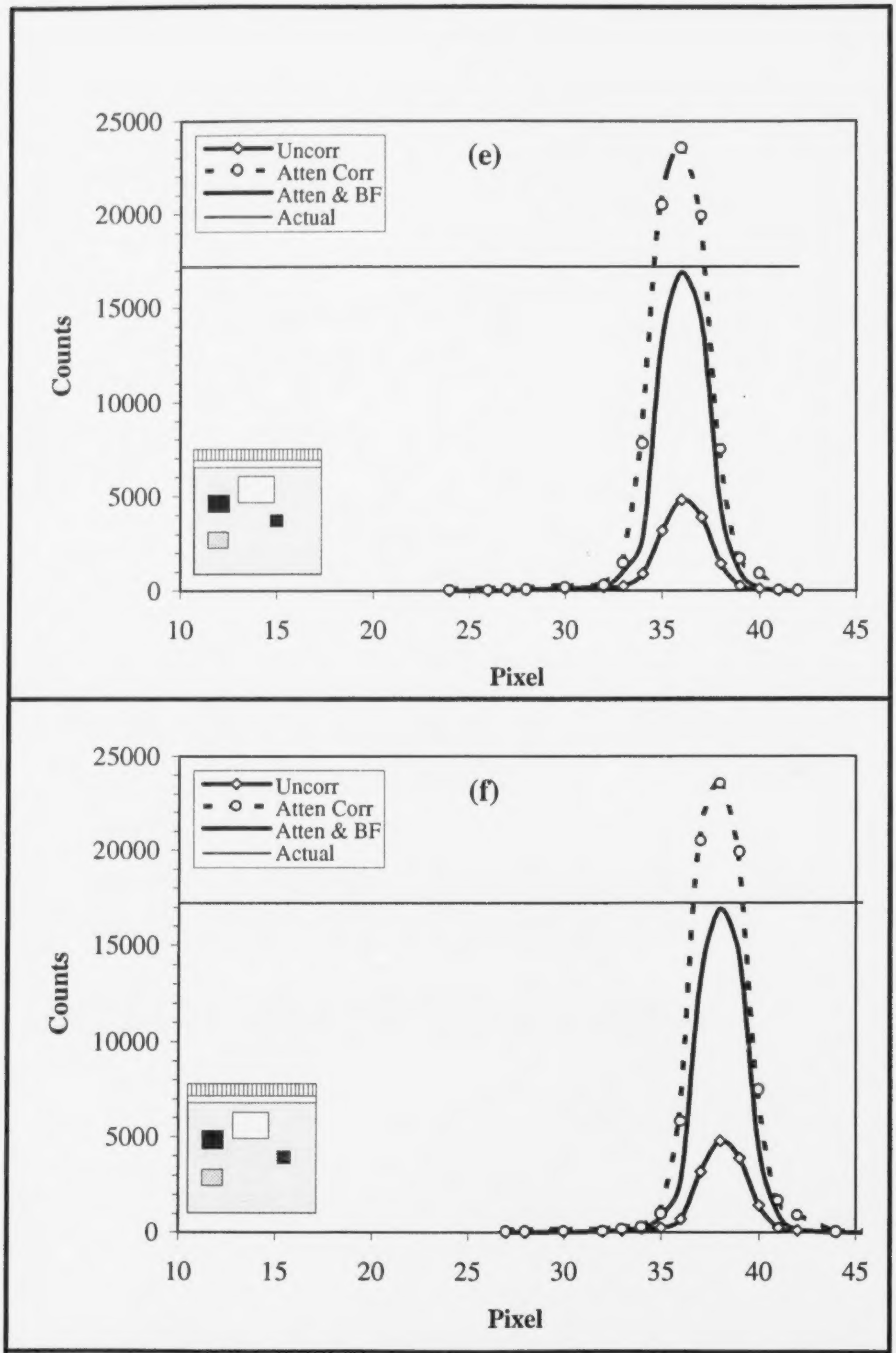

Figure 29 continued

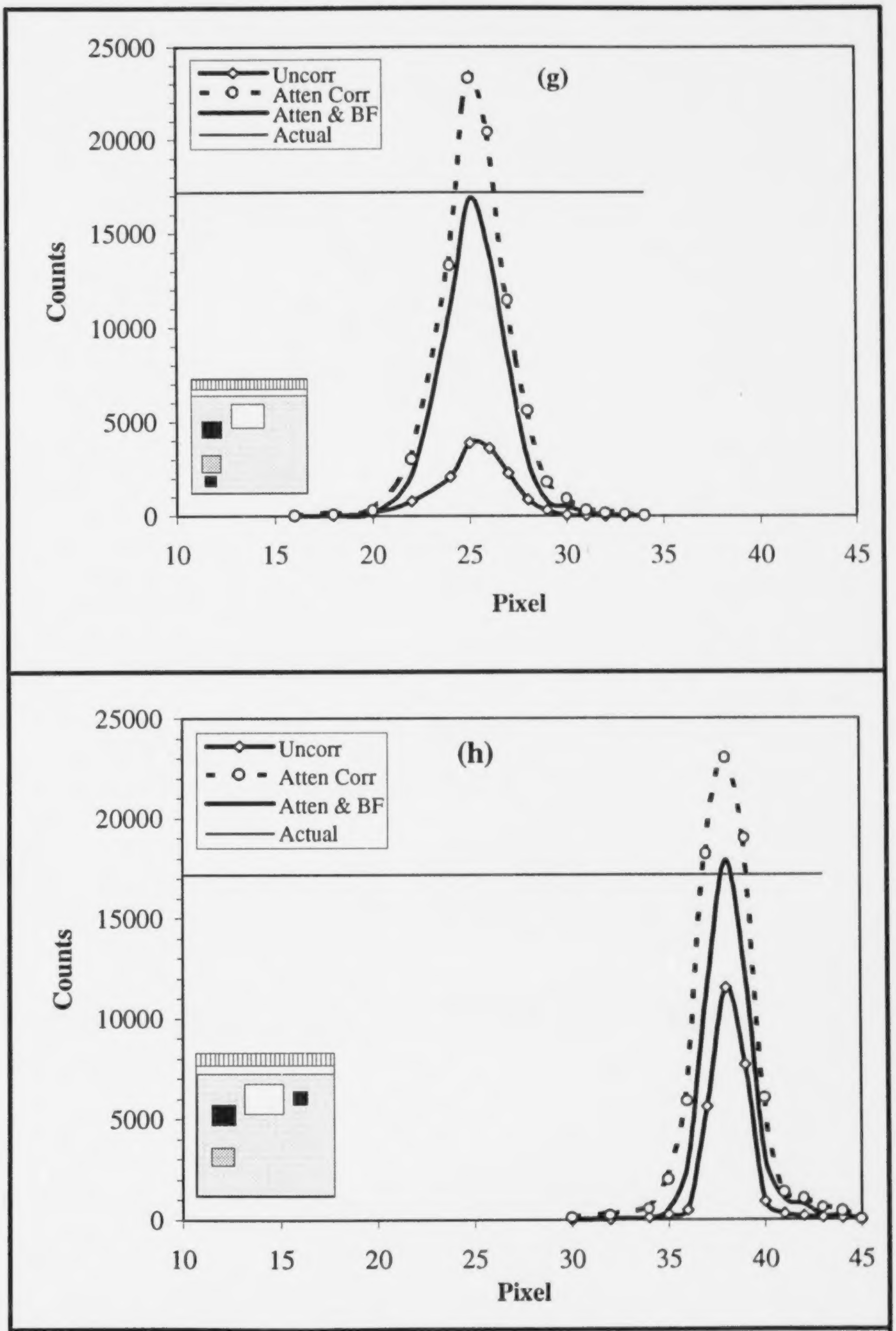

Figure 29 continued

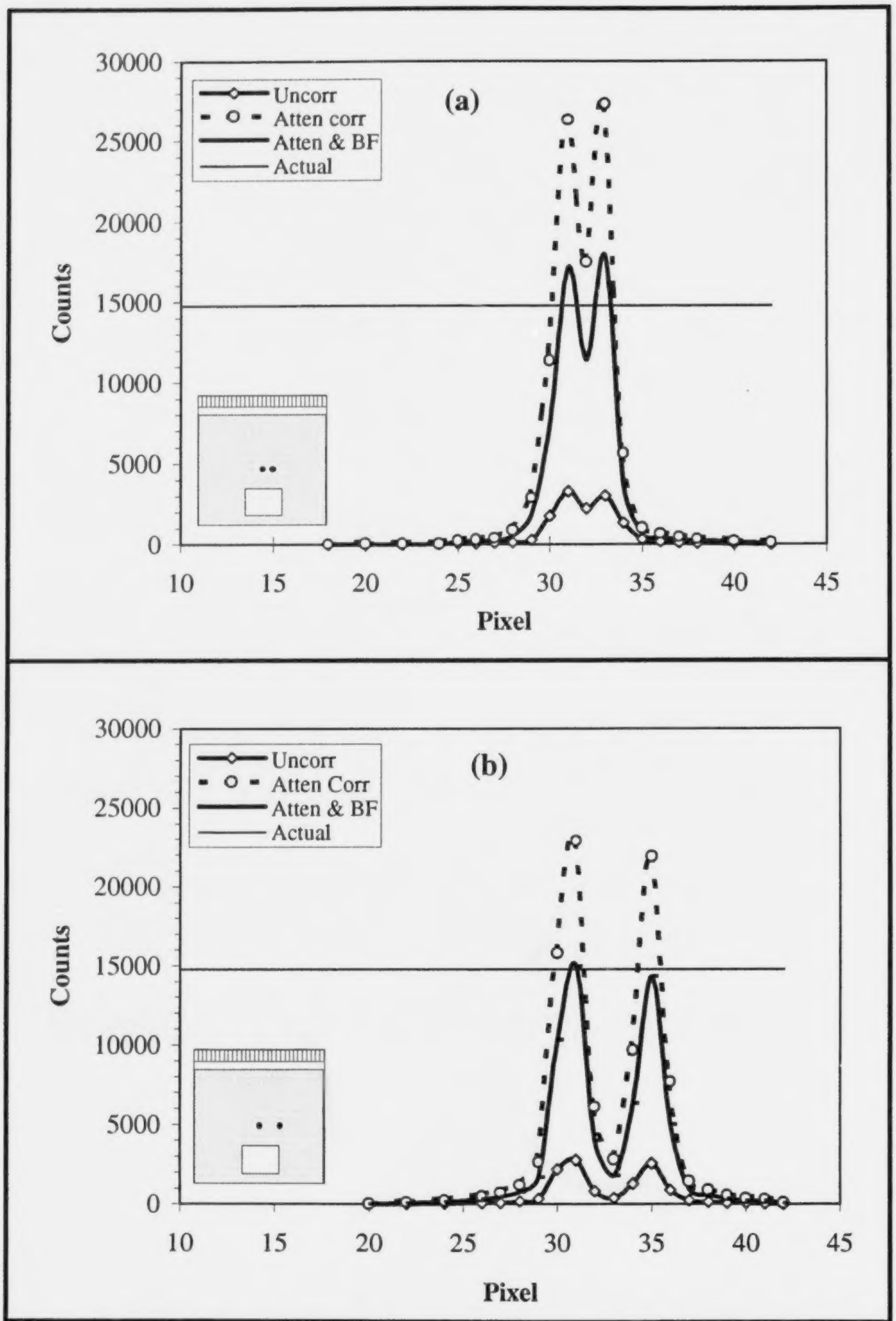

Figure 30. Projection profiles for source-detector configuration of Figure 19(a). Two line sources were separated as indicated in the figure (lower left of graph). The separation between sources were (a) 2 cm; (b) 4 cm; (c) 6 cm and (d) 8 cm.

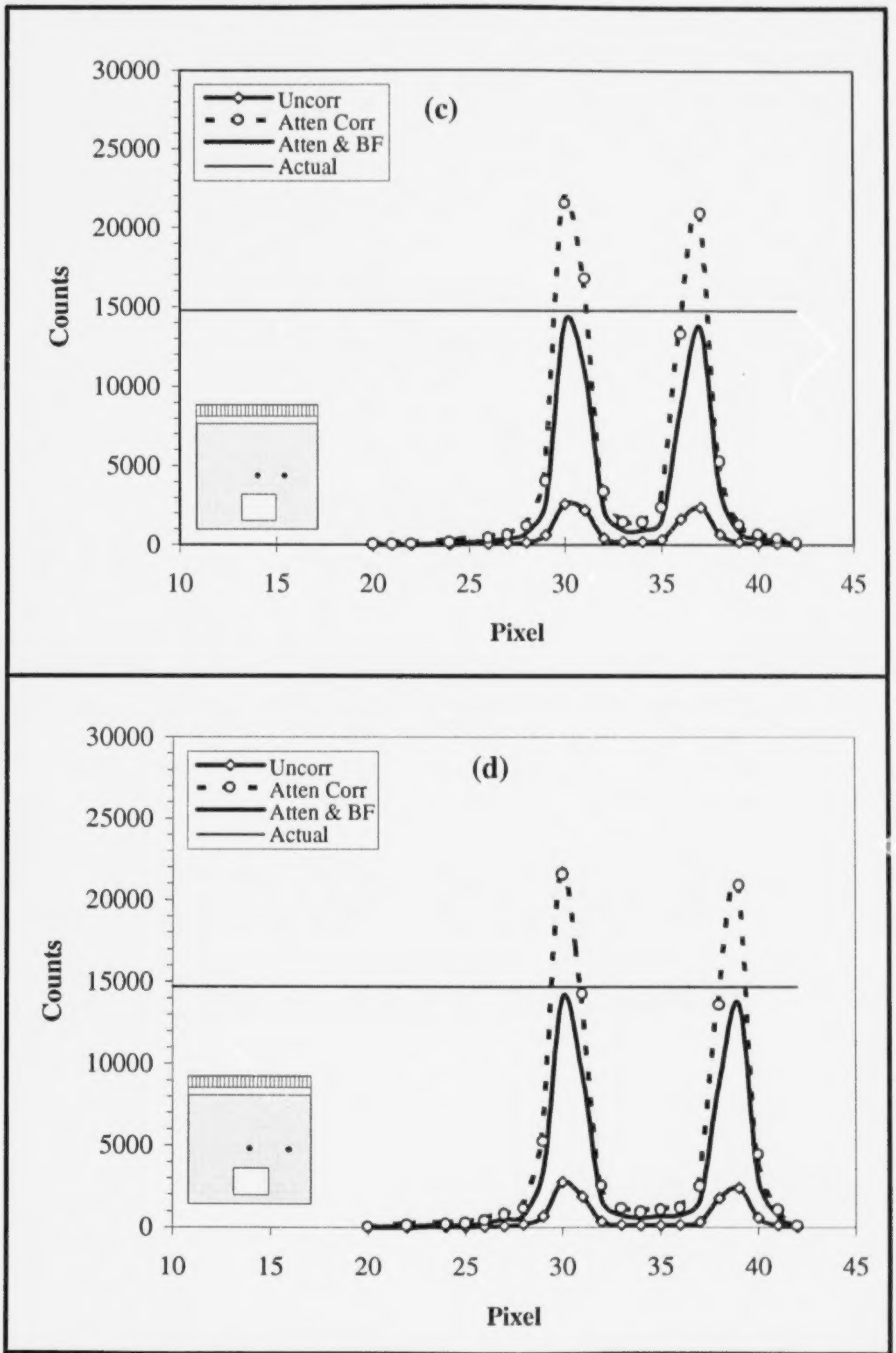

Figure 30 continued

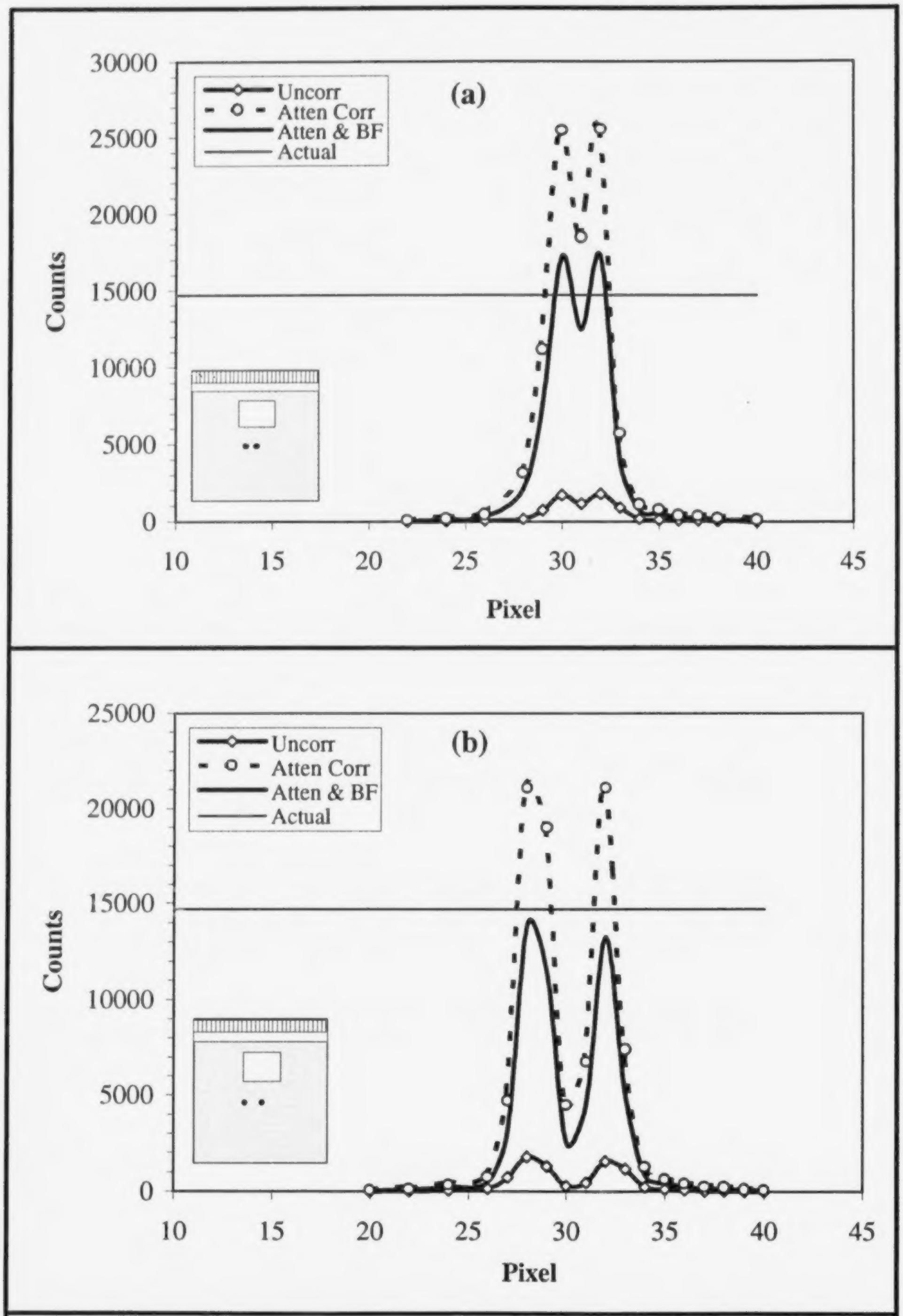

Figure 31: Projection profiles for source-detector configuration for Figure 19(b). Two line sources were separated as indicated in the figure (lower left of graph). The separation between sources were (a) 2 cm; (b) 4 cm; (c) 6 cm and (d) 8 cm.

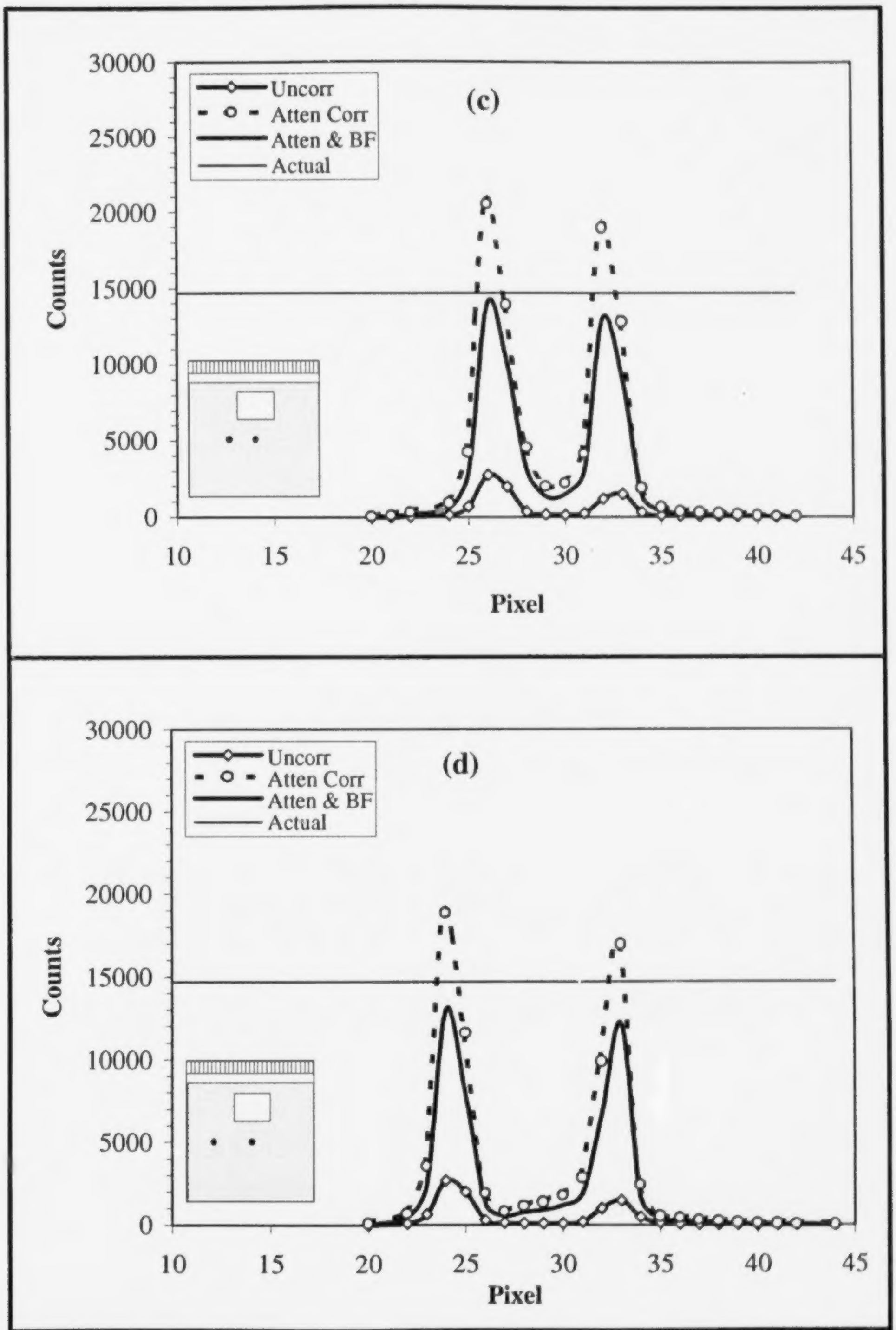

Figure 31 continued

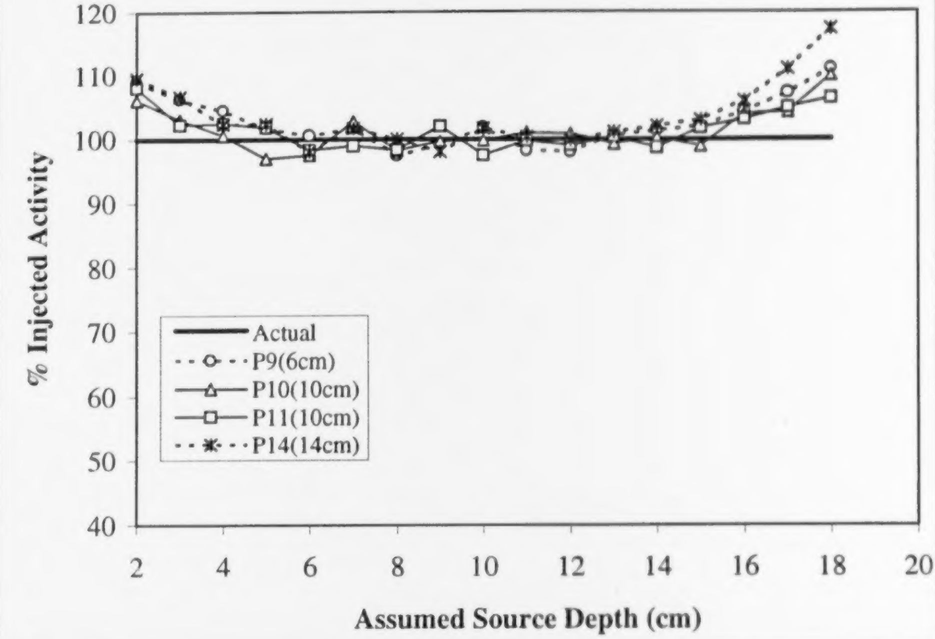

Figure 32: Variation in estimated activity with assumed source depth using the configuration shown in Figure 20.

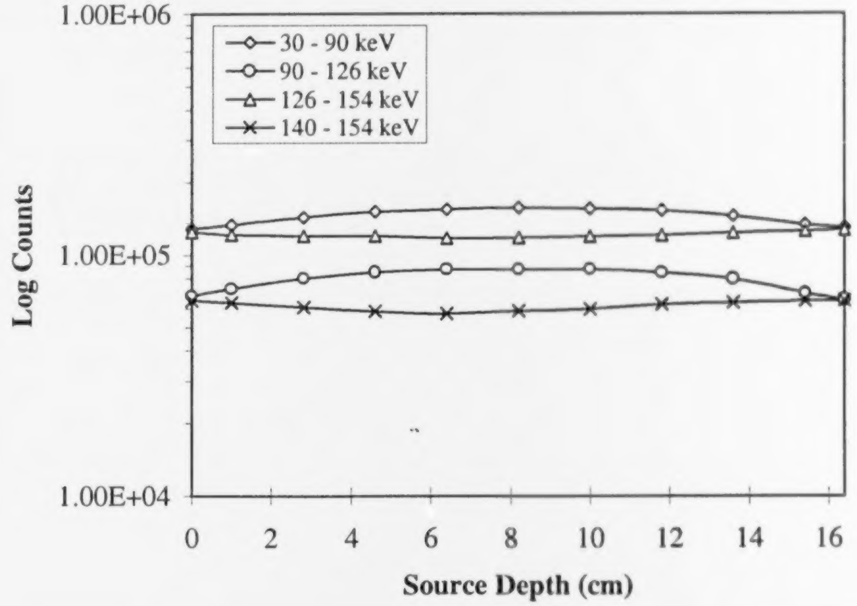

Figure 33: The geometric mean of counts for four different energy regions of the spectrum from a ^{99m}Tc line source at various depths in a perspex phantom.

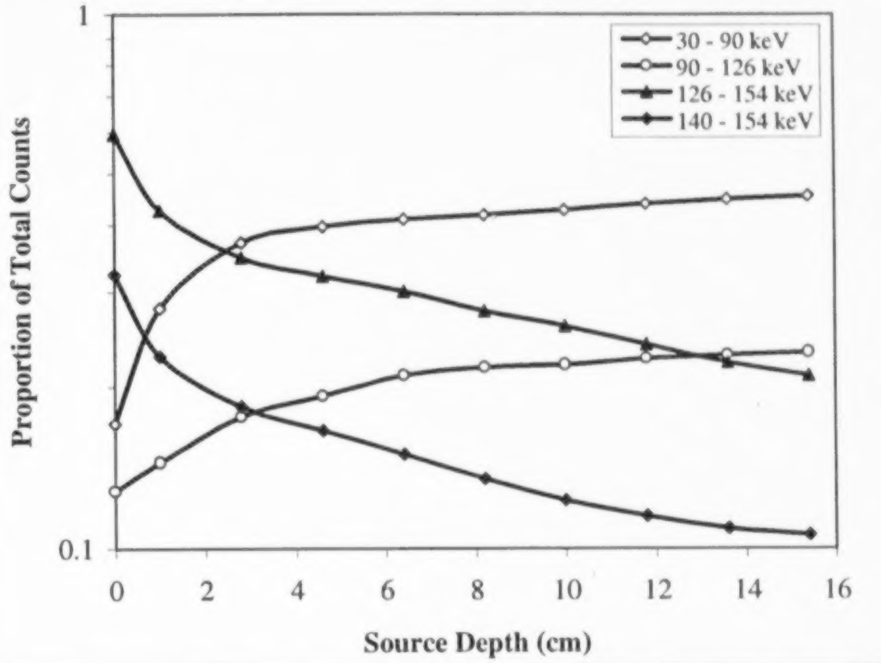

Figure 34. Variation in proportion of counts with source depth for various energy regions of the spectra from a point source.

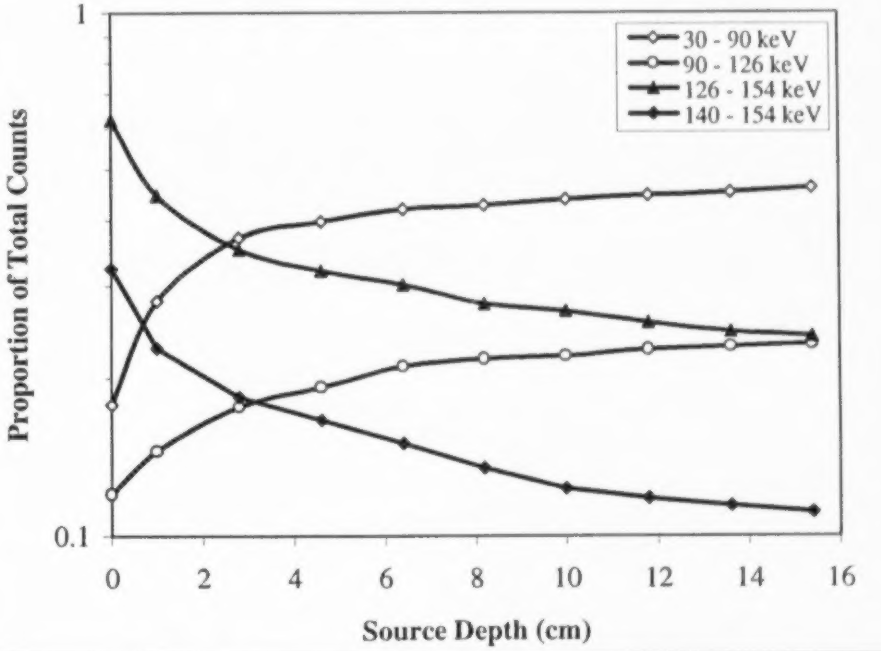

Figure 35. Variation in proportion of counts with source depth for various energy regions of the spectra from **two** point sources separated horizontally by 2 cm.

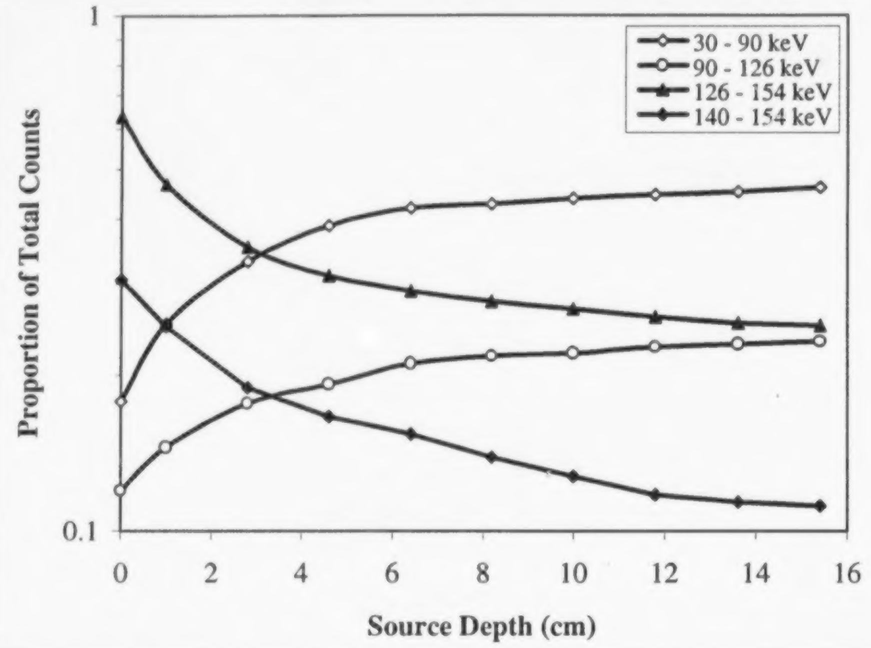

Figure 36. Same as Figure 35 except that the point sources were separated by 6 cm.

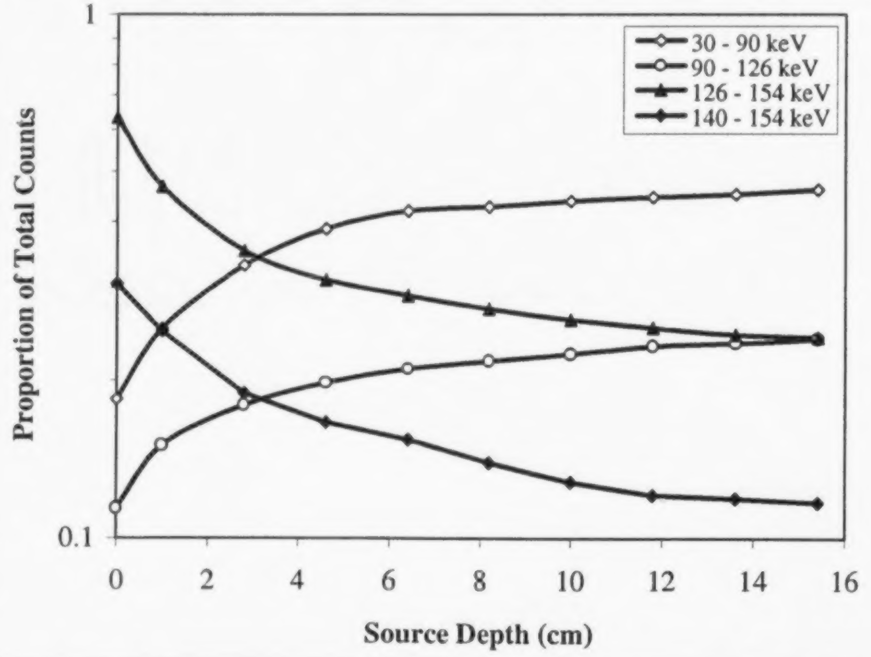

Figure 37. Same as Figure 35 except that the sources were separated by 10 cm.

Chapter 6

Clinical Applications

In the preceding chapter, an experimental validation of the new method using physical phantoms was presented and the accuracy of the method was demonstrated for various situations. However, the ultimate test is a clinical evaluation of the correction method. In this chapter, the use of the method to correct for planar images of patients is described. The chapter is divided into two major sections. In the first, a description of the methodology involved in regards to the clinical application is given and in the second, the results of the clinical evaluation are presented and discussed.

6.1 Methods and Materials

Anatomical Data

The application of the method to human studies in nuclear medicine requires the development of a diagnostically realistic model. It is essential that this model provides correct 3D anatomical geometry, thus necessitating the use of human data. CT imaging provides the 3D human anatomy data required to develop this model. Raw CT data required to construct the model was obtained from the Imaging Science Research

Laboratories, Department of Diagnostic Radiology, Yale University School of Medicine. A patient at the institution served as the source of the anatomical 3D data (93). The selected patient (adult male) height was 5 feet 10 inches (177.8 cm) and weight was 155 pounds (70 Kg). A total of 78 CT transverse slices were acquired from neck to midthigh with a 1 cm slice thickness using a 48 cm field of view. These images are available for public access (via the internet) from the aforementioned institution for use in medical research. These were downloaded from the internet as 78 individual 512 x 512 slices (i.e. each slice in a separate file) and stored accordingly on our computer system.

Development of the computerized human model

A program was written in C to pack the individual transverse slices into a single file of 78 consecutive slices and to subsequently shrink the slices into 128 x 128 x 78 voxels. The images are shown in Figure 38. This procedure reduces disk storage space for the data from 40.9 MBytes to approximately 5.11 MBytes and arranges the data into the working form required to set up the 3D human model. Although the human body consists of various tissue types, the differences in densities of individual tissues are such that they can be broadly classified as three types: 1) lung; 2) bone and 3) soft tissue. This classification allows one to put the range of Hounsfield numbers in the CT images into three distinct groups in accordance with the tissue types and to assign a density value to each tissue type. The assigned values were 0.3 gcm^{-3} (lung), 1.0 gcm^{-3} (soft tissue) and 1.85 gcm^{-3} (bone). This is summarized in Table 7. A separate program was written in C to search the pixels of the CT images and replace Hounsfield numbers deemed to be lung, bone or soft tissue with the appropriate densities. Thus the digitized human torso at this stage consists of a set of consecutive density maps (Figure 39) in which three different density values describe the pixels of the thoracic maps and two describe the pixels of the abdominal maps. Figures 40 and 41 provide more detailed views of the CT slices and corresponding density maps. An IBM RS/6000 model computer was used to run the programs. The resulting 128 x128 x 78 array was subsequently used for attenuation correction of patient images described in the following sections.

Patient studies

Patients are routinely referred to our nuclear medicine department for ventilation-perfusion lung scanning. These studies are performed using dual planar imaging with our Picker 2000 gamma camera systems. Six of the patients were selected for testing the clinical validity and accuracy of the new method. No modification was required to the existing patient preparation and acquisition protocols. Instead two additional images were acquired: one immediately after the standard ventilation scans and the other immediately after the standard perfusion scans. The procedure used was as follows. Each patient was instructed to inhale ^{99m}Tc DTPA aerosol from a nebulizer containing 1000 MBq of ^{99m}Tc DTPA. The patient was then placed supine on the couch of the gamma camera system and the routine ventilation images for diagnosis were acquired using the Picker acquisition protocols. Additionally, a subsequent, 3 min A-

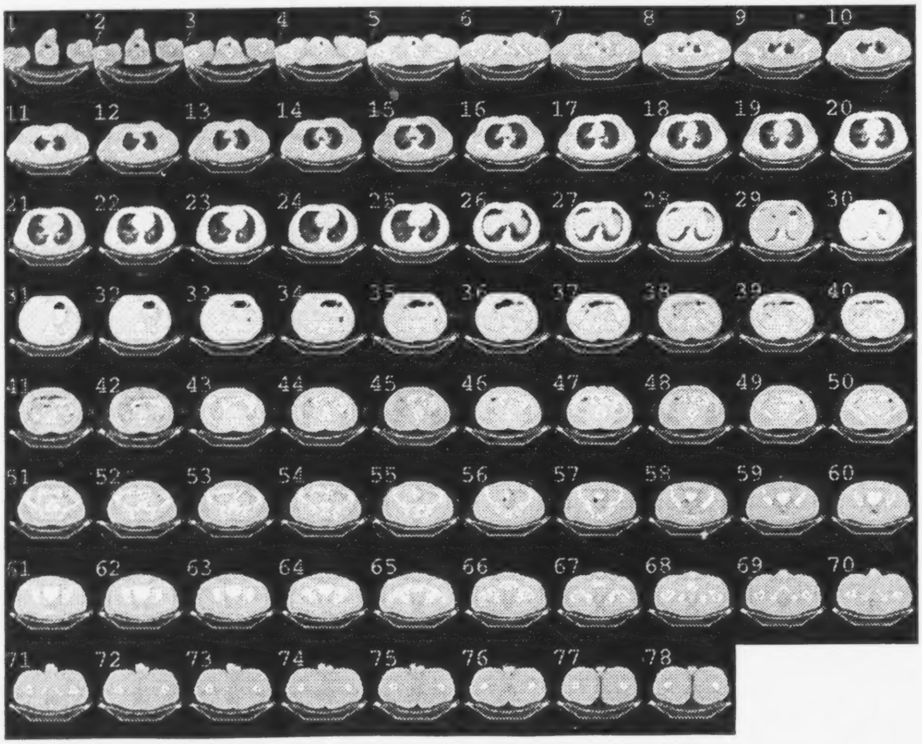

Figure 38. CT tranverse slices of the standard man from neck to midthigh.

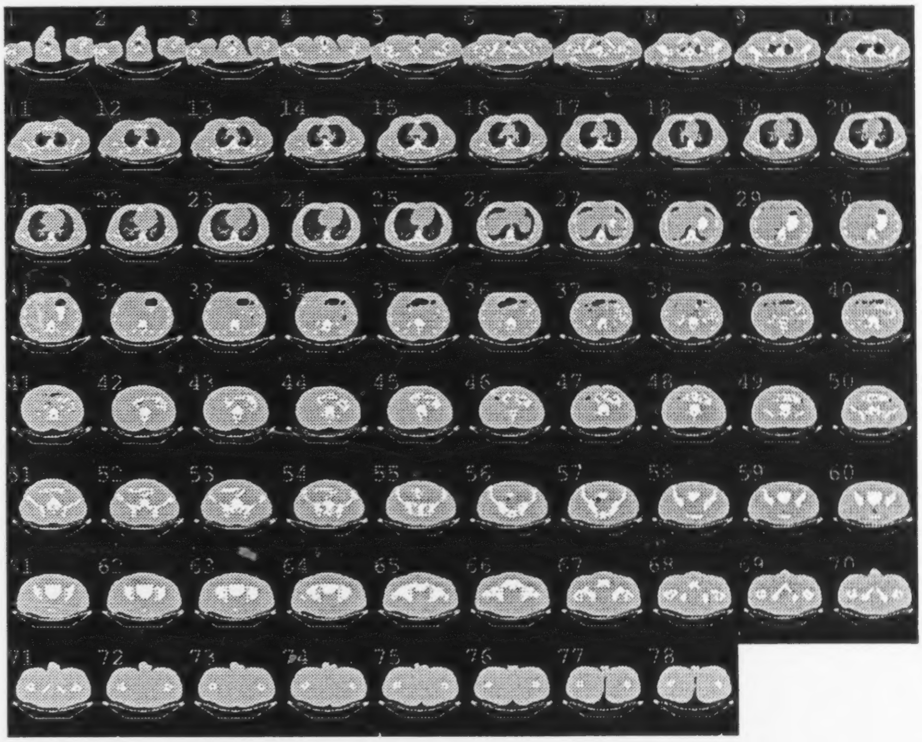

Figure 39. Density maps of the standard man from neck to midthigh.

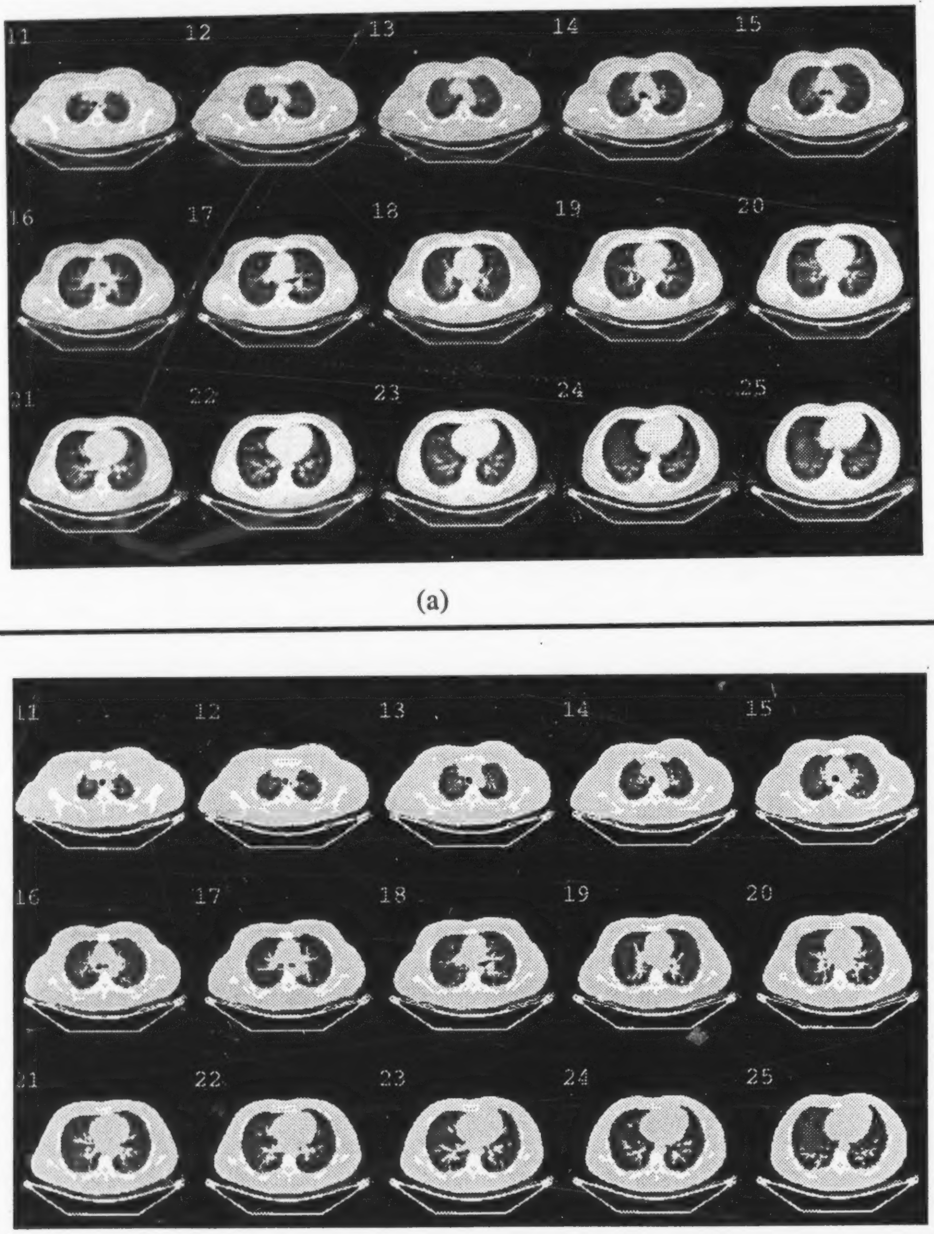

(a)

(b)

Figure 40. (a) CT slices of a section of the thorax and (b) the corresponding density maps.

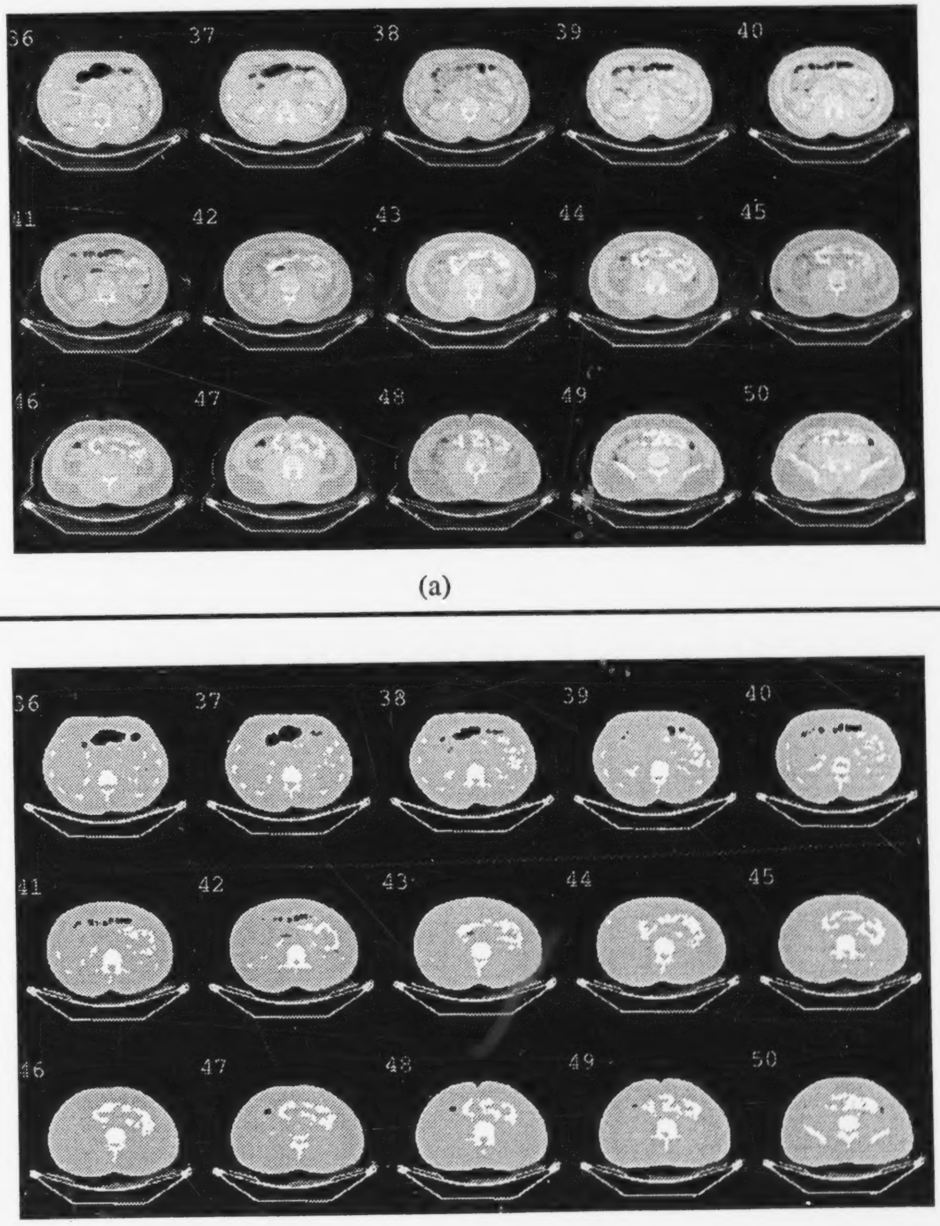

(a)

(b)

Figure 41. (a) CT slices of a section of the abdomen and (b) the corresponding density maps.

P acquisition was performed. The patient was then prepared for the perfusion study by administering 140 - 200 MBq of ^{99m}Tc MAA intravenously. As before, the routine perfusion images for diagnosis were acquired followed by an additional 3 minute A-P acquisition. The two 3 minute images were the ones used for this project. The images were acquired in 128 x 128 matrices. A 20% energy window, centered at 140 keV, was used for the acquisitions.

The fact that the ventilation study precedes the perfusion study in routine lung scanning means that the latter study may have significant contributions from the former that will affect quantification of ^{99m}Tc MAA. To overcome this a "pure" perfusion image was obtained by subtracting the 3 minute A-P ventilation study, corrected for decay between studies, from the 3 minute A-P perfusion study. Correction for decay was required in order to reduce the counts in the ventilation image to what it would be at the time when the perfusion scan was acquired. Note that due to the acquisition of the routine diagnostic images, significant time may elapse between acquisition of the two 3 minute images. To do the correction, the count in each pixel of the ventilation image was multiplied by a constant fraction, determined using Equation 9, for the time elapsed between the two 3 minute scans.

It was essential that patients with normal lung scans be used to test the method. Since it was impossible to ascertain this information prior to imaging, patient studies were selected if the ventilation-perfusion scans appeared normal. Normal lung studies were required to test the new method for two reasons: 1) it was felt that quantification of activity in an organ in the thorax would provide a good test for the new method because it consists of the widest variety of tissue types and 2) it has been assumed in other lung quantification studies (22) that when ^{99m}Tc MAA is administered for lung perfusion studies, all of the radioactive particles are trapped in the pulmonary capillary bed just after injection (94). The mean chest thickness of each patient was determined for use in the attenuation correction calculations. This was estimated from two measurements taken with calipers over the sternal notch and the xiphoid process.

Implementation of the model

The digitized human model provides the clinically realistic density distribution of the human body from neck to midthigh that is required for attenuation correction. Thus the model can be used to provide attenuation correction data for any organ within this region of the body. To apply the model in the quantification of lung activity, the thoracic region of the digitized torso was selected. The density maps of this region provided the required attenuation correction data.

To implement of the model, it was necessary to determine the dimension of the field of view of the gamma camera, in particular the dimension along the length of the patient (adult) in the thoracic region, and subsequently the number of 1 cm thick transverse slices of the torso that would make up this dimension. This step is necessary in order to establish proper correlation between the region of the nuclear medicine patient viewed by the gamma camera and the slices of the digitized torso to be used for the correction. To confirm that the appropriate region of the torso was selected, the slices were displayed on the monitor thus allowing the user to see that the organ of interest (lung) is fully contained within the selected slices. The entire process is required to be done only once using an adult patient.

If the number of slices required is n, then the CT array that describes the volume of interest consists of n 128 x 128 matrices. An algorithm was developed in C with a user interface for input of the number of slices, n, and the slice number along the digitized torso at which the selection starts. The algorithm then interpolates the n slices selected to 128 slices. This was done by dividing the volume into thinner slices, each approximately equal to the pixel size in a 128 x 128 matrix for the gamma camera field of view. The calculation of the nuclear medicine image pixel size was described in section 5.1. The resulting block of data now consists of a 128 x 128 x 128 array. The significance of this will become more obvious later in this section.

The cubic array serves as the input to the algorithm that was developed (and described in section 5.1) for creating opposing pairs of 2D correction maps from 3D data. Using this algorithm, a coronal plane was defined through the centre of the thorax and an integration was performed over all voxels from this plane to the anterior surface of the thorax to form the anterior 2D correction map and similarly for the posterior. If the average chest thickness of the patient was different from that of the standard man (20 cm), the algorithm used a modifying factor determined by the ratio of the two measurements to adjust the standard man voxel size accordingly. An example of the anterior and posterior correction maps is shown in Figure 42. Note that the definition of the coronal plane about which the 3D structure is collapsed is not crucial for accurate results as demonstrated in Figure 32 (section 5.2), except where the depth of the coronal plane is close to the surface of the body. The resulting 2D correction maps are 128 x 128 matrices. Recall that the ventilation-perfusion scans were acquired in 128 x 128 matrices. In the following section the alignment and combination of these images are discussed.

Alignment and combination of images

One of the considerations to be addressed in regards to the nuclear medicine images prior to their combination with the standard man data for correction, is to ensure proper alignment. There must be proper alignment between: 1) the ventilation and perfusion images before subtraction to produce the "pure" perfusion image and 2) the "pure" perfusion image and the 2D correction map. For the ventilation and perfusion images, it was essential to view and align the images before subtraction because of changes in patient and/or camera position from one study to the next. The image alignment requires that the organ of interest (lung) occupy identical pixel locations in each image matrix (i.e. the centre of the lungs should be at the same coordinates in the 128 x 128 image matrix in both ventilation and perfusion images).

The images to be aligned were displayed adjacent to each other, using a commercial software package (Alice), so that both image matrices were at the same level on the monitor. A horizontal line was then drawn through the centre of the lungs in the ventilation image. The same was done for the perfusion image and a calibrated ruler (software built-in tool) was used to determine the vertical separation in pixels between them. A program written in C used this information to vertically shift the position of the lungs by the required number of pixels in one image matrix with respect to the other to produce horizontal alignment. An example of this alignment is shown in Figure 43. Vertical alignment was performed in a similar fashion when required. (The latter was generally, successfully achieved at acquisition setup by aligning the central axis of the gamma camera with the mid-sagittal plane of the patient.) Once the images were satisfactorily aligned, pixel by pixel subtraction of the ventilation image from the perfusion image was performed to produce the "pure" perfusion image.

The human correction maps were displayed along with the "pure" perfusion images and the aforementioned alignment procedure performed as required. In some cases it was necessary to shrink or stretch the image of the lungs in the correction maps (i.e. the standard man lungs) to fit that of the nuclear medicine patients. To avoid performing this procedure repeatedly for patients whose lung images do not readily fit the standard man lung image, the model created a set of lung images of different sizes within 128 x 128 matrices as variations from the standard man lung image. Four examples of such variations are shown in Figure 44.

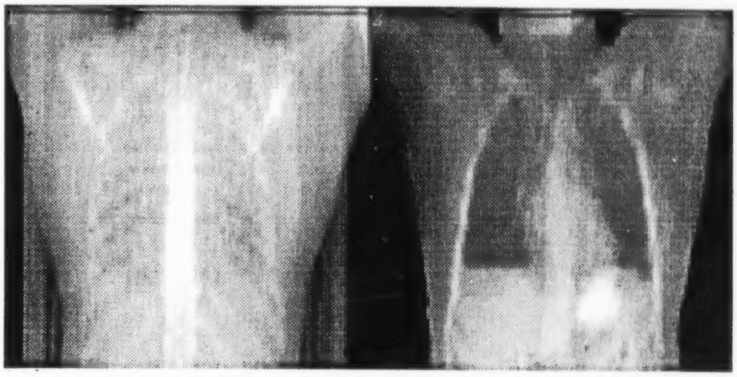

Figure 42. (a) Posterior (1) and anterior (2) correction maps of the collapsed thorax.

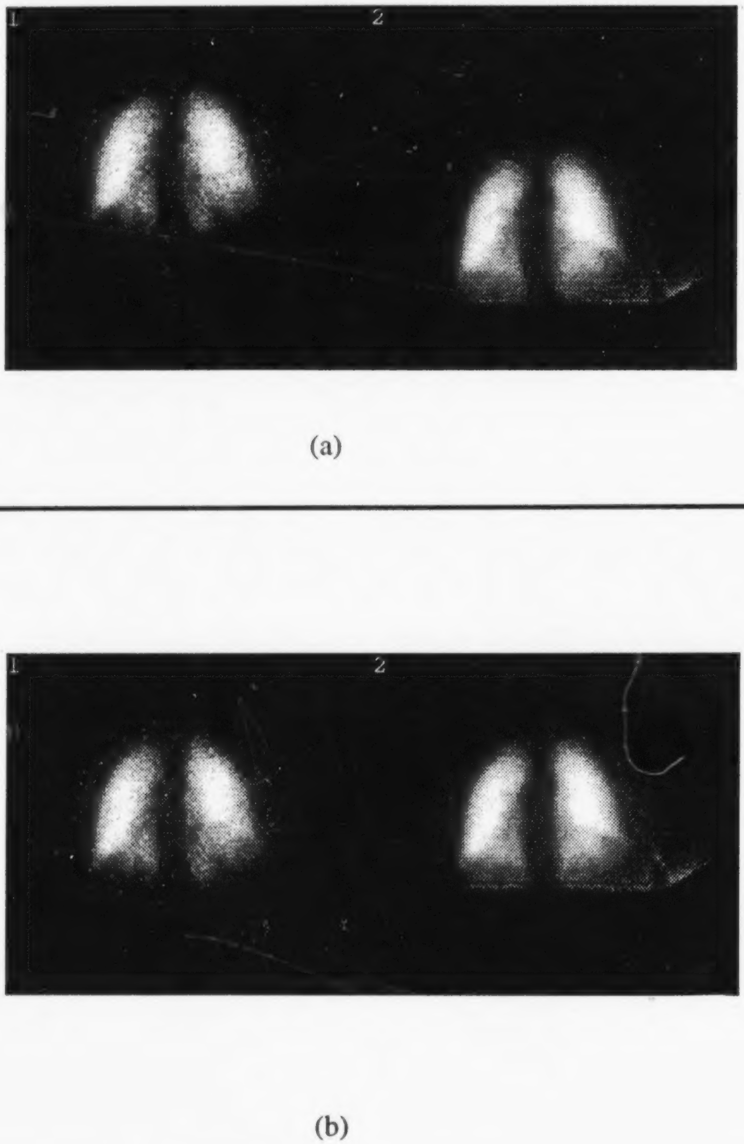

Figure 43. (a) Non-aligned ventilation and perfusion images. (b) The horizontally aligned images.

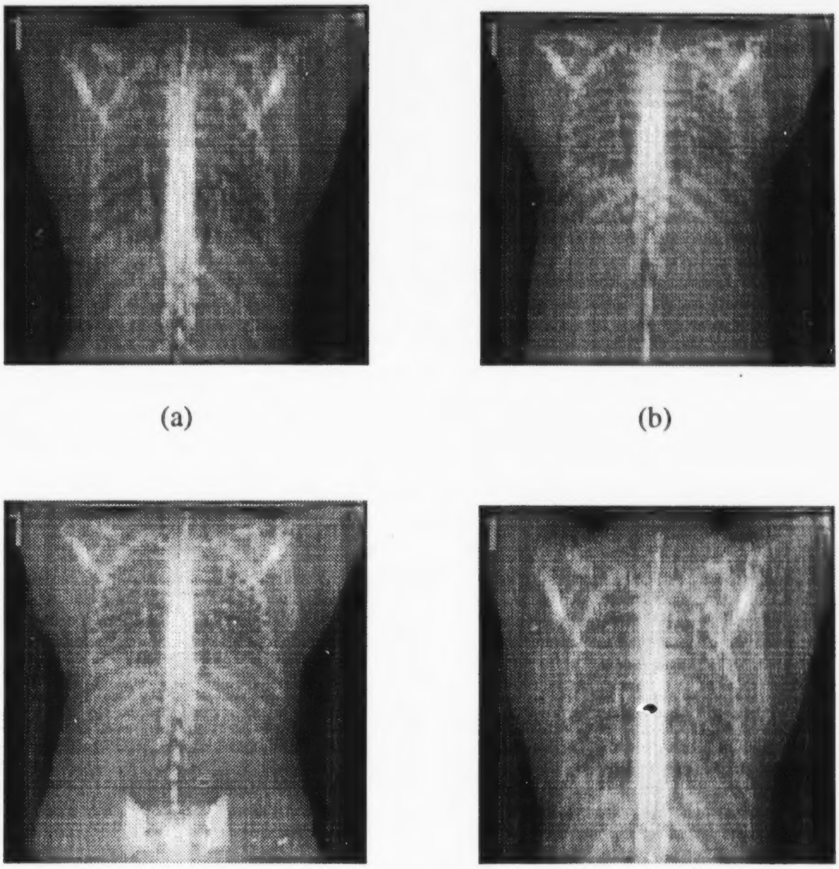

(a) (b)

(c) (d)

Figure 44. Examples of 2D correction maps (posterior) with different lung sizes. Images (a) to (d) were generated from collapsed CT slices of the same human being.

Prior to correction of the nuclear medicine image with the attenuation data (2D correction maps) of the standard man lungs, the "pure" perfusion image was displayed alongside a set of predetermined lung images and the one that appeared to provide the best fit to the patient lung image was selected for correction. There were some adult patients whose lung images did not appropriately fit any of the pre-determined lung sizes of the 2D correction maps, thus were considered unsuitable. Once the selection was made, both images (i.e. the patient lung images and the 2D correction maps) were then read into a correction algorithm which transformed the nuclear medicine image data to an appropriate format consistent with that of the correction maps and subsequently combined the images as described in the theory (chapter 4), to produce attenuation corrected nuclear medicine images of the lungs. The next stage involves the application of clinically realistic scatter correction to these images and is explained in the following section.

Monte Carlo simulation of clinically realistic buildup

Earlier in this project, Monte Carlo techniques were used to simulate standard phantoms (i.e. of regular geometries). However, the human body is much more complex and irregular in geometry than is represented by the perspex phantoms that were simulated. Consequently, the buildup data obtained from phantoms cannot provide accurate scatter correction in humans. This can only be achieved by providing the Monte Carlo program with human data. Thus the setup of the human model requires the use of the anthropomorphic phantom to study the buildup of scatter in clinically realistic situations. To simulate the buildup factors for the human body, slices of the digitized torso were read into the Monte Carlo program and used as the ideal nonhomogeneous phantom. For simulation of the buildup factors, the organ of interest (lungs) was defined as all voxels within the volume with a value equal to 0.3 gcm^{-3} (approximate density of lungs) and the simulated activity was assumed to be uniformly distributed in this volume. The voxels within the organ that are assumed sites for gamma emission are randomly selected as explained in Chapter 4. Similarly, bone and soft tissue were defined as regions within the 3D array with voxel values of 1.85 gcm^{-3} and 1.0 gcm^{-3} respectively. The buildup factors were calculated from the simulated data using Equation 22.

6.2 Results and Discussion

The new method was tested on six patients as indicated in Table 8. The table includes the age, weight, sex and average chest thickness of each patient. The number of patients used for this study was restricted by several factors. These included: 1) a significant proportion of the patients did not have normal lung scans which was required for testing the method; 2) some patients with normal scans as unsuitable for the model; and 3) the acquisitions were dependent on workload, clinical situation and pending cases in the nuclear medicine department.

The results from the studies performed on these patients are listed in Tables 9 and 10. The counts indicated for the "pure" perfusion image (Table 9), were obtained from the

ROI of the subtracted image. The new method requires the use of this image for pixel by pixel correction and image combination with the 2D correction map. Table 10 shows the injected lung activity and the calculated lung activity based on the new method and the GM approach. The percentage error associated with each method is also given. The injected activity varied from 145 MBq for patient # 4 at 54.55 Kg (120 pounds) to 176 Mbq for patient # 6 at 84.55 Kg (186 pounds). The results indicate that the clinical application of the new method produced accurate results. Errors obtained range from 1.5% to 4.5%. For the same patients the GM method produced errors ranging from 4.7% to 13.8%. Although the number of patients studied is not enough to demonstrate a trend in the GM method, it appears that the magnitude of the errors indicated in Table 10 increases with patient thickness. A likely explanation for this is that the assumption of the GM method that a fixed proportion of the primary beam can be replaced by scattered photons, becomes less reliable with increased scattering produced by increasing thickness of attenuating medium. Thus the commonly used broad beam linear attenuation coefficient value of 0.12 cm^{-1} may need to be reduced to better compensate for the increased scatter produced by relatively thick patients. The same effect was not observed for the new method.

The accuracy of the clinical results using the human model suggests that the assumption that the body consists of three tissue types; lung, bone and soft tissue, is reasonable. Thus the density maps obtained provided good representation of the human anatomy. Figures 40 and 41 show images of sections of the thorax and abdomen of the standard man used in this work. The raw CT slices are displayed in Figures 40(a) and 41(a) and the corresponding density maps in Figures 40(b) and 41(b) respectively. It can be seen that the density maps compare well with the CT slices of the same cross sections. Essentially, the model can be applied to any organ in the human torso. As demonstrated in Figure 44, the model can be manipulated to produce appropriate correction maps of organ sizes other than that of the standard man. The four images shown originate from the same human being and are magnified by a factor of 2. The collapsed 3D data produced 2D correction maps of relatively good contrast. This is important for proper delineation of the organ in the correction maps which is essential for selecting the appropriate model that is to be applied to the nuclear medicine image.

As indicated at the beginning of this chapter, the model was developed from whole body CT scans of a male patient (standard man). Thus it may seem reasonable to restrict its application to adult male patients that would be appropriate for the model. However, as shown in Tables 8 to 10, the model was successfully applied to both male and female patients, though one had to exercise reasonable discretion in selecting female lung patients due to anatomical difference in the thoracic region. The posterior views of the nuclear medicine images and correction map are shown in Figures 45 to 50. Each figure shows the result in subtracting the ventilation image (1) from the perfusion image (2) to obtain the "pure" perfusion image (3). The differences in counts in the images are not readily obvious from the printed images, however, are significant as indicated in Table 9. It is image 3 that is combined with the 2D correction map (4) to produce the corrected image (5). The method is simpler in the absence of a ventilation study where only a perfusion study is performed. In this case, the image obtained can be applied directly to the correction map. Slight overcorrection observed in Table 10 for the new method is, in addition to those already discussed, probably due to systematic errors in the subtraction of the ventilation image from the perfusion image (Section 6.1).

Finally, Monte Carlo simulations of the buildup factors in lungs using the human CT slices gave an average value of 1.14. There was no significant variation in lung buildup factors for the lung sizes used in this work. This is not surprising as Wu (31) demonstrated that for two sources of the same type, the difference in buildup factors will be significant only if one is several times larger than the other and is relatively deep in the body. Such magnitude of difference in adult lung sizes was not encountered. Consequently, the average buildup factor was applied to all patients. The use of the same buildup factor for each patient simplifies the procedure and obviates the need for individual buildup factor determination. The accuracy of the results obtained is indicative of the validity of this approach. If there were significant differences in the simulated buildup factors for the models of the 3D data used, then a look-up table consisting of the various buildup factors would be used to provide the appropriate values for the model.

Table 7. Tissue types used in model and the assigned densities.

Tissue Type	Lung	Soft Tissue	Bone
Density (gcm^{-3})	0.3	1.0	1.85

Table 8. Patient information including weight and chest thickness.

Patient	Age (yrs)	Weight (Kg)	Sex	Ave. Chest Thickness (cm)
1	72	63.64	F	19.5
2	56	75	M	22
3	77	72.73	M	21
4	49	59.1	F	19.7
5	39	65.91	F	22
6	57	84.55	M	23.5

Table 9. ROI counts for the ventilation (Vent), Perfusion (Perf) and "Pure" Perfusion (P. Perf) images.

Patient	View	Vent. ROI	Perf. ROI	P. Perf. ROI
1	Ant	165594	1034135	868521
	Post	167854	1049638	881743
2	Ant	178401	1007915	830014
	Post	180416	1022349	842173
3	Ant	180103	966552	786479
	Post	181693	977013	796380
4	Ant	169950	983460	813510
	Post	167982	988631	820649
5	Ant	173471	977503	804032
	Post	171242	983266	812019
6	Ant	178610	954761	831342
	Post	178843	942173	846232

Table 10. Injected and calculated activities using both methods and the errors associated with them.

Patient	Injected activity (MBq)	New method (MBq)	GM (MBq)	Percentage error using new method	Percentage error using GM
1	152	156	159.1	2.6	4.7
2	164	170.1	181	3.7	10.4
3	151	155.7	162.5	3.1	6.8
4	145	147.1	156.1	1.5	7.6
5	158	162	171.3	2.5	8.4
6	176	184	200.3	4.5	13.8

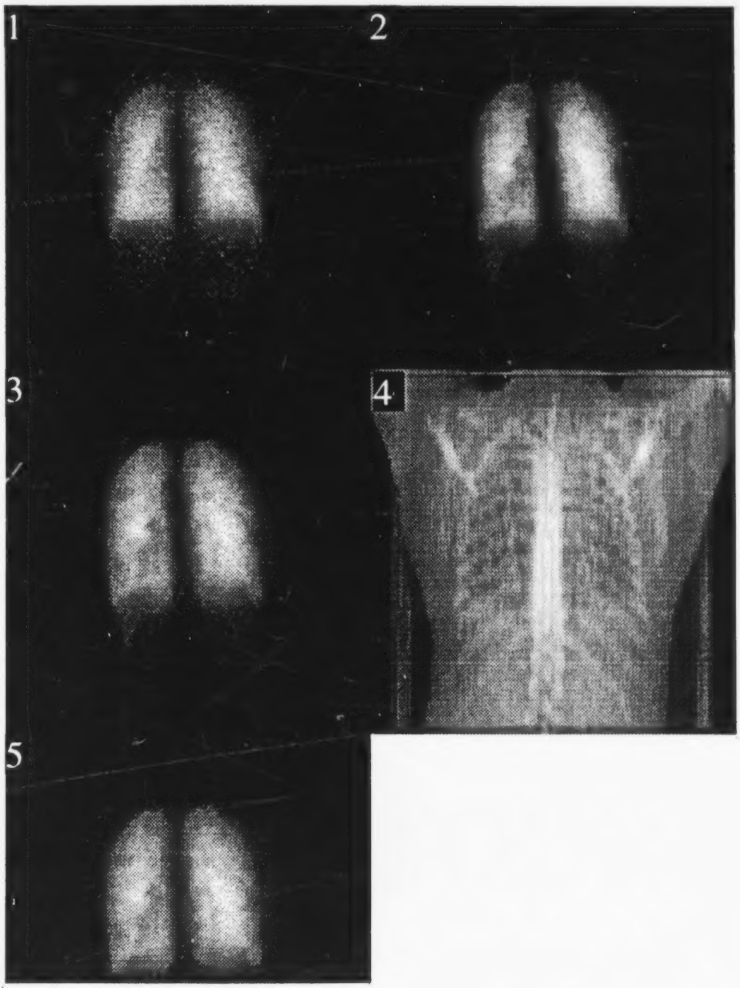

Figure 45. Patient #1: 1) ventilation, 2) perfusion, 3) "pure" perfusion, 4) 2D correction map and 5) the corrected image. All are posterior views.

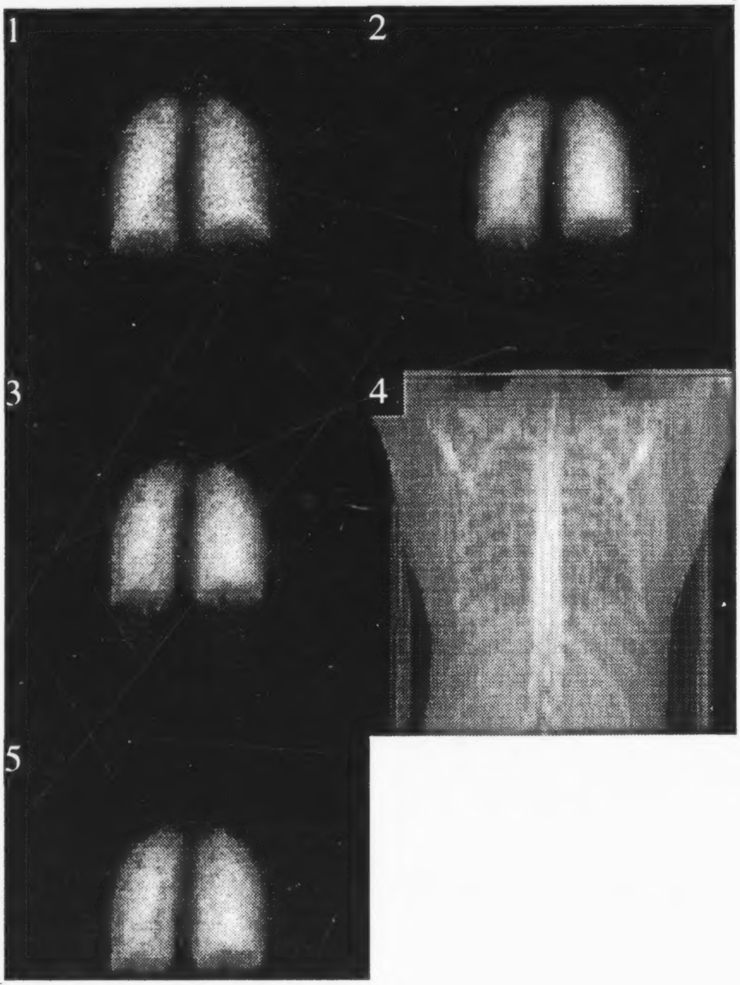

Figure 46. Patient #2: 1) ventilation, 2) perfusion, 3) "pure" perfusion, 4) 2D correction map and 5) the corrected image. All are posterior views.

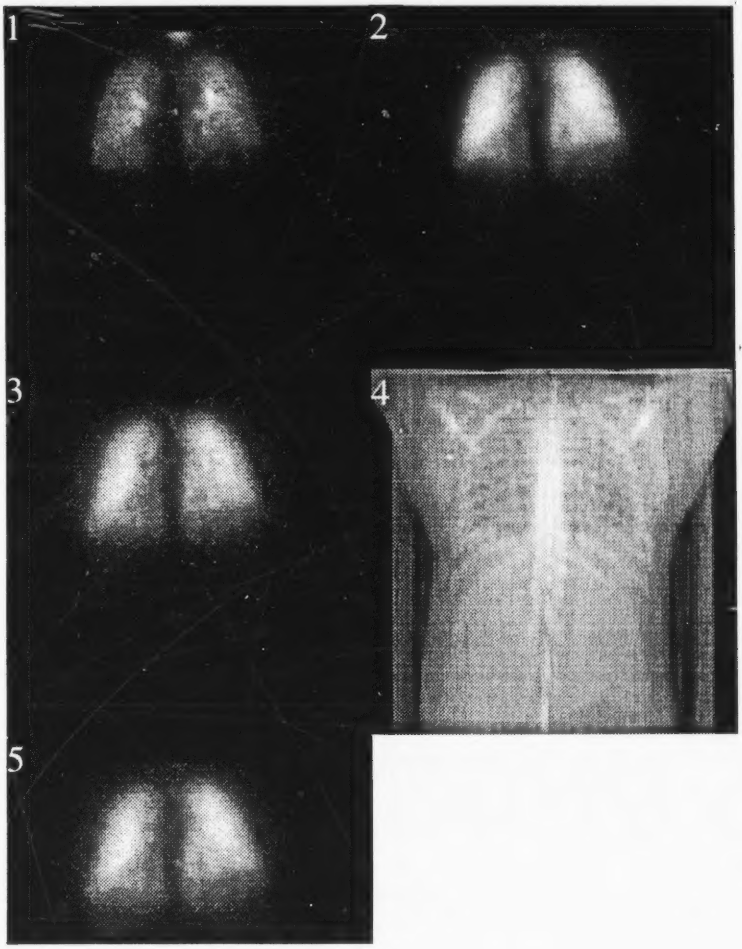

Figure 47. Patient #3: 1) ventilation, 2) perfusion, 3) "pure" perfusion, 4) 2D correction map and 5) the corrected image. All are posterior views.

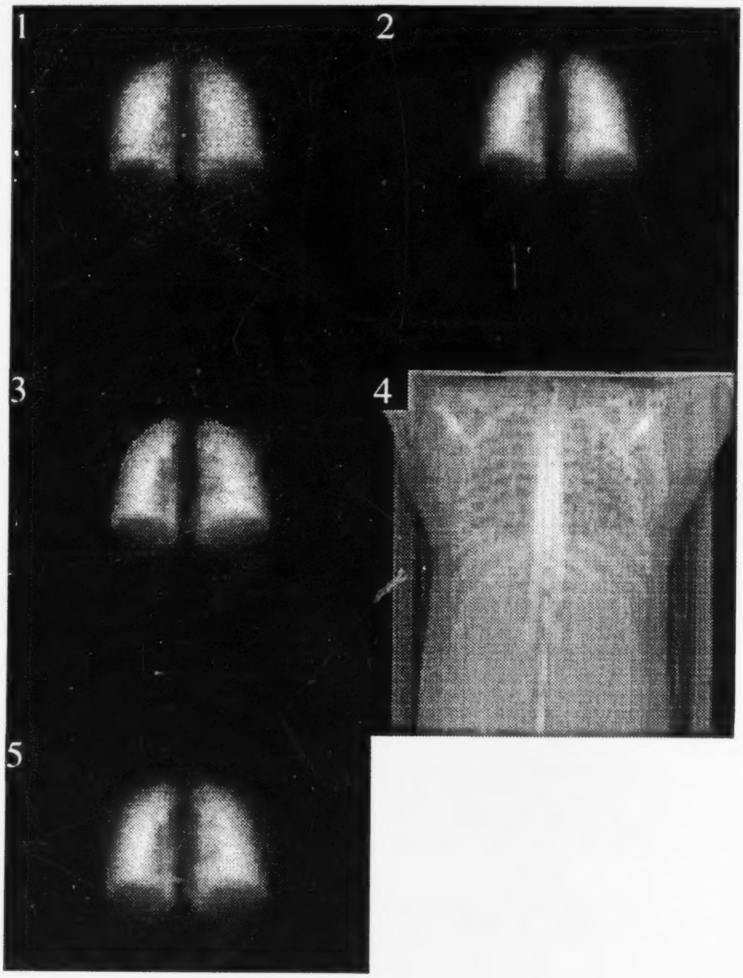

Figure 48. Patient #4: 1) ventilation, 2) perfusion, 3) "pure" perfusion, 4) 2D correction map and 5) the corrected image. All are posterior views.

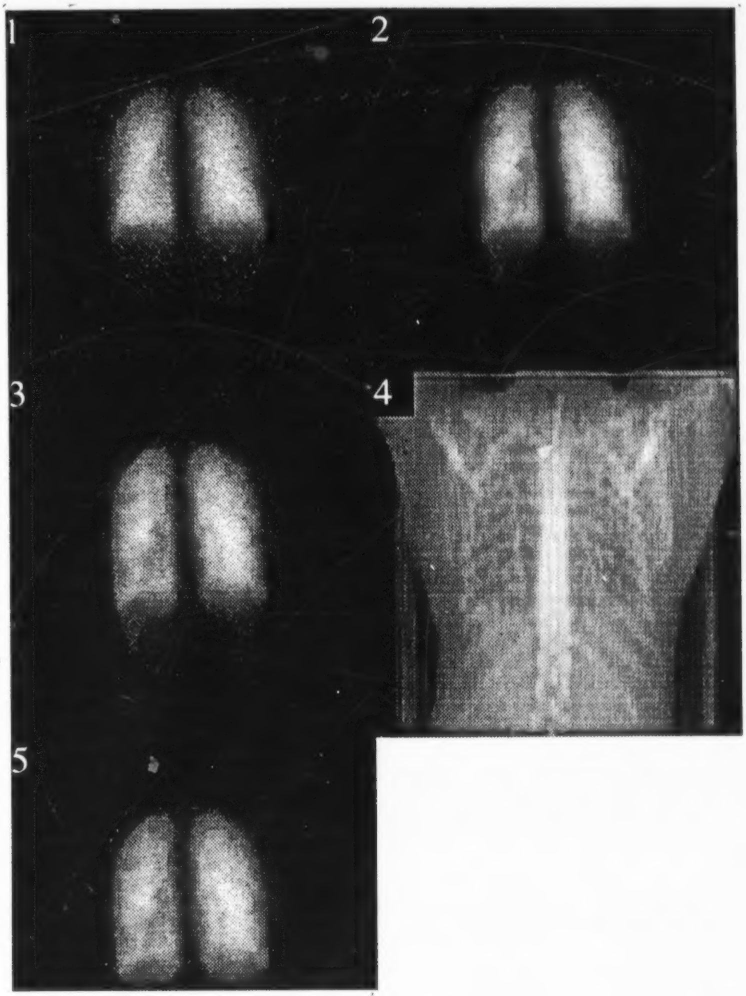

Figure 49. Patient #5: 1) ventilation, 2) perfusion, 3) "pure" perfusion, 4) 2D correction map and 5) the corrected image. All are posterior views.

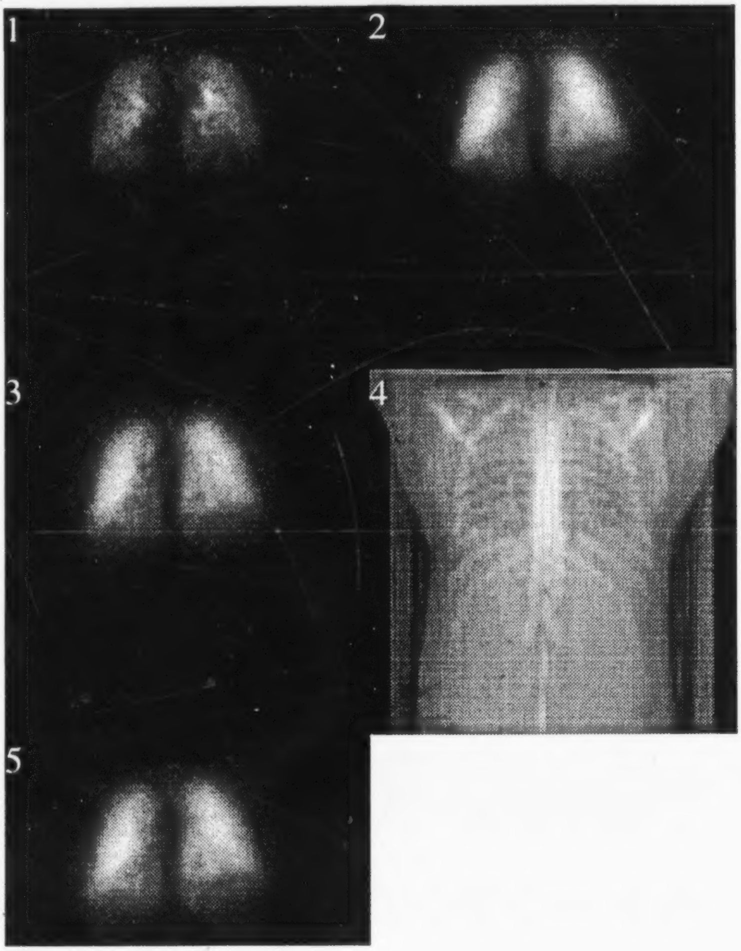

Figure 50. Patient #6: 1) ventilation, 2) perfusion, 3) "pure" perfusion, 4) 2D correction map and 5) the corrected image. All are posterior views.

Chapter 7

7. Conclusions and Future Work

7.1 Conclusions

It is important to note that in spite of the numerous correction methods that have been proposed during the past two decades, none has been accepted as the standard method for clinical use. Most methods have been assessed using physical or simulated phantoms of regular geometries. Physical phantoms cannot attain the complexity of a patient and the simulated configurations are generally simpler than those encountered in clinical practice. Correction methods that use these phantoms and obtain encouraging results are often found unreliable in more realistic situations.

This thesis demonstrates that accurate activity quantification in planar imaging can be achieved using a set of density maps obtained from CT images to correct for attenuation, combined with Monte Carlo simulated buildup functions to correct for the buildup of scatter in the projections. The results indicate that when the density variation over the volume imaged is known and attenuation and buildup are properly corrected for, accurate quantification can be achieved from the measurements of two 180° projections. The accuracy of the new method over the geometric mean method is due to the ability of the new method to take into consideration the density variation of each voxel over the volume of the phantom and, subsequently, accurately correct for attenuation, along each ray of view. The geometric mean method is limited in its assumption that attenuation is the same for all voxels. This assumption is incorrect for a nonhomogeneous medium. Therefore, the use of a single effective attenuation coefficient will produce overcorrection for sources in a region where source activity is not overlapped by dense tissue and undercorrection for source activity "hidden" behind dense tissue.

An algorithm for calculating 2D correction maps from 3D information which allows the user to apply *a priori* knowledge of the activity distribution in defining the coronal plane for the integration process was introduced. It was also shown that one can safely assume any depth in defining the coronal plane about which the 3D structure is to be collapsed into two 2D correction maps and obtain excellent results.

Planar imaging suffers from an inability to take into consideration the 3D nature of activity distribution and the interaction processes. The work presented here describes a new approach to planar imaging that utilizes the 3D information of the volume from which the planar images are obtained to correct for attenuation. It estimates the buildup of scatter and thereby provides for accurate activity quantification. A clinical model was developed using whole body CT data, acquired from a living standard man, to provide corrections in nuclear medicine images. The CT slices of the torso of the living man were reduced from 40.9 MBytes to 5.11 MBytes, thus requiring only minimal computer storage space.

The method was successfully applied to quantification of lung activity of patients in nuclear medicine. One of the most important features of this method is that attenuation and buildup corrections are determined from human data and not from physical or simulated phantoms of regular geometries. Another important feature of this method is that no CT scans of the nuclear medicine patients are required because the standard man provides the appropriate human 3D data required for correction. In addition, the method incorporates the use of Monte Carlo simulations to provide detailed information for use in the computation of buildup factors required for correction.

Finally, the new method, though not perfect, demonstrates significant improvement in the accuracy of planar imaging quantification using human 3D data and can be applied to both planar and SPECT imaging. Undoubtedly, there is more to be done in the development of this method to make it fully adaptable as a clinical method. In the following section, some areas of the project that require further investigation and development for improving the versatility and clinical applicability of the method are presented.

7.2 Future Work

The extent to which the method can be applied in clinical situations will depend, partly, on the degree of manipulation that can be performed on the human model without significant loss of data integrity. Certainly, more work needs to be done on this aspect of the project to develop the required computer software that will provide a more elegant way of manipulating the model to fit the nuclear medicine images. Ideally, the software should facilitate dynamic on-screen manipulation of the model by the user via a mouse or keyboard.

The density maps were created with the assumption that the human body consists of three tissue types: lungs (0.3 gcm^{-3}), bone (1.85 gcm^{-3}) and soft tissue (1.0 gcm^{-3}). Further investigations should be done to include more tissue types in the model which may improve the accuracy of the method since it would more closely repesent the actual situation. Potentially, the density maps can attain the complexity of the density distribution in the human body.

Further evaluation of measured and simulated data should be performed for different kinds of sources (shapes and sizes) in the phantom experiments. In particular, the behavior of the buildup function for sources close to the surface giving rise to overestimation of activity should be investigated. For the clinical applications, other organs of the body should be investigated to further test the accuracy of the method.

References

1. Roentgen WC 1896 Uber eine neue Art von Strahlen (Vorlaufige Mittheilung) Sitzungsber. Phys. Med. Ges Wurzburg Vol. 1895 pp. 137-147.

2. Becquerel H 1896 Sur les radiations invisibles emises par les corps phosphorescents, Comptes rendus de l' Academie des Sciences, Paris **122** 501-503.

3. Curie P, Curie M and Bemont G 1898 Sur une nouvelle substance fortement radioactive contenue dans la pechblende, C. R. Acad. Sci. Paris **129** 1215-1217.

4. Brucer M 1979 Nuclear medicine begins with a Boa Constrictor. In: The Heritage of Nuclear Medicine. Brucer M, Harris CC, MacIntyre WJ and Taplin GV eds. Society of Nuclear Medicine.

5. Myers WG and Wagner HN 1974 How it began. In: Nuclear Medicine Wagner HN ed. (New York: H. P. Publishing) pp. 3-16.

6. Webb S ed 1988 The Physics of Medical Imaging (Bristol: Institute of Physics Publishing) pp. 7-19.

7. Early PJ and Sodee DB 1995 Principles and Practice of Nuclear Medicine. 2nd edn (Missouri: Mosby) Chapters 17 - 29.

8. Bushberg JT, Seibert JA, Leidholdt EM and Boone JM 1994 The Essential Physics of Medical Imaging (Maryland: Williams and Wilkins) Chapter 15.

9. Sanders TP, Sanders TD and Kuhl DE 1972 Optimizing the window of an Anger camera for ^{99m}Tc. J. Nucl. Med. **12** 703-706.

10. Bloch P and Sanders T 1973 Reduction of the effects of scattered radiation on a sodium iodide imaging system. J. Nucl. Med. **14** 67-72.

11. Van Reenen O, Lotter MG, Heyns A du P, De Kock F, Herbst C, Kotze H, Pieters H, Minnaar PC and Badenhorst PN 1982 Quantification of the distribution of indium 111 labelled platelets in organs. Eur J. Nucl. Med. **7** 80-84.

12. Collier BD, Palmer DW, Knobel J, Isitman AT, Hellman RS and Zielonka JS 1984 Gamma camera energy for ^{99m}Tc bone scintigraphy: effect of asymmetry on contrast resolution. Radiology **151** 495-497.

13. Graham LS, La Fontaine RL and Stein MA 1986 Effects on asymmetric photopeak windows on flood field uniformity and spatial resolution of scintillation cameras. J. Nucl. Med. **27** 706-713.

14. La Fontaine R, Stein MA, Graham LS and Winter J 1986 Cold lesions: enhanced contrast using asymmetric photopeak windows. Radiology **160** 255-260.

15. Jaszczak RJ, Greer KL, Floyd CE, Harris CC and Coleman RE 1984 Improved SPECT quantification using compensation for scattered photons. J. Nucl. Med. **25** 893-900.

16. Rogers WL, Clinthorne NH, Stamos J, Koral KF, Mayans R, Knoll GF, Juni J, Keyes JW and Harkness BA 1984 Performance evaluation of SPRINT, a single photon ring tomograph for brain imaging. J. Nucl. Med. **25** 1013-1018.

17. Koral KF, Clinthorne NH and Rogers WL 1986 Improving emission computed tomography quantification by Compton scatter rejection through offset windows. Nucl. Instrum. Methods Phys. Res. **A242** 610-614.

18. King MA, Hademenos GJ and Glick SJ 1992 A dual-photopeak window method for scatter correction. J. Nucl. Med. **33** 605-612.

19. Hademenos GJ, Ljungberg M, King MA and Glick SJ 1993 A Monte Carlo investigation of the dual photopeak window scatter correction method. IEEE Trans. Nucl. Sci. **40** 179-185.

20. Thomas SR, Maxon HR and Kereiakes JG 1976 In vivo quantitation of lesion radioactivity using external counting methods. Med. Phys. **3** 253-255.

21. Ferrant A and Cauwe F 1979 Quantitating organ uptake using a gamma camera. Eur. J. Nucl. Med. **4** 223-229.

22. Macey DJ and Marshall R 1982 Absolute quantitation of radiotracer uptake in the lungs using a gamma camera. J. Nucl. Med. **23** 731-735.

23. Fleming JS 1979 A technique for the absolute measurement of activity using a gamma camera and computer. Phys. Med. Biol. **24** 176-180.

24. Chang LT 1978 A method for attenuation correction in radionuclide computed tomography. IEEE Trans. Nucl. Sci. **NS-25** 638-643.

25. Budinger TF, Gullberg GT and Huesman RH 1979 Emission computed tomography. In: Herman GT, ed. Image Reconstruction from projections: implementation and applications. New York: Springer Verlag 147-246.

26. Mas J, Younes RB and Bidet R 1989 Improvement of quantification in SPECT studies by scatter and attenuation. Eur J. Nucl. Med. **15** 351-356.

27. Manglos SH, Jaszczak RJ, Floyd CE, Hahn LJ, Gree KL and Coleman RE 1987 Nonisotropic attenuation in SPECT: phantom test of quantitative effects and compensation techniques. J. Nucl. Med. **28** 1684-1691.

28. Fleming JS 1988 A technique for using CT images in attenuation correction and quantification in SPECT. Nucl. Med. Comm. **10** 83-97.

29. Tsui BMW, Gullberg GT, Edgerton ER, Ballard JG, Perry JR, McCartney WH and Berg J 1989 Correction of nonuniform attenuation in cardiac SPECT imaging. J. Nucl. Med. **30** 497-507.

30. Meikle SR, Bailey DL, Hutton BF 1994 A transmission-dependent method for scatter correction in SPECT. J. Nucl. Med. **35** 360-367.

31. Wu RK and Siegel JA 1984 Absolute quantification of radioactivity using the buildup factor. Med. Phys. **11**189-192.

32. Siegel JA 1985 The effect of source size on the buildup factor calculation of absolute volume. J. Nucl. Med. **26** 1319-1322.

33. Siegel JA, Wu RK and Maurer AH 1985 The buildup factor: effect of scatter on absolute volume determination. J. Nucl. Med. **26** 390-394.

34. Ljungberg M and Strand S 1990a Attenuation correction in SPECT based on transmission studies and Monte Carlo simulations of buildup fuctions. J. Nucl. Med. **31** 493-500.

35. Buvat I, Benali H, Todd-Pokropek A and Di Paola R 1994 Scatter correction in scintigraphy: the state of the art. Eur. J. Nucl. Med. **21** 675-694.

36. Miller C, Filipow L and Jackson S 1995 A review of activity quantification by planar imaging methods. J. Nucl. Med. Technol. **23** 3-9.

37. Nickoloff EL, Perman WH, Esser PD, Bashist B and Alderson PO 1984 Left ventricular volume: physical basis for attenuation corrections in radionuclide determinations. Radiology **152** 511-515.

38. Ljungberg M and Strand S 1990b Scatter and attenuation correction in SPECT using density maps and Monte Carlo simulated scatter functions. J. Nucl. Med. **31** 1560-1567.

39. Tan P, Bailey DL, Meikle SR, Eberl S, Fulton RR and Hutton BF 1993 A scanning line source for simultaneous emision and transmission measurements in SPECT. J. Nucl. Med. **34** 1752-1760.

40. Miller C, Filipow L, Jackson S and Riuaka T 1996 Planar imaging quantification using 3D attenuation correction data and Monte Carlo simulated buildup factors. Phys. Med. Biol. **41** 1401-1423.

41. Compton AH 1923 A quantum theory of scattering of x-rays by light elements. Phys. Rev. **21** 483-502.

42. Evans RD 1953 The Atomic Nucleus (London: McGraw-Hill).

43. Attix H 1986 Introduction to Radiological Physics and Radiation Dosimetry. (Toronto: John Wiley & Sons) Chapter 7.

44. Johns HE and Cunningham JR 1983 The Physics of Radiology 4th edn (Illinois: Charles Thomas).

45. Chandra R 1982 Introductory Physics of Nuclear Medicine (Philadelphia: Lea & Gebiger).

46. Hall EJ 1994 Radiobiology for the Radiologist. 2nd edn (Philadelphia: Lippincott).

47. Tucker WD, Greene MW, Weiss AJ and Murrenhoff AP 1958 BNL 3746, American nuclear society annnual meeting. Trans. Am. Nucl. Soc. **1** 160.

48. Early PJ 1995 Use of diagnostic radionuclides in medicine Health Phys. **69** 649-661.

49. Ketchum LE 1986 Brookhaven, origin of Tc-99m and F-18FDG, opens new frontiers for nuclear medicine. J. Nucl. Med. **27** 1507-1515.

50. Richards P, Tucker WD and Srivastava SC 1982 Technetium-99m: An historical perspective. Int. J. Appl. Radiat. Isot. **33** 793-799.

51. Cassen B, Curtis L, Reed C and Libby R 1951 Instrumentation for I-131 use in medical studies. Nucleonics **9** 46-50.

52. Anger HO 1967 Radiosotope cameras: In Instrumentation in Nuclear Medicine vol 1 Chapter 19.

53. Sorenson JA and Phelps ME 1987 Physics in Nuclear Medicine. 2nd edn (London: Grune and Stratton).

54. Beck RN, Schuh MW and Cohen TD 1969 Effects of scattered radiation on scintillation detector response. In: Medical Radioisotope Scintigraphy (Vienna: IAEA) vol 1 595-616.

55. Beck RN and Rossmann K 1969 Some fundamental concepts of radioisotope imaging, Book of Abstracts: 12 th International Congress of radiology 146.

56. Ehrhardt JC and Oberley LW 1972 Effects of spectral changes on scanning. Radiology **104** 207-208.

57. Szabo Z, Links JM, Seki C, Rhine J and Wagner HN 1992 Scatter, spatial resolution and quantitative recovery in high resolution SPECT. J. Comput. Assist Tomogr. **16** 461-467.

58. Floyd CE, Jaszczak RJ, Harris CC, Greer KL and Coleman RE 1985 Monte Carlo evaluation of Compton scatter subtraction in single photon emission computed tomography. Med. Phys. **12** 776-778.

59. Ljungberg M, Msaki P and Strand SE 1990 Comparison of dual window and convolution scatter correction techniques using the Monte Carlo method. Phys. Med. Biol. **35** 1095-1110.

60. Gilardi MC, Bettinardi V, Todd-Pokropek A, Milanesi L and Fasio F 1988 Assesment and comparison of three scatter correction techniques in single photon emission computed tomography. J. Nucl. Med.**29** 1971-1979.

61. Singh M and Horn C 1987 Use of germanium detector to optimize scatter correction in SPECT. J. Nucl. Med. **28** 1853-1860.

62. Yanch JC, Flower MA and Webb S 1990 Improved quantification of radionuclide uptake using deconvolution and windowed subtraction techniques for scatter compensation in single photon emission computed tomography. Med. Phys. **17** 1011-1022.

63. Koral KF, Swailem FM, Buchbinder S, Clinthorne NH, Rogers WL and Tsui BMW 1990 SPECT dual-energy window Compton correction: scatter multiplier required for quantification. J. Nucl. Med. **31** 90-98.

64. Filipow LJ, Macey DJ and Munro TR 1979 The measurement of the depth of a point source of a radioisotope from gamma ray spectra. Phys. Med. Biol. **24** 341-352.

65. Koral KF and Johnston AR 1977 Estimation of organ depth by gamma ray spectral comparison. Phys. Med. Biol. **22** 988-993.

66. Hoffer P, Beck R and Stark V 1975 Measurement of scatter correction in liver and brain scans performed with a gamma camera. J. Nucl. Med. **16** 535.

67. Lowry CA and Cooper MJ 1987 A problem of Compton scattering in emission tomography: a measurement of its spatial distribution. Phys. Med. Biol. **32** 1187-1191.

68. Green AJ, Dewhurst SE, Begent RJH, Bagshawe KD and Riggs SJ 1990 Accurate quantification of ^{131}I distribution by gamma camera imaging. Eur. J. Nucl. Med. **16** 361-365.

69. Koral KF, Buchbinder S, Clinthorne NH, Rogers WL, Swailem FM and Tsui BMW 1991 Influence of region of interest selection on the scatter multiplier required for quantification in dual-window Compton correction. J. Nucl. Med. **32** 186.

70. La Fontaine R, Graham LS and Stein MA 1984 Effects of asymmetric photopeak windows on flood field uniformity and spatial resolution for scintillation cameras. J. Nucl. Med. **25** 22.

71. Rollo FD and Shulz AG 1971 Effects of pulse-height selection on lesion detection performance. J. Nucl. Med. **12** 690-696.

72. Oberley LW, Ehrhardt JC and Lensink SC 1972 The variable baseline scanner. Phys. Med. Biol. **17** 630-637.

73. Lange RC 1972 A simpler method for optimizing the window of the Anger camera for Tc-99m. J. Nucl. Med. **13** 342

74. Logan KW and McFarland WD 1992 Single photon scatter compensation by photopeak energy distribution analysis. IEEE Trans. Med. Imaging **11** 161-164.

75. Gilland DR, Jaszczak RJ, Greer KL and Coleman RE 1991 Quantitative SPECT reconstruction of iodine -123 data. J. Nucl. Med. **32** 527-533.

76. Van Rensburg AJ, Lotter MG and Heyns ADP 1988 An evaluation of four methods of ^{111}In planar image quantification. Med. Phys. **15** 853-861.

77. Hammond NP, Moldofsky PJ and Beardsley MR 1984 External imaging techniques for quantitation of distribution of I-131 F(ab)$_2$ fragments of monoclonal antibody in humans. Med. Phys. 11 778-783.

78. Sorenson JA 1974 Quantitative measurement of radioactivity in vivo by whole body counting. In: Instrumentation in nuclear medicine (New York: Academic Press) vol 2 311-348.

79. Myers MJ, Lavender JP and de Oliveira 1981 A simple method of quantitating organ uptake using a gamma camera. Br. J. Radiol. **54** 1062-1067.

80. Evans RD 1937 Radium poisoning: Quantitative determination of radium content and radium elimination rate of living persons. Am. J. Roentgenol. **37** 368-378.

81. Forge NI, Mountford PJ and O'Doherty MJ 1993 Quantification of Tc-99m lung radioactivity from planar images. J.Nucl. Med. **20** 10-15.

82. Welch A, Gullberg GT, Christian PE and Datz FL 1994 A comparison of Gd/Tc versus Tc/Tl simultaneous transmission and emission imaging using both single and tripple detector fan beam SPECT systems. IEEE Trans. Nucl. Sci.**41** 2779-2786.

83. Bailey DL, Hutton BF and Walker PJ 1987 Improved SPECT using simultaneous emission and transmission tomography. J. Nucl. Med. **28** 844-851.

84. Almquist H, Palmer J, Ljungberg M, Wollmer P, Strand SE and Jonson B 1989 Quantitative SPECT by attenuation correction of the projection set using transmission data: Evaluation of a method. Eur. J. Nucl. Med. **16** 587-594.

85. Harris CC, Greer KL, Jaszczak RJ, Floyd CE, Fearnow EC andColeman RE 1984 Tc-99m attenuation coefficient in water-filled phntoms determined with gamma cameras. Med. Phys. **11** 681-685.

86. Wu RK, Siegel JA and Rattner Z 1984 Tc-99m HIDA dosimetry in patients with various hepatic disorders. J. Nucl. Med. **25** 905-912.

87. Takaki Y, Kojima A and Tsuji A 1993 Quantification of renaluptake of Tc-99m DTPA using planar scintigraphy: a technique that considers organ volume. J. Nucl. Med. **34** 1184-1189.

88. Ljungberg M and Strand S 1989 A Monte Carlo program for the simulation of scintillation camera characteristics. Comput. Meth. Prog. Biomed. **29** 257-272.

89. Larsson SA 1980 Gamma camera emission tomography. Development and properties of a multisectional emission computed tomography system. Acta Radiol. Suppl. **363** 17-32.

90. Raeside DE 1976 Monte Carlo principles and applications. Phys. Med. Biol. **21** 181-197

91. Chan H and Doi K 1983 The validity of Monte Carlo simulation in studies of scattered radiation in diagnostic radiology. Phys. Med. Biol. **28** 109-129

92. Hubbell HJ 1969 Photon cross sections, attenuation coefficients and energy absorption coefficients from 10 keV to 100 GeV National Bureau of Standards NSRDS-29.

93. Zubal G, Harrell CR, Smith EO, Rattner Z, Gindi G and Hoffer PB 1994 Computerized three-dimensional segmented human anatomy. Med. Phys. **21** 299-302.

94. Tapplin GV and MacDonald NS 1971 Radiochemistry of macroaggregated albumin and newer lung scanning agents. Seminar Nucl. Med. **1** 132-152.